STARS

University of Central Florida
STARS

Electronic Theses and Dissertations, 2004-2019

2005

Interferometry-based Free Space Communication And Information Processing

Muzamil Arshad Arain
University of Central Florida

Part of the Electromagnetics and Photonics Commons, and the Optics Commons

Find similar works at: https://stars.library.ucf.edu/etd

University of Central Florida Libraries http://library.ucf.edu

STARS Citation

University of Central Florida

STARS
Showcase of Text, Archives, Research & Scholarship

INTERFEROMETRY-BASED FREE SPACE COMMUNICATION AND INFORMATION
PROCESSING

by

MUZAMMIL ARSHAD ARAIN
M.S. University of Central Florida, 2002

A dissertation submitted in partial fulfillment of the requirements
for the degree of Doctor of Philosophy
in the College of Optics
at the University of Central Florida
Orlando, Florida

Summer Term
2005

Major Professor: Nabeel A. Riza

ABSTRACT

This dissertation studies, analyzes, and experimentally demonstrates the innovative use of interference phenomenon in the field of opto-electronic information processing and optical communications. A number of optical systems using interferometric techniques both in the optical and the electronic domains has been demonstrated in the filed of signal transmission and processing, optical metrology, defense, and physical sensors.

Specifically it has been shown that the interference of waves in the form of holography can be exploited to realize a novel optical scanner called Code Multiplexed Optical Scanner (C-MOS). The C-MOS features large aperture, wide scan angles, 3-D beam control, no moving parts, and high beam scanning resolution. A C-MOS based free space optical transceiver for bi-directional communication has also been experimentally demonstrated. For high speed, large bandwidth, and high frequency operation, an optically implemented reconfigurable RF transversal filter design is presented that implements wide range of filtering algorithms. A number of techniques using heterodyne interferometry via acousto-optic device for optical path length measurements have been described. Finally, a whole new class of interferometric sensors for optical metrology and sensing applications is presented. A non-traditional interferometric output signal processing scheme has been developed. Applications include, for example, temperature sensors for harsh environments for a wide temperature range from room temperature to 1000^0 C.

To my parents, Muhammad Sarwar Arshad and Jamila Begum

ACKNOWLEDGMENTS

I am deeply grateful to Almighty Allah Who has blessed me with His unlimited bounties and bestowed the light of Islam that enlightened my soul and mind.

Writing the acknowledgements has always seemed difficult to me. You are supposed to express your gratitude towards a lot of people in a few words who have helped you in a thousand different ways. To me it sounds like you are bidding farewell to your friends for the last time. I always try to avoid this as it depresses me. But following the tradition, I have to write something so I will try to put few words of acknowledgements together in no particular order.

As I am completing my dissertation, I believe one person who is most responsible for this is my adviser Dr. Nabeel A. Riza. I thank him for his guidance, encouragement, and support throughout my graduate studies. During my stay, the things I liked most in the PIPS Lab was the freedom of creativity and the freedom to disagree with Dr. Riza. This really helped me in building my self-confidence that is so vital for a successful career in research. I am also thankful to my Ph. D. committee members, Dr. Michael Haralambous, Dr. James E. Harvey, Dr. Guifang Li, and Dr. M. G. "Jim" Moharam for taking their time and evaluating this dissertation. I had many fruitful discussions with them and I learnt a lot from them both in class and out of class. I am also grateful to them for providing references for many of my scholarships and job positions. Here, I also express my regards to Mrs. Amana Riza for her moral support and bearing the long hours that we often snatched from Dr. Riza's personal time.

I would like to acknowledge the help and support of other faculty members in CREOL and the administration staff. I sincerely believe that one of the reasons that CREOL is doing so well is the student-friendly environment created by the administration. Be it the registration of

Adamjee Science College, G.B.S.S. Gulshan-e-Iqbal, G.B.S.S. Nazimabad, Habib Public School and my first institution Super English School.

Finally, I admit that I do not have words to express my gratitude due towards my parents, Prof. Muhammad Sarwar Arshad and Jamila Begum, for all they have done for me throughout my life and I will not even try to do so. Though Elizabeth Browning said that 'How do I love thee? Let me count the ways' the situation is indeed 'How do thee love me? I can not count the ways'. I am also deeply thankful to my brother, sisters, and other family members for their precious love, prayers and blessings. This also includes my friends in Pakistan who are now part of our family. In the end, since I have thanked so many people, let me at the cost of modesty acknowledge Muzammil Arshad for being stubborn and refusing to give away inspite of so many difficulties. With a big chapter in my life ending, I am satisfied and think that it was a life worth living for.

TABLE OF CONTENTS

LIST OF FIGURES

LIST OF TABLES

LIST OF ABBREVIATIONS

1-D	One-Dimension, One-Dimensional
2-D	Two-Dimensions, Two-Dimensional
3-D	Three-Dimensions, Three -Dimensional
AC	Alternating Current
AO	Acousto-optic, Acousto-optics
AOD	Acousto-optic Deflector
AR	Anti-Reflection
AWG	Arrayed Waveguide Grating
BD	Beam Diameter
BDP	Beam Displacement Mirror
BOS	Broadband Optical Source
BS	Beam Splitter
C	Circulator
CCD	Charge Coupled Device
CFBG	Chirped Fiber Bragg Grating
CL	Cylindrical Lens
C-MOS	Code Multiplexed Optical Scanner
CREOL	Center for Research and Education in Optics and Lasers
DA	Differential Amplifier
dB	Decibel

DE	Diffraction Efficiency
DEMUX	Demultiplexer
EOSC	Etalon Optical Sensor Chip
Eq.	Equation
FBG	Fiber Bragg Grating
FL	Focal Length
FLC	Ferroelectric Liquid Crystal
FO	Fiber-optic
FOC	Fiber-Optic Cable
FP	Fabry Perot
FPCE	Florida Photonics Center of Excellence
FR	Faraday Rotator
FWHM	Full-width at Half-maximum
G	Grating
GHz	Giga-Hertz
GRIN	Gradient-Index
HeNe	Helium-Neon
HM	Holographic material
HWP	Half Wave Plate
Hz	Hertz
I	Interleaver
IF	Intermediate Frequency
IR	Infrared

kHz   Kilo-Hertz

LC   Liquid Crystal

LD   Laser Diode

M   Mirror

MEMS   Microelectromechanical Systems

MHz   Mega-Hertz

MOST   Multiplexed Optical Scanner Technology

MUX   Multiplexer

NLC   Nematic Liquid Crystal

OA   Optical Amplifier

ODL   Optical Delay Line

OSA   Optical Spectrum Analyzer

PBS   Polarization Beam Splitter

PC   Polarization Controller

PCX   Plano Convex

PD   Photodetector

PDL   Polarization Dependent Loss

PMF   Polarization Maintaining Fiber

P-MOS   Polarization-Multiplexed Optical Scanner

PR   Photo-refractive

PTR   Photothermorefractive

QWP   Quarter Wave Plate

R   Receiver

RC	Remoting Cable
RF	Radio Frequency
RH	Reflection Hologram
S	Spherical Lens
SA	Spectrum Analyzer
SiC	Silicon Carbide
SLM	Spatial Light Modulator
SMF	Single Mode Fiber
S-MOS	Space-Multiplexed Optical Scanner
SNR	Signal to Noise Ratio
TE	Transverse Electric
TEM	Transverse Electromagnetic
TFP	Tunable Fabry Perot
TH	Transmission Hologram
TL	Tunable Laser
TM	TM: Beam Spoiling Correction Adaptive Mirror
TOC	Thermo-optic Coefficient
WDM	Wavelength Division Multiplexing
W-MOS	Wavelength-Multiplexed Optical Scanner
VFODL	Variable Fiber Optic Delay Line

LIST OF PUBLICATIONS

Publications in Referred Journals

1. Nabeel A. Riza and Muzammil A. Arain, "Code Multiplexed Optical Scanner", Applied Optics, Vol. **42** (8), pp 1493-1502, (2003).
2. Nabeel A. Riza and Muzammil A. Arain, "Angstrom-Range Optical Path-Length Measurement with a High-Speed Scanning Heterodyne Optical Interferometer", Applied Optics, Vol. **42** (13), pp. 2341-2345, (2003).
3. Nabeel A. Riza, Sajjad A. Khan and Muzammil A. Arain, "Flexible beamforming for optically controlled phased array antennas", Optics Communications, Vol. **227**, pp. 301-310, (2003).
4. Zahid Yaqoob, Muzammil A. Arain and Nabeel A. Riza, High-Speed Two-Dimensional Laser Scanner based on Bragg Gratings stored in Photothermorefractive Glass," Applied Optics, Vol. **42** (26), pp. 5251-5262, (2003).
5. Nabeel A. Riza and Muzammil A. Arain, "Programmable Broadband Radio-Frequency Transversal Filter Using Compact Fiber-Optics and Digital MEMS-based Optical Spectral Control", Applied Optics, Vol. **43** (15), pp. 3159-3165, (2004).
6. Nabeel A. Riza, Muzammil A. Arain and Sajjad A. Khan, "Variable Fiber-Optic Delay Line", Journal of Lightwave Technology, Vol. **22** (2), pp. 619-624, (2004).
7. Nabeel A. Riza and Muzammil A. Arain, "Super Wide Angle Coverage Code Multiplexed Optical Scanner", Optics Letters, Vol. **29** (9), pp, 1004-1006, (2004).
8. Muzammil A. Arain and Nabeel A. Riza , "Precision Polarization Multiplexed Heterodyne Acousto-optic Interferometric Sensor," Optical Engineering, Vol. **44** (5), (2005).
9. Muzammil A. Arain and Nabeel A. Riza, "Fiber Coupled In-line Heterodyne Optical Interferometer for Minimally Invasive Sensing," accepted for publication in Journal of Lightwave Technology, IEEE/OSA.
10. Nabeel A. Riza, Muzammil A. Arain, and Frank Perez, "6-H Single Crystal Silicon Carbide Thermo-optic Coefficient Measurements for Ultra High Temperatures up to 1273 K in the Telecommunications IR band," submitted to Journal of Applied Physics.
11. Muzammil A. Arain and Nabeel A. Riza, "An Opto-electronic Approach for Adaptive Radio-Frequency Transversal Filter Implementation with Negative Coefficients using Optical Spectrum Shaping, " submitted to Applied Optics (OSA).
12. Nabeel A. Riza, Muzammil A. Arain, and Frank Perez, "Harsh Environments Minimally Invasive Optical Sensor using Free-Space Targeted Single Crystal Silicon Carbide," submitted to IEEE Sensors Journal.

Conference Publications and Presentations

13. Muzammil A. Arain and Nabeel A. Riza, "Mid IR Band Optical Sensor For Super Precision Measurements," in Defense, Security, and Aerospace Applications, SPIE Defense and Security Symposium to be held 28 March-1 April 2005 SPIE, Orlando, USA.

14. Nabeel A. Riza, Muzammil A. Arain, Frank Parez, "Harsh Environments Minimally Invasive Optical Sensing Technique for Extreme Temperatures: 1000 deg C and Approaching 2500^0 C," in OFS '05, Belgium.

15. Nabeel A. Riza and Muzammil A. Arain, "Angstrom Sensitivity Polarization Multiplexed Heterodyne Acousto-optic Interferometric Sensor," in IEEE Sensor 2004, October 24-27, in Vienna, Austria.

16. Nabeel A. Riza and Muzammil A. Arain, "Sub-micron range thickness measurements using a novel scanning heterodyne optical interferometer", Sensors, 2002. Proceedings of IEEE, Vol. 2, 12-14 June, 2002, Pages: 1080 -1084.

17. Nabeel A. Riza, Muzammil A. Arain, and Farzan Ghauri, "Tunable Microwave/Millimeter Wave Transversal Filter using Retro-Reflective Spatial Photonics," in International Topical Meeting on Microwave Photonics, MWP 2004, October 4-7, in Maine, USA.

18. Nabeel A. Riza and Muzammil A. Arain, "Code Multiplexed Holography based All-Optical N×N Switch", Photonics in the South East, Sponsored by University of central Florida, SPIE, and OSA, SE-03-D3, Orlando, Florida, November 12-13, (2003).

19. Muzammil A. Arain and Nabeel A. Riza, "Optical Transceiver using Code-Multiplexed Optical Scanner", Lasers and Electro-Optics Society, 2003. LEOS 2003. The 16th Annual Meeting of the IEEE, October 26-30, 2003, Tucson, Arizona, (2003).

20. Muzammil A. Arain, Nabeel A. Riza, High-beamforming power-code-multiplexed optical scanner for three-dimensional displays ", Proc. SPIE Vol. 5243, p. 59-64, Three-Dimensional TV, Video, and Display II; Bahram Javidi, Fumio Okano; Eds., SPIE, September 2003.

21. Muzammil A. Arain and Nabeel A. Riza, "Free Space Optical Wireless using Code-Multiplexed Optical Scanner", INMIC 2002, December 27-28, Karachi, Pakistan.

22. Nabeel A. Riza and Muzammil A. Arain, "3-dimensional wide scan angle optical scanning using code-multiplexed optical scanner", Lasers and Electro-Optics Society, 2002. LEOS 2002. The 15th Annual Meeting of the IEEE, Vol. 2, 10-14 November, 2002, Pages: 578-579.

23. Nabeel A. Riza and Muzammil A. Arain, "Code Multiplexed Optical Scanner", The 86th Annual Meeting of the Optical Society of America, Orlando FL, USA, Sep. 29 - Oct. 3, 2002.

24. Nabeel A. Riza, Muzammil A. Arain, and Zahid Yaqoob, "Agile ultrasound modulated optical tomography techniques using smart fiber-optics", SPIE Photonics West 2004, Conference 5320 Photons Plus Ultrasound: Imaging and Sensing, 24-29 January 2004, San Jose, California, USA.

INTRODUCTION

Optical interferometry is a tool that has been used for a variety of applications even before the advent of lasers. However, after the lasers become widely available, optical interferometric techniques have been employed for optical sensors, surface characterization, refractive index measurements, and distance measurements. Specifically interferometry has been used for temperature, pressure, gas, and humidity sensors using optical technologies such as fiber Bragg gratings, fiber-optic tips, and microelctromechanical devices. Broadly speaking, these interferometers can be classified into two categories; namely high coherence interferometers and low coherence interferometers. In high coherence optical interferometry, two beams produced from a narrow line-width laser are used as signal and reference beams and the required information is encoded into the instantaneous irradiance of the resultant signal. They can be further classified as homodyne and heterodyne interferometers. However, both these interferometers are alignment and noise sensitive and require that the two paths of the beams be close together. In some applications like remote sensing or where the signal beam is physically separated, this factor poses serious limitations. The resolution in high coherence interferometer is usually very high and can be in the sub-nanometer range. However, the maximum range is limited to the operating wavelength λ. One method to extend the range is to use dual wavelength interferometry. This scheme employs two very close wavelengths λ_1 and λ_2 simultaneously to transform the fringe spacing from λ to $(\lambda_1\lambda_2)/(\lambda_1-\lambda_2)$ which is an order of magnitude higher than the previous case. This however reduces the resolution by the same factor for same detection instruments. On the other hand, another alternative is to use low coherence interferometry where

a broadband optical source is used and the required information is carried in the transmitted/reflected spectrum of light. A common configuration is Fabry-Perot type interferometer where the desired information lies in the location of the maxima/minima of the transmitted/reflected signal respectively. These systems provide a large measurement range but suffer from poor resolution. These interferometers are far less alignment sensitive and susceptible to noise than the high coherence type interferometer because of their inherent common optical path nature. However, as the reflectivities of the two surfaces in Fabry-Perot type interferometer decrease, the sharpness of the transmitted/reflected peak/dip is decreased resulting in a further decrease in the resolution. Therefore there is always a trade-off between high resolution and large range in both low coherence and high coherence interferometry.

The theme in this dissertation is to study, analyze, and experimentally demonstrate the innovative use of interference phenomenon in the field of photonic information processing and optical communication. A large number of interferometers have been built and applications demonstrated. Specifically, holographic interferometry, heterodyne interferometry, Fabry-Perot interferometry, and interferometry in the electronic domain have been used to demonstrate optical scanners, optical transceivers, optical path length measurement instruments, reconfigurable RF filters, and optical sensors. The next section describes the over-all organization of the dissertation.

Dissertation Organization

The first chapter deals with the demonstration of Code Multiplexed Optical Scanner (C-MOS) based on phase multiplexed optical holography. It has been shown that the interference of waves in the form of holography can be exploited to realize a novel optical scanner called C-MOS. The C-MOS features large aperture, wide scan angles, 3-D beam control, no moving parts, high beam scanning resolution, and low power consumption. The concept of C-MOS has been extended to build an optical transceiver that can be highly useful in establishing high bandwidth agile links in optical wireless networks. C-MOS based 3-D display technology has also been demonstrated.

Another area of research in this dissertation is optical time delay generation and photonics information processing using interference in the electronic domain. A hybrid analog-digital variable fiber-optic delay line has been demonstrated to solve the dilemma of efficiently enabling many settable and long duration time delays together with continuous and short time delays. The demonstrated design uses cascading of wavelength sensitive analog time delay generation through Chirped Fiber Bragg Grating (CFBG) with the wavelength insensitive digital fiber-optic switched delay line. The demonstrated time delay line can be used in applications such as RF photonic signal processing, all optical packet switched networking, and laser and RF radar systems. Based on the analog time delay generation scheme, a first ever high speed, reconfigurable, broadband RF transversal filter has been implemented using the principle of optical spectrum control through 2-D digital micro mirror spatial light modulator (DMD SLM).

A highly accurate method of optical path length measurements has also been demonstrated in a no-moving parts scanning heterodyne interferometer using a single acousto-

optic Bragg cell in both free space as well as fiber-optic domains. These interferometers are used in optical metrological applications with a resolution of 1.4 Angstrom for thickness measurements and 2.6×10^{-7} for refractive index measurements. A number of variations of the basic heterodyne interferometer for optical path length measurements are presented. The feasibility of multiplexing several sensors using a distributed chip concept has been demonstrated. Specifically polarization multiplexed, space multiplexed, and wavelength multiplexed heterodyne interferometers have been demonstrated.

Finally, designed and demonstrated is a a single crystal Silicon Carbide (SiC)-based minimally invasive smart optical sensor suited for harsh environments and extreme temperatures reaching 2500^0C using non-traditional Fabry-Perot interferometry. The novel sensor design is based on an agile wavelength source, instantaneous single wavelength strong two-beam interferometry, full optical power cycle data acquisition, free-space targeted laser beam, and multi-wavelength signal processing for unambiguous temperature measurements to form a fast and distributed smart optical sensor system. Experiments conducted using a 1550 nm eye safe band tunable laser demonstrate temperature sensing from room temperature to 1000 °C with a measured average 1.3^0C resolution. Applications for the proposed sensor include: use in fossil fuel-based power systems, aerospace/aircraft systems, satellite systems, deep space exploration systems, and drilling and oil mining industries.

In conclusion, different aspects of the innovative use of interferometry are exhausted in this dissertation. It is believed that this dissertation will influence the way interferometry is used in practical applications. Applications like optical sensors and optical scanners will particularly be a significant contribution in the field of optical engineering.

CHAPTER ONE: CODE MULTIPLEX OPTICAL SCANNER

1.1 <u>Introduction</u>

The increased use of lasers in the fields of communications, defense, biomedicine, and material characterization requires accompanying improvements in laser beam steering technology. Optical scanning can be defined as a controlled movement of a point of light in space. An ideal optical scanner is application dependent but generally should have a large aperture, wide scan angles, 3-D beam control, no moving parts, high beam scanning resolution, low power consumption. In addition, this scanner should be high speed, light weight, simple to control, and provide reconfigurability. A number of different scanning technologies have been developed to reach these goals with limited success. These technologies include acousto-optics,[1] bulk crystal electro-optics,[2] integrated piezoceramic electro-optics,[3] and microelectromechanical system (MEMS).[4]

Recently, an optical scanning technology called "Multiplexed Optical Scanner Technology" or "MOST" was introduced to address the ideal scanner requirements.[5] MOST exploits different attributes of the light wave to realize a scanner. For instance, wavelength tuning and selection coupled with dispersive optics are used to realize the Wavelength Multiplexed Optical Scanner (W-MOS).[6-11] In a similar light, the Polarization Multiplexed Optical Scanner (P-MOS) exploits digital polarization switched access of electronically programmable birefringent beamformers to realize a fully programmable 3-D scanner for linearly polarized optical beams.[12-14] Another member of the MOST family is the C-MOS that

implements a 3-D optical scanner via spatial code activated access of holographically stored 3-D beam scan wavefront information.

Here, the C-MOS concept is experimentally demonstrated. The basic 3-D volume or voxel element of a 3-D scan is experimentally implemented as eight points in space by the C-MOS. Coded beamforming information is stored and accessed from a photorefractive crystal. In this chapter, experimental results for C-MOS are described with two applications. Later, the concept of C-MOS is extended for a wide angle C-MOS covering 288^0 field of view. A C-MOS based optical transceiver for optical communications is proposed and experimentally demonstrated.

1.2 <u>Code Multiplexed Optical Scanner</u>

1.2.1 Code Multiplexed Optical Scanner Theory and Holography

Over the years since the invention of the laser, holography [15] has found numerous applications such as in test and measurement,[16] signal processing,[17] entertainment,[18] and image data storage.[19] This section introduces the use of holography for 3-D inertialess beam scanning using spatial orthogonal set phase encoding of the input beam. *Figure* 1.2.1(a) shows the proposed C-MOS concept in the transmissive recording geometry that leads to the generation of an in-line scanning beam. The C-MOS assembly requires the holographic recording of a set of N 3-D scan reference beams with N independent spatial phase encoded signal beams. Specifically, each 3-D scan beam is recalled by imposing its specific spatial code on the input laser beam (see

Figure 1.2.1(b)). Codes and 3-D beam generation optical information can be generated via static

optics such as moving mirrors and phase-coded plates and/or by programmable optics such as

spatial light modulators (SLM) as shown in Figure 1.2.1.
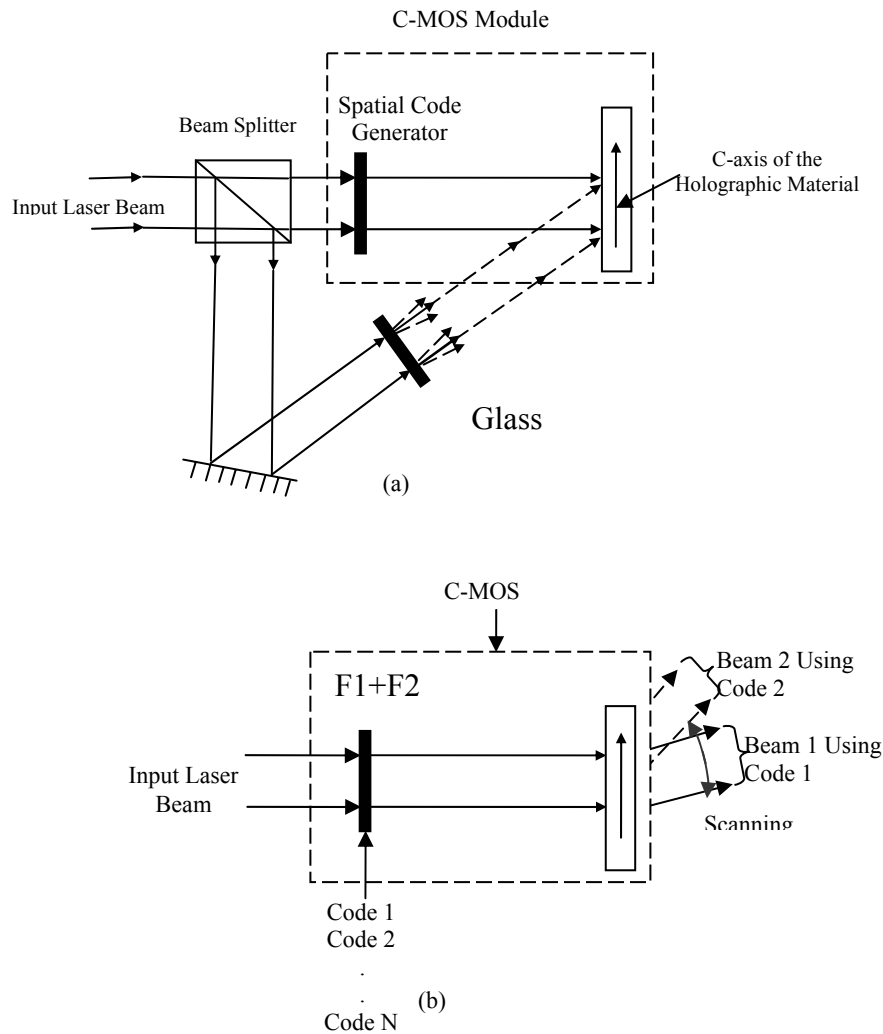
Figure 1.2.1: C-MOS creation and operation shown where (a) shows the hologram recording
with changing optical phase codes in a transmissive assembly, and (b) shows hologram reading
for C-MOS realization in transmissive assembly. PRC: Photorefractive Crystal

The foundation of the C-MOS lies in the principle of holographic information data

storage. Previously, the focus of this field has been storing thousands of high-resolution images

7

(e.g., a one million pixel image) in a single volume holographic material to allow rapid parallel access of two dimensional (2-D) information leading to applications such as real time image retrieval. A key constraint for such a demanding application lies in the storage capacity of the holographic material and the crosstalk or noise level in the image recovery process. In the typical case of one thousand pixel binary (or digital) images, each image of one million pixels, assuming angle multiplexing, a billion pixels must be stored leading to the mentioned high capacity requirement on the holographic storage medium.

In the C-MOS, an almost reverse process takes place where N signal beams each carry a 2-D code of p pixels and N reference beams each represent a point /pixel in 2-D space for implementing 2-D scanning. For 3-D scans representing a spherical wave (instead of a point representing a plane wave), several pixels (e.g., q pixels) are required to produce Q spherical waves where each wave is encoded by r pixels. Hence this scanner would produce N+Q beams requiring a storage medium with a first approximation capacity of $N \times p + Q \times [q \times r]$. For a simple case for N = 100 2-D scan beams generated by N p=100 pixel codes and Q = 10 spherical waves generated by q = 100 pixels and codes with r= 100 pixels, the holographic material capacity must exceed $100 \times 100 + 10 \times [100 \times 100] = 110,000$. This example shows that as a first estimate, a 1000 point C-MOS requires a holographic capacity of 110,000 points versus a 1000 image generator that requires ~ 10^9 point storage capacity, implying that the C-MOS generally requires much lower storage capacity. This also means that lower crosstalk beams can be generated if the higher storage capacity of a medium is used to implement storage via higher pixel value codes.

1.2.2 Code Multiplexed Optical Scanner Design

A beam to be generated in a C-MOS for scanning, with its direction vector $\vec{k}_m$ can have its optical field S_m expressed as:

$$S_m = S_m(x, y) \exp(j\vec{k}_m \cdot \vec{r}),\qquad (1.2.1)$$

where $\vec{r}$ is the position vector of the point in space where the field is to be expressed. This 3-D scan beam wave can be a plane wave or it can be a spherical wavefront depending upon the output scanned beam requirement. The maximum number of phase-encoded holograms that can be stored without cross talk is equal to N, where N is the number of reference beam plane wave components in the phase-coded beam.[20] The corresponding phase coded optical field P can be represented by a summation of N plane waves, each with a different phase and is given by:[21]

$$P = \sum_{n=1}^{N} P_n \exp(j\vec{k}_n \cdot \vec{r}) \exp(j\phi^m{}_n),\qquad (1.2.2)$$

where P_n is the amplitude of the nth plane wave component, $\vec{k}_n$ is the corresponding wave vector, and $\phi^m{}_n$ is the phase of the nth plane wave component for the mth output scanned beam.

From the theory of interference, the intensity recorded in the holographic medium is given by :

$$I_m = \left| S_m + P_n \right|^2$$

$$= S_m(x,y)S^*_m(x,y) + \sum_{n=1}^{N} P_n P^*_n + \sum_{n=1}^{N} S_m(x,y)P^*_m(x,y)\exp[j(\vec{k}-\vec{k}_n)\cdot\vec{r}]\exp(-j\phi^m_n) +$$

$$\sum_{n=1}^{N} P_n \sum_{l=1,l\neq n}^{N} P^*_l \exp([j(\vec{k}_n-\vec{k}_l)\cdot\vec{r}]\times\exp([j(\phi^m_n-\phi^m_l)]. \tag{1.2.3}$$

Here, the third term contributes towards holographic reconstruction. The process of storing N number of scan beams is performed, each with a different phase coded beam. Previously, spatial phase-codes have been used to store image data in holographic materials.[21] Each of the stored scan beams can be reconstructed by illuminating the corresponding phase coded beam and the reconstructed field is given by:

$$R_p(x,y) = \left[\sum_{l=1}^{N} P_l \exp(j\vec{k}\cdot\vec{r})\exp(j\phi^m_l)\right]\times\left\{\sum_{m=1}^{m}\sum_{n=1}^{N} S_m(x,y)P^*_m(x,y)\exp[j(\vec{k}-\vec{k}_n)\cdot\vec{r}]\exp(-j\phi^m_n)\right\}. \tag{1.2.4}$$

Due to the Bragg selectivity restriction, Eq. 1.2.4 simplifies to [22]:

$$R_p(x,y) = \left\{\sum_{m=1}^{m}\sum_{n=1}^{N} S_m(x,y)P_m P^*_m(x,y)\exp(j\vec{k}_n\cdot\vec{r})\cdot\vec{r}]\exp[j(\phi^p_n-\phi^m_n)]\right\}. \tag{1.2.5}$$

Equation 1.2.5 points that two conditions need to be satisfied to avoid cross-talk, namely,

$$\sum_{n=1}^{N} \exp([j(\phi^p_n-\phi^m_n)]=0, \text{for } p\neq m, \text{ and} \tag{1.2.6}$$

$$\sum_{n=1}^{N} \exp([j(\phi^p_n-\phi^m_n)]=N, \text{for } p=m. \tag{1.2.7}$$

Equations 1.2.6 and 1.2.7 show that orthogonal phase codes should be used to avoid cross talk while retrieving the 3-D beam scan hologram. We use Hadamard codes to produce binary phase only orthogonal optical codes.[23] The Hadamard matrices (H-matrix) consist of +1 and -1 values, which can correspond to 0 and π optical phase shifts, respectively.

As mentioned before, the maximum number of phase-encoded holograms that can be stored without cross talk is equal to N, where N is the number of reference beam plane wave components in the phase-coded beam. The number of plane wave components in the phase-coded beam in turn is usually restricted by the resolution of the SLM available. Here generating the phase shift of π is critical, as inaccuracies in realizing a phase shift of π is the most dominant source of cross talk in the reconstruction of holograms. There is a basic difference in the application of holography for data storage and C-MOS. In holographic data storage, the stored information is usually an image, which can have a million points that need to be stored and reproduced accurately. Hence, as mentioned earlier, a high data capacity holographic material is required. In the case of C-MOS, for 2-axis scans, information to be stored corresponds to a single point in space for each code. This is because a point in space corresponds to a plane wave in the far field. For instance, the to be stored scan beam information can be generated through 2-axis mirror movement that generates a set of x-tilted and y-tilted plane waves. For example, if a mirror has four x-tilt and four y-tilt positions, 16 far field points can be generated. Furthermore, apart from tilted plane waves, any shape or type of wavefront can be stored for C-MOS operation, including converging and diverging waves that generate 3-D beam scans. Hence, any arbitrary scanning beam pattern can be realized through C-MOS.

It is important to note that although the input beam to the C-MOS is coded with a near image like spatial code, the scan beam at the exit of the C-MOS can move substantially in 3-D,

11

leading to a powerful scanner. Another advantage of the C-MOS is the ability to reconstruct a linear combination of stored scan beams, a feature possible via the use of phase-encoded holography.[24] This means that while retrieving holograms, we can apply linear combination of phase codes to generate corresponding combination of scan beams. For example, if we store four output scan beams at the front face of the voxel, we can generate all four beams by applying the linear combination of the corresponding phase codes.
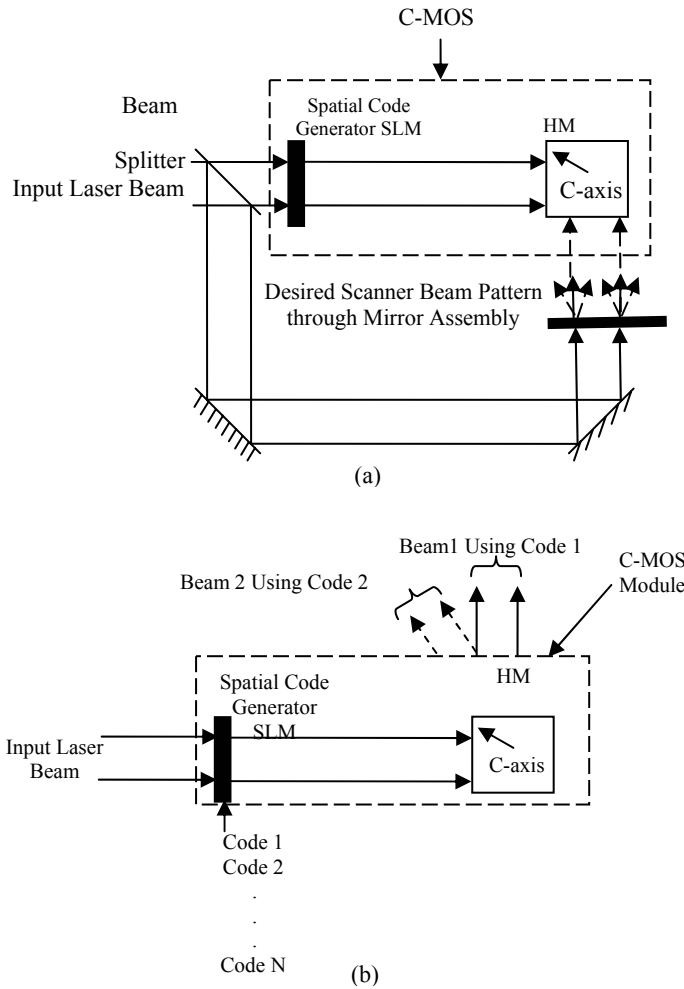
Figure 1.2.2: C-MOS creation and operation shown where (a) shows the hologram recording with changing optical phase codes in a 90° assembly, and (b) shows hologram reading for C-MOS realization in 90° assembly.

Note that the Figure 1.2.1(a) C-MOS assembly gives the flexibility of recording holograms when waves having in-plane polarizations are used. In this case, the electro-optic coefficients, dynamic range and sensitivity might be higher but in-plane polarizations tend to create holographic scattering.

Figure 1.2.2 shows an alternative design for assembling the C-MOS where the c-axis (optic axis) of the storage material is at 45° with respect to the material output faces. This geometry is often referred to as the 90° geometry 45° cut. In this geometry, the polarizations of the interfering beams should be perpendicular to the plane of incidence or in other words, the fields should have ordinary polarization. It is well known that the storage capacity in the transmission geometry (Figure 1.2.1(a)) is higher because more charge per interference fringe is present to build up the space charge field. However, the 90° geometry is mostly preferred because it offers high spatial frequencies yielding larger diffusion fields. Also the scattering is less as compared to the case of transmission geometry, hence the 90° geometry is preferred for holographic data storage using photorefractive (PR) crystals.

For storing N holograms or N different output scanned beam, we need N orthogonal phase codes such as of the H-matrix type. The H- matrix is a square matrix of order $N = 2^n$, with n being an integer. Each row or column can be used as orthogonal code because each row or column is orthogonal to all other rows or columns.

Any holographic storage material can be used with the C-MOS. These include photographic plates, polymer films, silver halide photographic emulsions, photorefractive crystals, photothermorefractive (PTR) glasses and photochromic materials.

1.2.3 Code Multiplexed Optical Scanner Experiment

Described here is proof of concept experiment, in which successfully shown are the capabilities of C-MOS for 3-D beam steering. Using an orthogonal set of spatial codes (e.g. binary phase only codes or Hadamard codes) implemented through an SLM in the path of the laser input, a set of holograms is recorded in a photorefractive crystal. Here each hologram is stored with a different reference scan beam incident on the holographic material at a different angle. After storing and fixing all the holograms, the scan reference beam is blocked and the spatial codes are regenerated on the input laser beam. Via holographic reconstruction, each spatial code generates its original scan beam that at the exit of the C-MOS creates the output scanned beams. Hence, by cycling through spatial codes, via an SLM, a C-MOS is realized for 3-D scans.

Figure 1.2.3 shows the C-MOS demonstration experimental setup. Collimated light from 532 nm Nd:YAG laser is s-polarized and expanded using two lenses S_1 and S_2 making an afocal system with 12.05 magnification. An aperture is used to select the central portion of the collimated beam with uniform intensity. A 50:50 beam splitter is then used to split the incident beam into two beams. One of the beams goes to the reflective Hamamatsu optically addressed Parallel Aligned Nematic Liquid Crystal (PAN LC) SLM, reads the coded phase information, and follows the same path through the beam splitter to reach the photorefractive crystal. The other beam (reference) reaches the adjacent face of the photorefractive crystal to record a hologram in 90° geometry through a combination of mirrors M_1 and M_2 that are used to generate x and y tilts. S_3 is a movable weak lens with focal length FL_3 (75 cm in our case) that is inserted into the path to produce z-axis or 3-D translation of a scan beam. The output scanned

beam is focused via lens S_4 onto the 2-D imaging charge coupled device (CCD). For readout

purposes, the reference beam is blocked and corresponding phase code patterns are applied to the

SLM driver again to produce the scanning beams in space via holographic reconstruction. The

scan speed of the C-MOS is limited by the access time of the SLM, which for the case of the

Hamamatsu SLM is a video rate or 30 ms / scan beam.

Figure 1.2.3: Experimental setup for C-MOS demonstration using orthogonal phase codes and photorefractive crystal as holographic material for 3-D beam scanning.
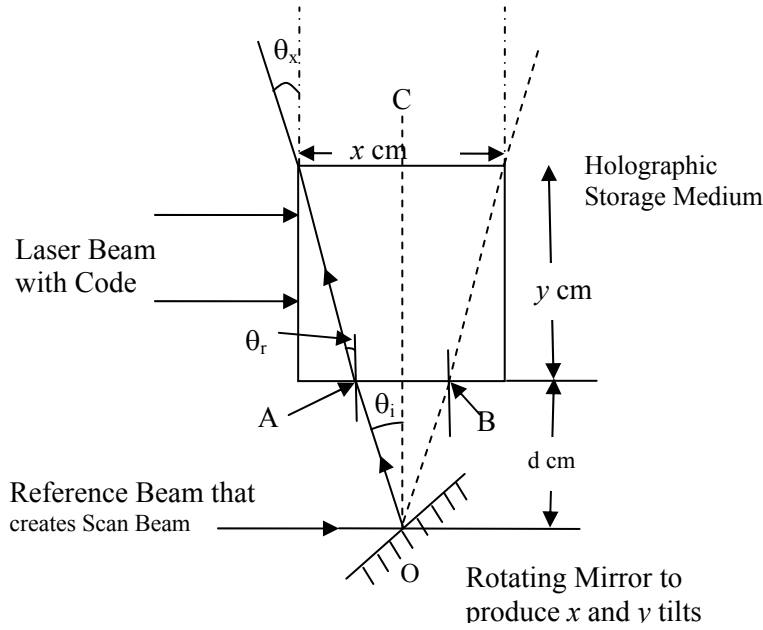
Figure 1.2.4: Geometry to calculate the maximum scan angle in the x-direction for C-MOS in 90° assembly. Y-direction has the same scan angle because of the same dimensions in x and y directions. Here angle AOC represents the maximum scan angle in one direction. The total scan angle is 2 × Angle AOC = Angle AOB.

Note that the scan angles are limited by the geometry of the experiment and by the physical dimensions of the photorefractive crystal. If x and y be the dimensions of the crystal as shown in Figure 1.2.4., then the maximum scan angle that we can get is given by:

$$\theta_{imax} = \tan^{-1}[\{x/2 - y \cdot \tan(\theta_r)\} / d] \qquad (1.2.8)$$

where $\tan(\theta_r) = \sin^{-1}(\theta_{imax})/ n_{eff}$ and n_{eff} = Effective refractive index of the crystal (see Figure 1.2.4). At the point O, a mirror is used to generate x and y tilts by tilting the mirror in x and y direction. The angle AOB represents the maximum scan angle with line segment OC as the central point of the scanner. The distance of the mirror from the crystal is d. By placing the mirror as close as possible to the crystal, we can increase the scan angle. For example, when d =

16

1 cm, x = 1 cm, and y = 1 cm as in our case, we can get a scan of $\pm 12.4^{o}$. However, if we change the dimensions of crystal to d = 0.5 cm, x = 1 cm, and y = 0.5 cm by reducing the width of the photorefractive crystal bearing the phase code information, we can get a scan of approximately of $\pm 21.60^{o}$. This means that the scan angle depends upon the aspect ratio of the dimension of the face of the photorefractive crystal towards the SLM and the face of the photorefractive crystal towards the mirror. In other words, changing crystal-light interaction geometry also requires relevant optimization of the specific crystal size.

Code No.	Phase pattern of code multiplexed beam plane wave components															
	1	2	3	4	5	6	7	8	9	10	11	12	13	14	15	16
1																
2																
3																
4																
5																
6																
7																
8																
9																
10																
11																
12																
13																
14																
15																
16																

Figure 1.2.5: Hadamard Matrix of order sixteen where each row is orthogonal to all other rows representing a phase code for code multiplexing. Here each row corresponds to a single phase code. Dark boxes represents a phase of 0° while white boxes represents a phase shift of 180°. The first eight rows have been used for forming a voxel through the C-MOS.

The Hadamard matrix of order 16 is given by the matrix shown in Figure 1.2.5. In our case, we used the first eight rows of the matrix to store eight beams forming a 3-D voxel element as shown in Figure 1.2.5. A higher order, i.e., 16 × 16, matrix is used to improve C-MOS operation via selection of optimal 8 codes that give the best experimental crosstalk performance.[25-26] Using these phase codes, eight beams were recorded and retrieved as shown in Figure 1.2.6.
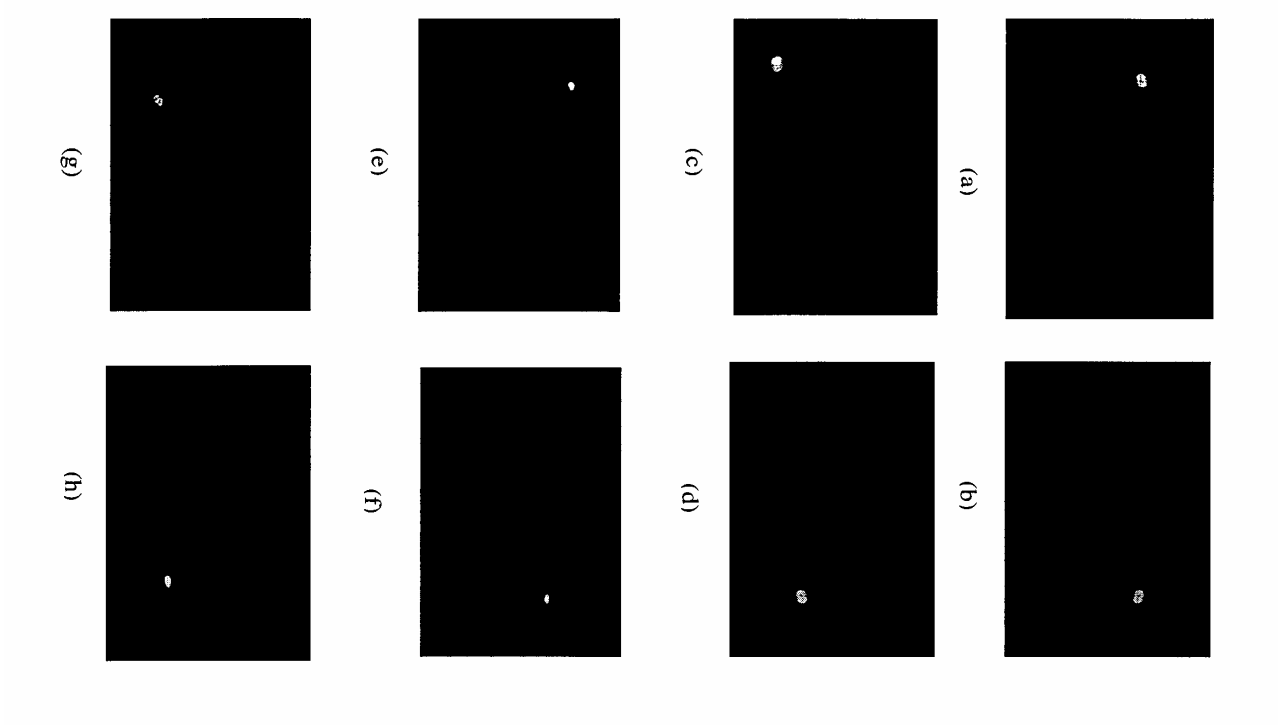
Figure 1.2.6: Eight 3-D beams generated from the proposed experimental C-MOS voxel. (a) - (d) beams are on the front face of the voxel while (e) - (h) beams (appearing more focused) are at the back plane of the voxel.

A beam of 1 cm diameter giving an aperture size of 1 cm for the C-MOS was used. Note that the aperture size is only limited by the dimensions of the photorefractive crystal. Therefore we can increase the aperture size by using a larger photorefractive crystal. Scanning in the x-axis

18

and y-axis is done through rotating the mirror M_2. The maximum scan angle depends upon the geometry of the experiment as discussed above. We rotated the mirror M_2 through 0.333° along y-axis to produce a deflection of 0.1545 cm in the x direction at the focal plane of the lens L_4 located at the CCD. Similarly a deflection of 0.1545 cm in the y direction is obtained by rotating the mirror M_2 through 0.333° along x-direction. Hence $X_o = Y_o = 0.1545$ cm with $\theta_x = \theta_y = 0.333^\circ$ as shown in Figure 1.2.7. These angles were chosen so as to easily capture the voxel scan points with our basic output optics and CCD. However, note that the dynamic range of the C-MOS scanning angle in x and y directions is much wider. As mentioned earlier, the dynamic scanning range depends upon the physical layout of the C-MOS design and size of storage material. In our experiment we measured a θ_x and θ_y scan of $\pm$ 10.5°.
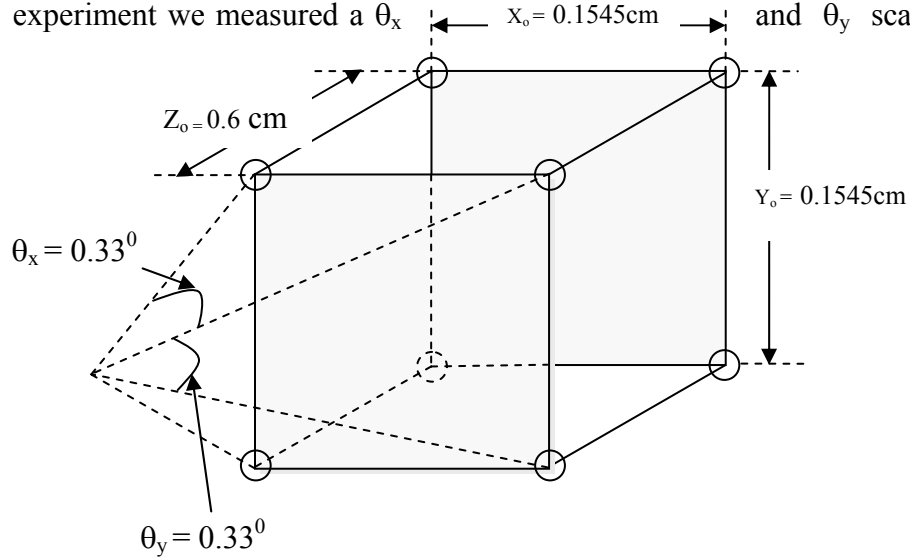
Figure 1.2.7: Generation of Voxel scan element in 3-D space. The circles represent the location of the generated beams in a cubic volume element. X_o, Y_o, and Z_o are the scanning dimensions in the x, y, and z-directions respectively. θ_x and θ_y are corresponding scan angles in x and y directions.

Scanning in the z-direction depends upon the movement of S_3. The effective focal length of the combination of S_3 and S_4 is given by:

$$1/FL = 1/FL_3 + 1/FL_4 - t/ (FL_3 \times FL_4), \qquad (1.2.9)$$

where FL_3 and FL_4 are focal lengths of lenses S_3 and S_4 respectively. Here, t is the distance between the two lenses. Using $FL_3 = 75$ cm, $FL_4 = 20$ cm, and $t = 34$ cm, the effective focal length of the system is found to be 24.59 cm. The back focal distance (BFD) is given by

$$BFD = FL - t \times FL / FL_3. \qquad (1.2.10)$$

The calculated BFD for $t = 34$ cm is 13.442 cm while the measured BFD is found to be 13.3 cm. For the case of $t = 28$ cm, after translating the lens S_3, the calculated BFD is 14.03 cm while the measured value is 13.9 cm. Hence the change in BFD or voxel z-dimension (Z_0)is 13.9 cm − 13.3 cm = 0.6 cm. Using this S_3 / S_4 lens combination, we are able to store and generate the scan beamfronts with the desired focusing / defocusing effect to generate a voxel scan element. The spot size at the CCD camera which is placed at the focal plane of S_4 (when distance between S_3 and S_4 is 34 cm) is found to be 257.5 μm. By changing the distance between S_3 and S_4 to 28 cm, the spot size becomes 463.0 μm at the CCD camera. Note that as generally photorefractive crystals exhibit low diffraction efficiencies where multiple holograms are stored in one crystal, efficiencies, the demonstrated C-MOS also exhibits a low (e.g. , < 1%) throughput efficiency. It is expected that by using holographic materials such as photothermorefractive glasses,[27-28] high (> 50 %) scanner efficiencies can be generated.

1.2.4 Code Multiplexed Optical Scanner Application

As a basic 3-D optical scanner, the C-MOS can be used in a number of applications where accurate yet simple 3-D beam scanning is required.[29]
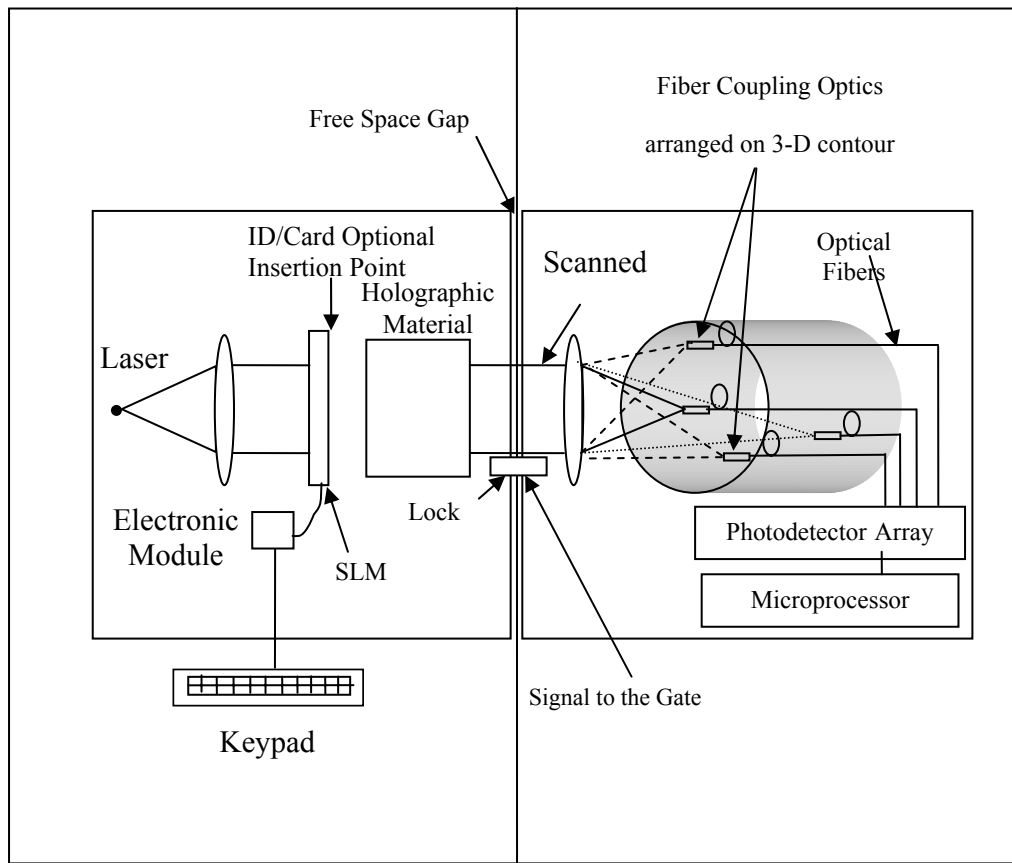
Figure 1.2.8: Proposed C-MOS based optical security lock system.

A novel application for the C-MOS is access control. As mentioned earlier, the diffraction efficiency of a multi-hologram (e.g., 1000 holograms) photorefractive crystal is generally low (e.g. < 1%). This aspect of a photorefractive crystal-based C-MOS can be exploited for security locks and access control. Figure 8 shows our proposed security lock scheme using the C-MOS. At the entrance, a keypad driven SLM or inserted ID card can be used to input the code. The input code generates a particular 2-D phase coded beam that strikes a given holographic material thus generating a particular beam or set of beams in 3-D. This set of 3-D beams passes via the door air gap and via a lens, strikes a 3-D contoured optical sensing

head. The security head contains fiber coupling optics arranged in a unique 3-D geometry where pin-point accuracy is required for the correct coupling of light to the fiber feeds. The fiber coupling optical heads are connected to photodetectors via optical fibers. The optical feed carried in the fibers trigger a given sequence of photodetectors. The photodetector array signals are fed to a microprocessor that processes the data and grants access according to the code information. Note that low diffraction efficiencies via the photorefractive crystal-based C-MOS requires near perfect beam pointing at the detector 3-D plane, thus reducing the probability of false triggering and making a near fail-safe optical lock for high security applications.

1.2.5 C-MOS Based 3-D Display

The basic building block of the proposed 3-D display is the C-MOS. A schematic diagram of the proposed 3-D display is shown in Figure 1.2.9. Here electronic control units control the direction of the output beam from the three basic scanning units. As demonstrated before, C-MOS can form a voxel in space. This capability can produce any type of scanning pattern in space. Hence it can be exploited to form desired images to be displayed. As is well known, every color can be produced by the appropriate mixing of three basic colors, i.e., red, green and blue. Light from three lasers, i.e., red, green, and blue are used to produce three color beams. The intensity of these beams can be controlled by the laser power control unit so that all the possible colors can be generated by appropriately mixing these laser beams at any particular point in space. These beams pass through the SLM inside the C-MOS module, takes the appropriate orthogonal phase code for the desired direction implemented via the 3-D image formation control.
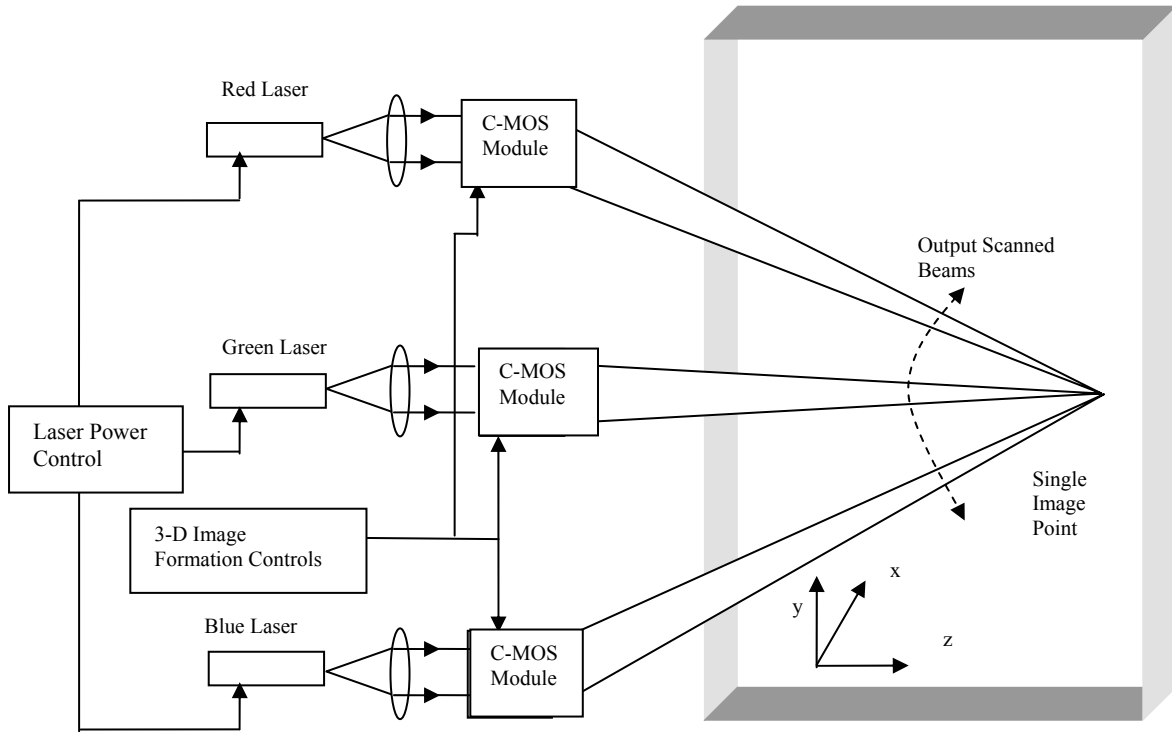
Figure 1.2.9: Schematic Diagram of a C-MOS-based 3-D Display.

In the three C-MOS modules, a raster scan pattern is stored in such a way that these scanning units can produce raster scans at different planes. The raster scan produce a 2-D image in x and y direction while the z-position of this raster can be varied by using the z-scan capability of the scanner. Hence a true 3-D image can be generated by scanning point-by-point in space. This arrangement does not require any type of special equipment to see 3-D images and hence can be very useful in 3-D imaging. Moreover, the diffraction efficiency of the C-MOS is usually kept low, and hence it is not dangerous for the naked eye. Note that the output scanned beams are converging spherical beams that intersect at a common point. The intensity of the beams is controlled in such a way that the combined intensity is above threshold of the human eye only at

23

the point where these three beams intersect. Hence an image is formed only at the focal point. By varying the focal length along the z-direction, perception of depth is produced in the 2-D image. Large scan angles and aperture sizes offered by the C-MOS are best suitable for 3-D displays for large size images and large field of views. The ability to recall linear combinations of stored scanned beams can be useful in multiple image generation or high speed operation of 3-D displays. In conventional 2-D displays, image is generated through point-by-point raster scan while in the proposed C-MOS based 3-D display, this scanning can be replaced by simultaneous scanning of multiple points through the C-MOS scanner. Hence this ability adds a very powerful feature to the proposed C-MOS based 3-D display.

1.3 <u>Wide Angle C-MOS</u>

1.3.1 Theory and Design of Wide-Angle C-MOS

In the previous section, the classic 90^0 hologram formation geometry was used to design the C-MOS that in-turn led to a restricted angular scan range. Specifically, using a 2cm(Length) × 2cm(Height) × 2cm(Thickness) photorefractive crystal for hologram storage, we demonstrated a 53^0 scan range. Here the scan angle depends upon the aspect ratio of the dimension of the face of the photorefractive crystal towards the scan beam side and the face of the photorefractive crystal towards the reference beam side.[30] This physical constraint in-turn limits the input beam angles for the successful recording of holograms that eventually create the scanner exit beams.

This is due to the fact that we can not change the aspect ratio without reducing the aperture size of the scanner. Figure 1.3.1 shows the proposed wide angular coverage C-MOS design that relies upon the reconstruction of wavefronts and their conjugates using in-line holography. Compared to the 90^0 recording geometry, the proposed in-line geometry greatly softens the restrictions on the angular range of the input recording beams as the thickness of the holographic material can be reduced without reducing the aperture size of the scanner. Specifically, a wide angular coverage scanner is realized using a combination of both transmissive and reflection holograms. With respect to Figure 1.3.1 and without loss of generality, consider a signal beam traveling in the z-direction with its electric field expressed as $S(x,y) = S(x,y)e^{(-jkz)}$ and a reference beam with electric field represented as $R(\mathbf{r}) = R(x,y)e^{(-j\vec{k}\cdot\vec{r})}$. Here $\vec{k} = \frac{2\pi}{\lambda}\hat{k} = k\hat{k}$ where $\hat{k}$ is a unit vector in the direction in which the reference beam is traveling and $\vec{r}$ is the unit vector at a point in space where the electric field has to be expressed. From the theory of interference, when these signal and reference waves interfere in the holographic material, their resultant intensity is given by:[15]

$$I(x,y) = SS* + RR* + SR* + S*R,\qquad\qquad(1.3.1)$$

where * denotes complex conjugate. It is important to note that the polarization states of the two interfering waves need to be parallel to each other. Hence s or TE polarization (i.e. vertical) is preferred for both the waves in Figure 1 so that the coupling between the two beams is not reduced. The resultant intensity is stored as a transmittance $t(x,y)$ in the holographic material and can be written as:

$$t(x,y) \propto I_0 + SR* + S*R,\qquad\qquad(1.3.2)$$

where I_0 denotes the DC terms. This resultant intensity is stored in a holographic material using a different signal beam for every reference beam that is used as a scanned beam. These signal beams have orthogonal phase codes such as Hadamard codes written on them using a digital operation phase-only spatial light modulator (SLM). The specific reference or scanned beam can be reconstructed by its corresponding phase coded signal beam. It is important to note that if we multiply Eq. 1.3.2 by R*, i.e., a conjugate reference beam traveling in the opposite direction, the third term in Eq. 1.3.2 gives a conjugate signal beam. This beam travels in the opposite direction to the original beam and after passing through the spatial code generator SLM, becomes a plane wave. This feature can be exploited to realize a free-space agile transceiver for establishing a two way communication link.[31,32]

Recall that to enable the wide angle C-MOS, holograms in the holographic material are recorded in two configurations, i.e., as transmission holograms and as reflection holograms. The recording (Figure 1.3.1(a)) and reading (Figure 1.3.1(b)) operations of the wide angle C-MOS using transmission holography are shown with the help of beam 1. However, when the z-component of the reference beam and signal phase-coded beams are in the opposite direction, a reflection hologram is recorded, as indicated by beam 2 operations in Figure 1.3.1.

The available angular scan for the proposed wide scan angle scanner depends upon the physical size of the SLM and the holographic material and their relative distance Z_1. Figure 1.3.1(a) shows four regions which cannot be accessed for C-MOS fabrication and eventual scan beam generation. Two regions of angular span 2θ are due to the finite size of the holographic material. If the width of the holographic material is W and its thickness is D, then $\theta = tan^{-1} (D / W)$ as shown in Figure 1.3.1 (c). Similarly, the finite physical extent of the SLM also restricts the angular scan by 2ϕ as shown in Figure 1.3.1(a), giving $\phi = tan^{-1}(L / Z_1)$. This restricted angular

scan region can be reduced by using a smaller SLM or by placing the SLM farther away from the

holographic material.
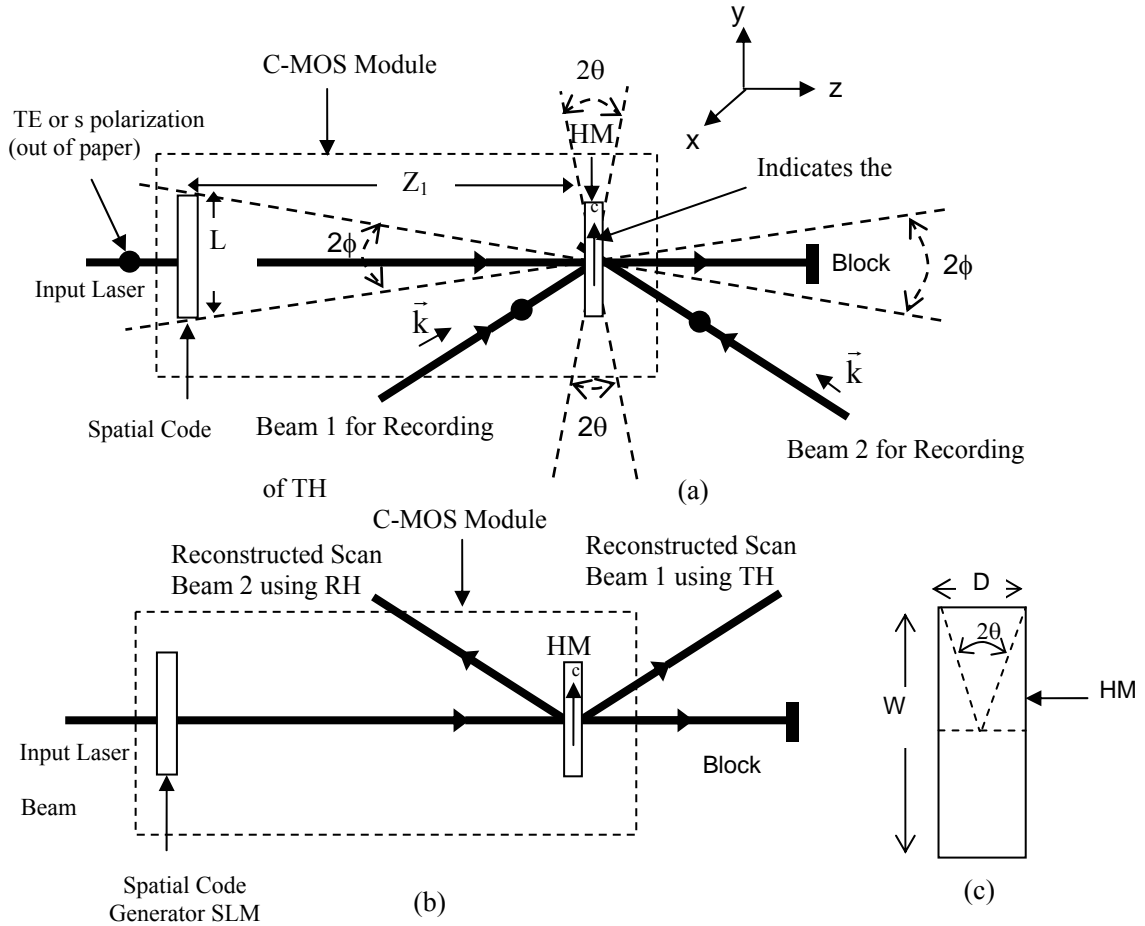
Figure 1.3.1: Wide angle C-MOS creation and operation shown where (a) shows hologram recording with changing optical phase codes with beam 1 recorded as a transmission hologram (TH) and beam 2 recorded as a reflection hologram (RH), (b) shows hologram reading for C-MOS realization with beam 1 reconstructed as a TH and beam 2 reconstructed as a RH, and (c) the holographic material physical geometry used to calculate the restricted scan region. HM: Holographic Material.

It is well-known that the reconstructed beam quality from a holographic material usually

suffers during the hologram readout process. The dominant source of this spatial degradation is

via the non-linear hologram recording process. However, this limitation can be alleviated by

operating in the linear region of the transmittance-exposure curve of the holographic material.

Specifically, adverse effects can be minimized by limiting the exposure fluctuations in the range $E_0(1-V_{max}) < E < E_0(1+V_{max})$ [33] where V_{max} is the maximum visibility of the interference fringes in the holographic material while E is the localized exposure and E_0 is the average exposure. Equal diffraction efficiency is also an important requirement in generic laser beam scanners. This goal can be achieved by employing a proper exposure schedule during the C-MOS hologram recording process such as suggested in Ref. [33].

1.3.2 Experimental Demonstration

The basic laboratory structure of the demonstrated wide angle C-MOS is shown in Figure 1.3.2. Here the module in the box is a basic C-MOS unit containing a spatial phase code generator SLM and a holographic material. Here, N reference beams have been stored in the holographic material using N orthogonal phase codes in the path of the coded signal beam. The direction of the reference or output scanned beam can be altered by appropriately positioning the mirrors M_1 and M_2, in addition to other optics as indicated by the dotted beam paths in Figure 1.3.2. These mirror optics can be used to direct the reference beam on both sides of the holographic material to record holograms in both transmission and reflection configuration.

The main challenge in realizing the proposed wide angle C-MOS lies in selecting and employing the appropriate stable optics for hologram recording. As each component can contribute noise to the reconstructed scan beam, an environmentally stable C-MOS construction setup is required to avoid scanner beam degradation. Another constraint in designing the present C-MOS experiment is via the physical size limits of the available optics components that in-turn restricted the experimental angular scan of the wide angle C-MOS. Specifically, the holographic

material used is iron doped $LiNbO_3$ photorefractive crystal of 3 cm (length) $\times$ 3 cm(height) $\times$1 cm(thickness). This results in a $\theta = 10^0$.
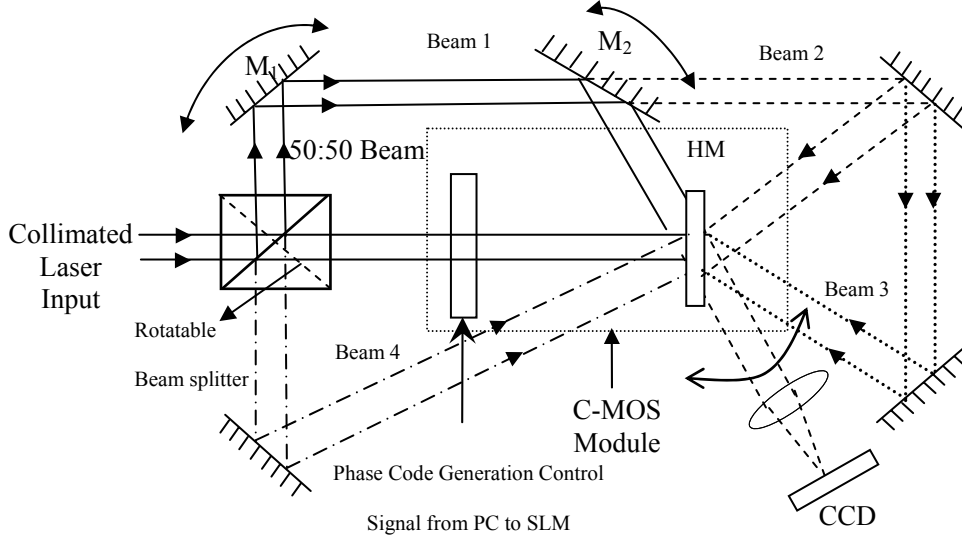
Figure 1.3.2: Experimental setup for the wide scan angle C-MOS demonstration using the in-line geometry and 0^0 c-axis photorefractive crystal as the holographic material.

The experiment is performed with a TE polarized Argon ion laser operating at 514.5 nm with an intensity of 100 mW/cm^2. A transmissive phase-only mode nematic liquid crystal SLM with 128 linear array column electrodes is used for entering the Hadamard codes. The SLM package size has a length L of 18 cm. The SLM is placed at a distance Z_1 of 65 cm from the holographic material resulting in a ϕ of 8^0. Note that the length L mentioned earlier is of the complete optical and electronic package, not just the optically active area of the SLM which in this case is 1.28 cm. Given the mentioned experimental constraints, four scan sectors with an angular scan of 90^0-8^0-10^0=72^0 each are created for the demonstrated scanner. Hence, the total angular scan is $4\times 72^0 = 288^0$ for the designed scanner. For a proof of principle experiment, six randomly chosen beams covering the wide angle sectors were recorded and reconstructed using

six rows of a Hadamard Matrix of order 8. These reconstructed six wide angle scan beams are shown in Figure 1.3.3.
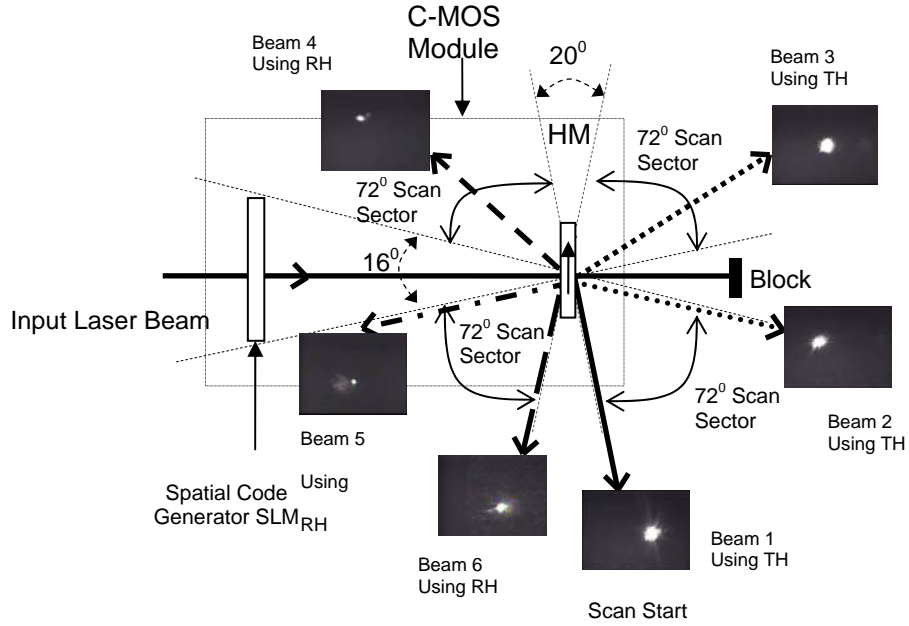
Figure 1.3.3: The demonstrated wide angle C-MOS realized by storing and reconstructing six output scanned beams as transmission and reflection holograms in a 288^0 angular scan range.

These beams were detected one at a time by means of a CCD placed at the correct output location. A minimal cross-talk of – 9 dB with a per beam efficiency of 5% was measured. This limited cross-talk level was achieved partly due to the low code complexity and partly because of the phase code in-active pixel gaps in the SLM. Hence a powerful super wide angle C-MOS is realized that can provide a scan coverage of nearly 4π steradian.

1.4 <u>Optical Transceiver using Code-Multiplexed Optical Scanner</u>

1.4.1 Theory and Design of Optical Transceiver

The rapid growth in science and technology in the present world is largely due to the availability of effective and fast communication links that enable information transfer at unprecedented pace. However, the increased demand of these services along with the emergence of new business and household applications such as but not limited to high-quality video conferencing, data mirroring, e-commerce, telemedicine, data warehousing, large-file transfers, video-on-demand, and interactive video are driving the need for ultrahigh bandwidth services. These demands can potentially be fulfilled using optical communication techniques that offer high speed and ultrahigh bandwidth channels. For example, single mode fibers operate at either 1300nm or 1500nm low absorption window with bandwidths in 1,000s of GHz while the fastest ATM switching systems operate at 25GHz. This shows that in future, conventional electronic communication will eventually be replaced by optical communication at all levels including the end-users links like local area networks and short haul wireless networks.[29]

Deployment of optical communications at all networking layers requires high speed, cost effective and efficient interconnection techniques. Presented here is a novel transceiver for agile two-way free space communications. Earlier, the Code Multiplexed Optical scanner (C-MOS) was introduced along with its proof of concept demonstration.[30,31] Here this concept is extended to a C-MOS Transmitter/Receiver (Tx/Rx). C-MOS Tx/Rx relies upon the reconstruction of wavefronts and their conjugates using holography. Consider a signal beam with its electric field

expressed as $S = S(x, y)e^{(-i\varphi(x,y))}$ and a reference beam with electric field $R = R(x, y)e^{(-i\theta(x,y))}$. From the theory of interference, when these waves interfere, their resultant intensity is given by:[15]

$$I(x, y) = SS^* + RR^* + SR^* + S^*R, \tag{1.4.1}$$

where * denotes complex conjugate. A complex conjugate beam is a beam that is identical to the original beam except that it is reversed in time and space. So if we have a diverging spherical wave propagating beam in z-direction, its conjugate will be a converging spherical beam traveling in negative z-direction. The first two terms represent the intensities of the reference and signal beams and do not have any information while the third and the last term forms interference fringes. This resultant intensity is stored as a transmittance *t(x,y)* in the holographic material and can be written as:

$$t(x, y) \propto I_0 + SR^* + S^*R, \tag{1.4.2}$$

where I_0 denotes the DC terms. This resultant intensity is stored in a holographic material by using a different signal beam for every reference beam that is used as a scanned beam. These signal beams have orthogonal phase codes such as Hadamard Codes written on them using a spatial light modulator (SLM). The specific reference or scanned beam can be reconstructed by its corresponding phase coded signal beam. If we multiply Eq. 1.4.2 by S, the second term in Eq. 1.4.2 gives us the desired reference or output scanned beam. However, if we reconstruct the wavefront by illuminating the conjugate of the reference beam, i.e., R*, we get the conjugate signal beam from the third term in 1.4.2. This beam travels in an opposite direction to the original coded signal beam. The illumination of the holographic material with the coded signal

beam represents the transmit mode of the proposed C-MOS Tx/Rx while illumination with

conjugate reference beam creates the receive mode of the C-MOS Tx/Rx module.

1.4.2 Experimental Demonstration

The basic structure of the free space C-MOS Tx/Rx is shown in Figure 1.4.1. Here the

module in the box is a basic C-MOS unit containing a SLM, a holographic material, and a beam

splitter (BS). Here, the N reference beams have been stored in the holographic material using N

orthogonal phase codes in the path of the coded signal beam.
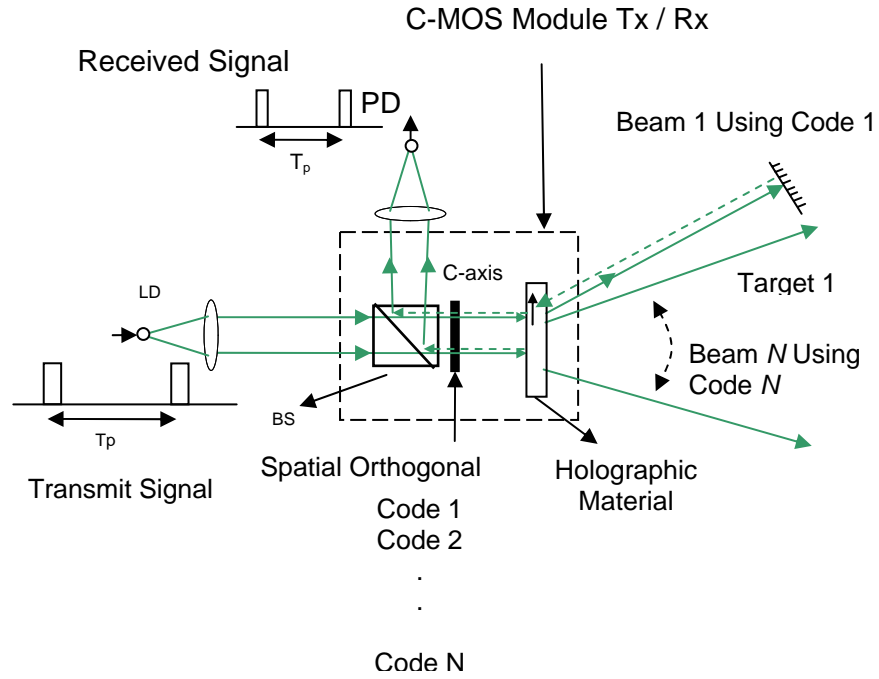
Figure 1.4.1: Basic structure of proposed Free Space C-MOS Transceiver. T_p is the pulse repetition period of the transmitter: Transmit, LD: Laser Diode, PD: High Speed Photodetector, R: Receiver, BS: Beam Splitter.

The free space C-MOS Tx/Rx depends on code selective multiplexed holography. Depending upon the code selected in the path of signal beam at the transmitter station, a different direction is selected which corresponds to for example, a particular target location for laser radar operation. The target can also be another C-MOS Tx/Rx location. Hence by cycling through the orthogonal phase codes, one can establish a Transmit/Receive link between any of the two points in the transmit and receive chain. The link is established when the light beam tracks the retroreflective or common path between the transmitter and receiver. Hence the target reflected light passes through the holographic material in the C-MOS Tx/Rx, and according to the laws of holography, generates a conjugate coded signal beam which travels in the opposite direction from the actual coded signal beam. The orthogonal phase codes used in C-MOS are binary phase codes consisting of 0^0 and 180^0 optical phase shifts. When the signal beam passes through the SLM, different spatial components pick either 0^0 or 180^0 depending on their spatial position. When the conjugate beam is generated and passes through the SLM, it picks the same amount of phase. More importantly, by passing through 0^0 or 180^0 optical phase shifts twice means that the wavefront curvatures due to the binary coding are cancelled out generating an on-axis plane wave that turns into the received beam focused on the fixed high speed point photodetector. In this manner, a two way wide data bandwidth link is established using C-MOS operations.

A proof of concept experiment is performed with code 1 (corresponding to a plane code pattern) that records and then generates output scanned beam using iron doped Lithium Niobate photorefractive crystal as the holographic material and at a wavelength of 514.5nm. This beam is then modulated by means of chopper with a 30% duty cycle chopper. This beam is then retroreflected by means of a mirror and travels in the opposite direction while passing through the photorefractive crystal and generates the conjugate signal beam that is correctly aligned and

detected by the point photodetector. Figure 1.4.2 shows the oscilloscope of the received signal obtained via the photodetector.
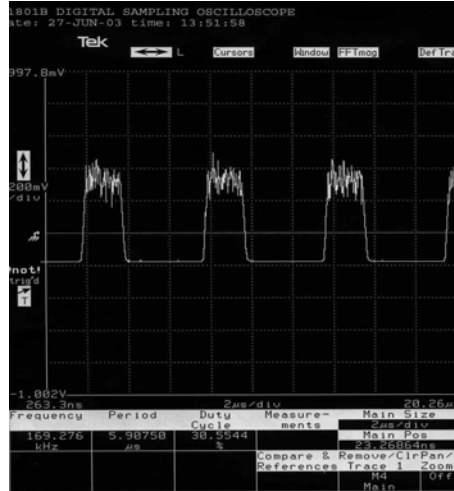
Figure 1.4.2: Oscilloscope trace for the C-MOS transceiver modulated receive signal   at the PD, showing the expected 30% duty cycle modulated signal.

1.5 <u>Limitation of C-MOS</u>

As discussed in previous sections, C-MOS has powerful new features that no other scanners can provide. Specifically, almost 360^0 coverage provided by C-MOS along with 3-D beam scan capabilities make C-MOS an ideal candidate for scanning in a number of commercial, communications, and military applications. However, C-MOS has two draw backs that have to be overcome to exploit the full potential of C-MOS.

1. Diffraction Efficiency

2. IR Operation

Both these draw backs are material related. Now the limitations of C-MOS are discussed in detail.

35

1. Diffraction Efficiency

C-MOS operates on the principle of multiplexed holography in photorefractive crystals. Specifically $LiNbO_3$ has been used in the proof-of-concept experiments. Specially doped and fabricated $LiNbO_3$ crystals can produce up-to 100 % diffraction efficiencies for a single hologram. However, in C-MOS multiple holograms have to be recorded in the same material. It is well known in holographic data storage using $LiNbO_3$ crystals that the efficiency per hologram drops as $1/N^2$ where N is the number of holograms (see Ref. [20, 25]). Hence storing multiple holograms drastically lowers the diffraction efficiency using current commercial holographic materials. This restricts the practical application of C-MOS to the cases where lower efficiencies are desirable. Two such applications, namely security lock and 3-D display, have been proposed where C-MOS has a big potential. However, for other applications where higher diffraction efficiency is required, suitable materials are required.

2. IR Operation

A number of intended C-MOS applications are in the IR band. However, so far no materials are commercially available in which holograms can be recorded in the near IR band. Therefore, this is another field where available materials restrict the use of C-MOS.

With the progress of material sciences, it is expected that an ideal material for C-MOS might become available that will guarantee deployment of commercially available C-MOS modules for target designation, 3-D displays, laser radars, and free space communication.

Conclusions

In this chapter, a novel 3-D optical scanning technique called C-MOS is described that is based on holography and phase code multiplexing. 3-D output scanned beams are generated with the help of spatial phase codes, where phase codes are based upon robust binary Hadamard codes. Demonstrated is basic 3-D scan operational principles of the C-MOS by forming an 8-beam voxel element. Initial experimental results using visible light and a photorefractive crystal-based C-MOS design indicates large $\pm 10^{o}$ scan ranges and better than 0.3^{o} x-y scan resolutions with better than 6mm z-direction scan capacity. For wider scan angles, a super wide angle Code Multiplexed Optical Scanner based on transmissive and reflection holography produced via the in-line hologram formation geometry. This C-MOS has a capability of scanning in 4π steradians. In the proof-of-concept experiment, a scan of 288^{0} in one direction has been demonstrated using six randomly formed beams in the chosen scan zones. A number of applications of C-MOS has been demonstrated and proposed. A novel optical lock application has been introduced for the photorefractive crystal based C-MOS. Proposed and demonstrated is a novel optical transceiver for two-way free space communications in the optical domain using the C-MOS. This technique can also be used for infrared band optical radar, countermeasures, and target designation. C-MOS can be implemented for true 3-D displays that do not require special optics to view 3-D images. Also it does not require any software implementation. It is suitable for large aperture and FOV 3-D display applications. This proposed 3-D display is capable of high speed operation along with the possibility of multiple image generation.

Although the proposed C-MOS can deliver, to the best of our knowledge, the world's widest scan angle with no moving parts, issues related to holography such as limited diffraction efficiencies with increasing number of scan beams (i.e., holograms) limits the scanner throughput, making it appropriate for applications using high power lasers or high sensitivity detectors.

References

1. M. Gottlieb, C. L. M. Ireland, and J.M. Ley, "Electro-Optic and Acousto-Optic Scanning and Deflection," Marcel Dekker, (1983).
2. V. J. Fowler and J. Schlafer, " A survey of laser beam deflection techniques," *in Proceedings of IEEE Conference*, (1966), **54**, pp.1437.
3. Q. W. Song, X. Wang, R. Bussjager, and J. Osman, "Electro-optic beam-steering device based on a lanthanum-modified lead zirconate titanate ceramic wafer," *Appl. Opt.* **35**, pp. 3155-3162, (1996).
4. N. Asada, "Silicon micromachined two dimensional galvano optical scanner," *IEEE Trans. on Magnetics*, Vol. **306**, 4647-4648, (1994).
5. N. A. Riza, "MOST: Multiplexed Optical Scanner Technology," in Proceedings of IEEE Annual Meeting of Lasers and Electro-Optic Society, (Institute of Electrical and Electronics engineers, 2000), pp. 828-829.
6. N.A. Riza, Y. Huang, "High speed optical scanner for multi-dimensional beam pointing and acquisition," in Proceedings of IEEE 12th Annual Meeting of Lasers and Electro-Optic Society, (Institute of Electrical and Electronics engineers, 2000), pp. 822-823.
7. N. A. Riza and Z. Yaqoob, "Ultra High Speed Scanner for Optical Data Handling," in Proceedings of IEEE 13th Annual Meeting of Lasers and Electro-Optic Society, (Institute of Electrical and Electronics engineers, Puerto Rico, 1999), pp. 262-271.
8. N. A. Riza and Z. Yaqoob, "Agile optical beam scanners using wavelength and space manipulations," Algorithms and Systems for Optical Information Processing V, B. Javidi; D. Psaltis eds., Proc. SPIE 4471, pp. 262-271, (2001).
9. Z. Yaqoob and N. A. Riza, "Free-space wavelength-multiplexed optical scanner demonstration," *Appl. Opt.*, Vol. **41**, pp. 5568-5573, (2002).
10. Z. Yaqoob, A. A. Rizvi, and N. A. Riza, "Free-space wavelength multiplexed optical scanner," *App. Opt.*, Vol. **40**, pp. 6425-6438, (2001).
11. Z. Yaqoob, J. Steedle, and N. A. Riza, "Wide Angle High Speed Large Aperture Optical Scanner," in Proceedings of IEEE 14th Annual Meeting of Lasers and Electro-Optic Society, (Institute of Electrical and Electronics engineers, San Deigo, California, 2001), pp. 262-271.
12. N. A. Riza, "BOPSCAN Technology: A methodology and implementation of the billion point optical scanner," in International Optical Design Conference, L. R. Gardner; K. P. Thompson, eds. Proc. SPIE 3482, 572-578, (1998).
13. N. A. Riza, "Digital control polarization-based optical scanner," US Patent 6,031,658, Feb.29, 2000.
14. N. A. Riza and S. A. Khan, "P-MOS: Polarization Multiplexed Optical Scanner," OSA Annual . Meeting, Orlando, USA, 2002.
15. R. J. Collier, C. B. Burckhardt, and L. H. Lin, Optical holography (New York, Academic, New York, 1971).
16. P.K. Rastogi, Holographic interferometry (Springer Series in Optical Sciences,Vol. 68, Springer, New York, 1994).
17. P. Günter, Electro-optic and Photorefractive Materials (Springer Proceedings in Physics, Vol. 18, Springer-Verlag, New York 1987).

18. S. A. Benton, "Photographic Holography," in Optics in Entertainment, C. Outwater, ed., Proc. SPIE 391, (1983).

19. J. J. Amodei and D.R. Bosomworth, "Hologram storage and retrieval in photochromic strontium titanate crystals," *Appl. Opt.*, Vol. **8**, pp. 2473-2477, (1969).

20. F. H. Mok, M. C. Tackitt and H. M. Stoll, "Storage of 500 high resolution holograms in LiNbO3 crystal," *Opt. Lett.*, Vol. **16**, pp. 605-607 (1991).

21. X. Yang and Z. Gu, "Three dimensional optical data storage and retrieval system based on phase-code and space multiplexing," *Opt. Eng.*, Vol. **35**, pp. 452-456, (1996).

22. H. Kogelink, "Coupled wave theory for thick hologram gratings," J.Bell Syst. Tech. Vol. **48**, pp. 2909-2947, (1969).

23. R. K. Yarlagadda and J. E. Hershey, Hadamard Matrix Analysis and Synthesis With Applications to Communications and Signal / Image Processings (Kluwer Academic Press, Massachusetts, 1997).

24. J. F. Heanue, M. C. Bashaw and L. Hesselink, "Recall of linear combinations of stored data pages based on phase-code multiplexing in volume holography," *Opt. Lett.*, Vol. **19**, pp. 1079-1081, (1994).

25. C. Denz, G. Roosen, G. Pauliat, and T. Tschudi, "Potentialities and limitations of hologram multiplexing by using the phase encoding technique," *App. Opt.*, **31**, pp. 5700-5706, (1992).

26. Z. Wen andY. Tao, "Orthogonal codes and cross-talk in phase-code multiplexed volume holographic data storage," *Opt. Comm.*, Vol. **148**, pp. 11-17, (1998).

27. O. M. Efimov, L. B. Glebov, L. N. Glebova, K. C. Richardson, and V. I. Smirnov, "High-efficiency Bragg gratings in photothermorefractive glass," Appl. Opt. 38, 619-627 (1999).

28. O. M. Efimov, L. B. Glebov, and V. I. Smirnov, "High-frequency Bragg gratings in a photothermorefractive glass," *Opt. Lett.*, Vol. **25**, pp. 1693-1695 (2000).

29. N. A. Riza, "Reconfigurable optical wireless," ," in Proceedings of IEEE 12th Annual Meeting of Lasers and Electro-Optic Society, (Institute of Electrical and Electronics engineers, San Francisco, 1999), pp. 262-271.

30. N. A. Riza and M. A. Arain, "Code Multiplexed Optical Scanner", *Appl. Opt.-IP*, Vol. **42**, pp. 1493-1501, (2003).

31. M. A. Arain and N. A. Riza, "3 -dimensional wide scan angle optical scanning using code-multiplexed optical scanner", *IEEE LEOS 15th Annual Meeting* (LEOS 2002) Conf. Proc. **2**, pp. 578-579, (2002).

32. M. A. Arain and N. A. Riza, "Optical Transceiver using Code-Multiplexed Optical Scanner", *IEEE LEOS 16th Annual Meeting* (LEOS 2003).

33. A. Adibi, K. Buse, and D. Psaltis, "Multiplexing holograms in LiNbO$_3$:Fe:MN crystals", in *Opt. Lett.,* Vol. **24**, pp. 652-654, (1999).

CHAPTER TWO: PHOTONICS SIGNAL PROCESSING

2.1 <u>Introduction</u>

Photonic signal processing is a branch of optics that has a broad range of applications in communications, military, aerospace, biomedicine, and test and measurement. Specifically, Radio Frequency (RF) filtering using photonics can provide powerful new capabilities over broad (e.g., tens of GHz and higher) RF bandwidths. A highly useful filter is the transversal filter that is produced by weighted and time delayed sum of the input signal for generating a filtered output RF signal such as to reject or select specific frequencies in the RF band. Specifically sort after is an electronically programmable RF transversal filter that can be rapidly programmed to adapt to the changing signal processing environment such as in adaptive antenna systems for commercial and military communications and electronic warfare and radar.

The basic element required to implement an RF transversal filter is a variable time delay module. Apart from being used in RF transversal filters, a variable fiber optic delay line (VFODL) is a highly sought after component with applications ranging from microwave/millimeter wave analog photonic signal processing to digital optical communication systems based on packet switching. The ideal VFODL is able to efficiently and continuously generate time delays with high temporal resolution over any given long time delay range. In this chapter, first a hybrid variable fiber-optic delay line capable of producing many time delay settings is introduced. Later, the analog part of the time delay unit based on chirped fiber Bragg grating (CFBG) is used to implement multi-coefficient programmable RF transversal filter in the

optical domain. In this chapter, first a VFODL is described followed by a demonstration of a reconfigirrable RF transversal filter in the optics domain.

2.2 <u>Hybrid Analog-Digital Variable Fiber-Optic Delay Line</u>

Over the years, efforts have been made to realize these VFODLs, particularly for microwave photonics applications where an RF signal riding on an optical carrier needs to be provided with a desirable delay. One way to efficiently generate many time delays over a long time delay range uses an N-bit switched binary architecture that employs 2×2 digital switches to select given binary paths connected in a serial cascade architecture.[1] Here, based on the delay range required, free-space, solid-optic, and fiber-based delay paths have been deployed in both serial and parallel switched architectures using a variety of switching technologies such as liquid crystals [2,3], Lithium Niobate-integrated-optics [4,5], micromechanics [6,7], acousto-optics [8,9], Gallium Arsenide-integrated-optics [10], and Indium Phosphide and Silica-on-Silicon-integrated-optics.[11] Because of the digital switched nature of these VFODLs, time delay resolution is quantized to a discrete value and there is a tradeoff between resolution and number of binary switched stages. In effect, getting smaller resolutions across larger time delay ranges means adding more cascading, leading to higher losses and greater module complexity. Hence a dilemma exists to get both high resolution and long time delay range. A more recent and attractive technology for generating time delays involves the use of wavelength tuning and FBGs. Initially discrete FBGs positioned along specified fiber paths were used to produce discrete time delays based on the wavelength chosen.[12,13] Later the concept was extended to use a chirped FBG to generate near continuous time delay, but over short delay range due to the fabrication size limitations of FBGs

and the laser tuning range.[14,15] To get more delay settings within an efficient structure, multi-wavelength fiber time delay processing was proposed using discrete FBGs delay segments within a serial optical switched structure.[16,17] In addition, wavelength tuning in combination with wavelength division multiplexer devices was also proposed to realize VFODLs.[18,19] So far, all these efforts, to the best of the author's knowledge, have not realized a VFODL that can deliver near continuous time delays over an arbitrary large time delay range. In this section, such a desired VFODL that solves the prior resolution-range dilemma is described.

2.2.1 Hybrid Variable Fiber-Optic Delay Line Design

Figure 2.2.1 shows one version of the proposed hybrid VFODL. The module has one electrical input port and one electrical output port from where emerges the given delayed electrical waveform riding on a delayed optical carrier. The module has two delay control ports; one to control the analog time delay while the other to control the digitally switched optical delay. Hence, the proposed structure is a cascade of an efficient digitally switched optical delay line in combination with an analog controlled optical delay line. This hybrid combination solves the earlier resolution-range dilemma as the digital delay is excellent for providing the long time delay range while the analog delay is excellent in providing the near continuous high resolution delay between the discretized delays of the switched delay line. In effect, a near continuous time delay control can be generated across a large time delay range.
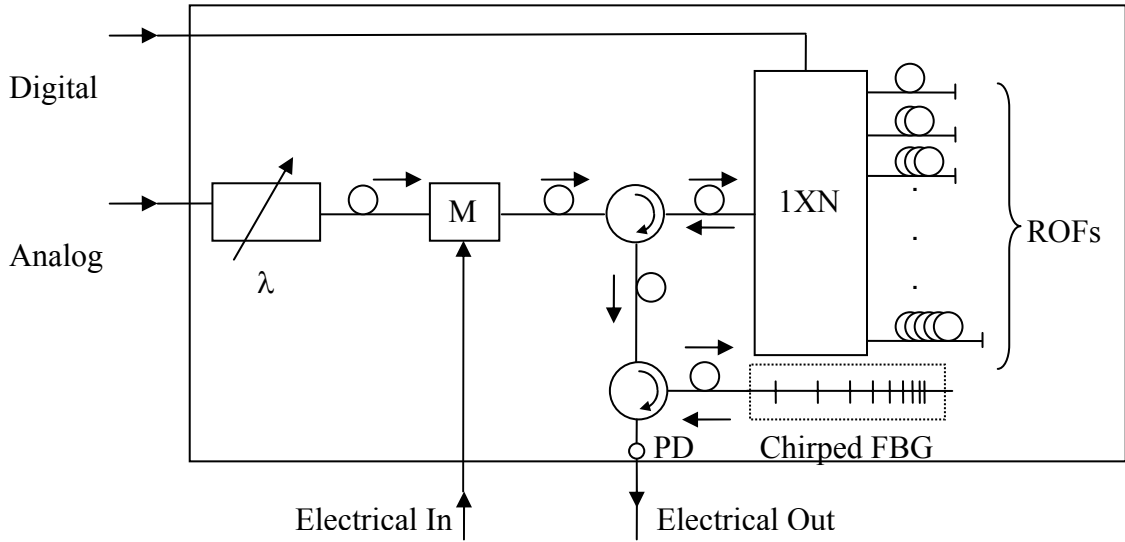
Figure 2.2.1: Schematic diagram of the proposed hybrid analog-digital VFODL realized as a parallel N-bit digital-analog time delay unit.

Earlier, proposed was the use of a wavelength sensitive delay line in cascade with a wavelength insensitive delay line to realize a hardware efficient optical beamformer.[16] In Figure 2.2.1, this same concept is extended, but with the use of a single input wavelength to realize the desired VFODL. Specifically, a wavelength sensitive chirped FBG is used in combination with precisely cut N Reflective Optical Fibers (ROFs) interconnected to a 1xN polarization and wavelength independent switch. The maximum value of time delay obtained from the analog time delay unit sets the design value for the time delay T in the digital time delay unit obtained through ROFs. If desired, it is possible to use non-fiber delays such as integrated-optic, solid-optic, and free space delays to achieve the desired results. Also, the 1xN switch can be assembled in any technology, as per requirements of the application. The digital switch operation picks a specific fiber delay to give the longer desired time delay from 0 to (N-1)T. The first fiber in the switch connections (the top one in Figure 2.2.1) acts as a reference time delay fiber. The other fibers increase in length so as to increase the time delay by T. Hence the second fiber when

44

engaged by the switch provides a T delay; similarly, the third fiber provides a 2T delay; the fourth fiber a 3T delay, and eventually the Nth fiber provides a (N-1)T delay. Tuning the laser adjusts the analog time delay over a T time delay step across any of the discrete (N-1) T time delay regions picked by the digital optical switch and thus provides a near continuous time delay from 0 to NT. Hence, the desired goal of making a VFODL with near continuous analog time delay control over an arbitrary long time delay range is realized.
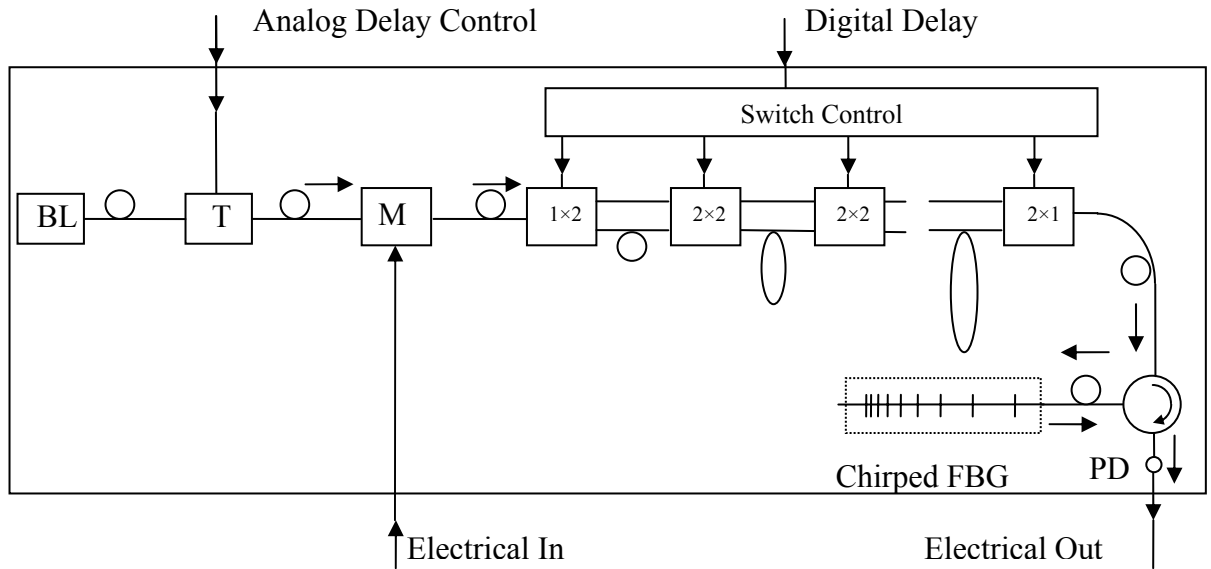
Figure 2.2.2: Schematic diagram of another version of the proposed VFODL realized as a serial N-bit digital-analog time delay unit. BL: Broadband Laser; M: Modulator; PD: Photodiode Detector.

Figure 2.2.2 shows an alternate design of the proposed VFODL. Here, wavelength selection instead of wavelength tuning of a single source is used to generate analog time delay control. One advantage of this approach is that within a given analog T delay interval, multiple time delay signals can be generated for possible signal processing uses such as transversal filtering using array signal summation. Also note that this design uses an N-bit switched binary serial delay structure versus a parallel 1xN switched structure; thus forming an efficient design

when many switched delays are required. Specifically, parallel design gives N different digital delays while an N-bit serial design with N switching stages gives the more efficient 2^N different digital delay settings.

It is well known that when light passes through some medium of non-uniform refractive index, it undergoes dispersion, i.e., different wavelength components travels with different speeds and hence there appears a time delay between propagating light signals of different wavelengths. This time delay, called the Group Time Delay (GTD), depends upon the wavelength spread of the optical signal and the properties of the material in which light waves are propagating. If we consider a fiber of length L, then the GTD is given by:

$$\tau_g = \frac{L}{V_g},$$
(2.2.1)

where V_g is the group velocity of light. It can be shown that:[20]

$$\tau_g = \tau_m + \tau_w = \frac{L}{c}\frac{d\beta}{dk_0} + \frac{L}{c}\frac{d}{dk_0}[k_0 b(n_1 - n_2)],$$
(2.2.2)

where c is the velocity of light in vacuum, λ is the optical wavelength, n_1 is the refractive index of fiber core, n_2 is the refractive index of fiber cladding, $k_o = 2\pi/\lambda$, $\beta = k_o n$, b is the material and geometry dependent constant, and n is the effective refractive index of the fiber. τ_g consists of two components; τ_m, the material dispersion delay and τ_w, the waveguide dispersion delay. In single mode fibers, τ_w is an order of magnitude lower than τ_m and is usually neglected.[21] Hence, only the material dispersion delay τ_m is considered that can be expressed as:

$$\tau_m = \frac{L}{c}\frac{d\beta}{dk_0} = \frac{L}{c}(n - \lambda_0\frac{dn}{d\lambda_0}).$$
(2.2.3)

If we have a wavelength spread of $\Delta\lambda$ in the input light signal, then according to Eq. 2.2.3, there will be a time delay between these components that can by calculated by taking the differential of τ_m with respect to the wavelength. This wavelength spread dependent time delay is given by:

$$\Delta\tau_m = \frac{d\tau_m}{d\lambda_0}\Delta\lambda_0 = L\Delta\lambda_0[\frac{\lambda_0}{c}\frac{d^2 n}{d\lambda^2}] = L\Delta\lambda_0 D_m, \qquad (2.2.4)$$

where D_m is called the material dispersion constant and is usually expressed in ps/nm/km.

Analog control of the time delay in the proposed VFODL relies upon the chirped FBG. As is well known, an FBG is a piece of optical fiber with a grating written inside it. This grating reflects a particular wavelength that satisfies the Bragg condition and is given by:[22]

$$\lambda_{Bragg} = 2n_{eff}\Lambda_g, \qquad (2.2.5)$$

where Λ_g is the grating period and n_{eff} is the effective refractive index inside the FBG. In a continuously chirped grating, Λ_g is varied continuously throughout the length of the grating. This results in different dispersion for each wavelength due to the fact that different wavelength components are reflected from different physical positions along the length of the grating. If we have a chirp of $\Delta\Lambda_{chirp}$ in the grating period, then the corresponding chirped wavelength range is given by:

$$\Delta\lambda_{chirp} = 2n_{eff}\Delta\Lambda_{chirp}. \qquad (2.2.6)$$

If we take a reference wavelength at the center of the chirped wavelength range of the grating, the time delay is expressed by:

$$\Delta\tau_{cg} = \frac{(\lambda_0 - \lambda)}{\Delta\lambda_{chirp}}\frac{2L_g}{V_g} = \frac{(\lambda_0 - \lambda)}{\Delta\lambda_{chirp}}\frac{2L_g}{c}n_{eff}$$
$$= \Delta\lambda\frac{2L_g}{\Delta\lambda_{chirp}c}n_{eff} \qquad (2.2.7)$$

where L_g is the length of the chirped grating and a factor of two appears due to the fact that the grating is traveled twice when light is reflected back in our proposed VFODL. Here we can define the grating dispersion constant as $D_{cg} = \dfrac{2L_g}{\Delta\lambda_{chirp}c}n_{eff}$. Note that in this expression, the length of the grating is also included and therefore D_{cg} is usually expressed in ps/nm. Combining Eq. 2.2.4 and Eq. 2.2.7, the total time delay due to the chirped grating can be expressed as:

$$\Delta\tau = \Delta\tau_m + \Delta\tau_{cg}. \qquad (2.2.8)$$

Usually $\Delta\tau_{cg}$ is an order of magnitude higher than $\Delta\tau_m$ because chirp gratings are designed to give high dispersion values, so the time delay is calculated using:

$$\Delta\tau = \Delta\lambda\frac{2L_g}{\Delta\lambda_{chirp}c}n_{eff} = \Delta\lambda D_{cg}. \qquad (2.2.9)$$

Equation 2.2.9 is the design equation for calculating time delays in the analog time delay unit of our VFODL. When light travel through a fiber of length L and effective refractive index n_{eff}, the absolute time delay is given by $t = Ln_{eff}/c$. But we know that the light also suffers a time delay due to the dispersion in the medium. Hence the total time delay for an ROF such as used in the VFODL can be expressed by using Eq. 2.2.4 as:

$$\Delta T = \frac{2\Delta Ln_{eff}}{c} + 2L\Delta\lambda_0 D_m, \qquad (2.2.10)$$

where ΔL is the incremental change in length of successive ROFs and ΔT is the corresponding digital time delay step. Here the second term contributes to the timing jitter associated with the digital delay unit of the VFODL. It will be shown later that this timing jitter term is negligible compared to the first term in Eq. 2.2.10, and hence is neglected for designing the digital part of the demonstrated hybrid VFODL. Therefore, ΔL can approximated as:

$$\Delta L = \frac{\Delta Tc}{2n_{eff}} \ .$$
(2.2.11)

This equation is the design equation for the digital part of the VFODL.

2.2.2 Experimental Demonstration

The VFODL in Figure 2.2.1 is designed and demonstrated in the laboratory. A mechanically tuned laser with a 1510-1600 nm tuning range is fiber-connected to a C-band (1530-1560 nm) Lithium Niobate Integrated-optic amplitude modulator. This modulator is fed by the RF signal that requires a given delay generated by the proposed hybrid VFODL. This delayed RF signal is produced by the high speed photo-diode connected to the fiber grating interconnected circulator.

The CFBG used in our experiment has an average reflectivity of 92% (loss of 0.36dB) with a bandwidth $\Delta\lambda_{chirp}$of 22.88nm at center wavelength of 1548.682nm. The value of D_{cg} supplied by the manufacturer is 35.2 ps/nm. Hence, using Eq. 2.2.9, the maximum time delay that can be achieved by this grating by tuning the wavelength is $22.8 \times 35.2 = 805.37$ ps, which agrees closely with the experimentally measured value of 800ps. Figure 2.2.3 shows the VFODL demonstrated time delay over a 800 ps range using wavelength tuning from 1536 nm to 1560 nm. The resolution of the VFODL is limited by the wavelength resolution of the tunable laser. The tunable laser with a 1ms tuning speed used in this experiment has a tuning resolution of 0.01nm which using Eq. 2.2.9 corresponds to a time resolution of 0.35ps. The measured value on oscilloscope is 0.5ps that is limited by the bandwidth of the oscilloscope and agrees well within the limitations of oscilloscope. The design N is chosen to be 32 by employing a 1×32 optical-mechanical fiber-optic switch with a 1 ms and a ±0.3 dB loss variation over all 32 switch

49

settings. The circulator connected to the switch has a three port optical loss of 1.29 dB while the circulator connected to the chirped grating has a 2.13 dB 3-port optical loss.

As the tunable wavelength is offset from 1536 nm to 1560 nm, the delay from the chirped FBG kicks in, providing the 800 ps analog fill step between the 32 digital delay steps. A designed basic step of 800ps delay is required for the digital part of the VFODL; therefore using Eq. 2.2.11, we get $\Delta L = 8$ cm. Here we have used a typical value of $n_{eff} = 1.4682$ for Corning ® SMF-28™ .[23]
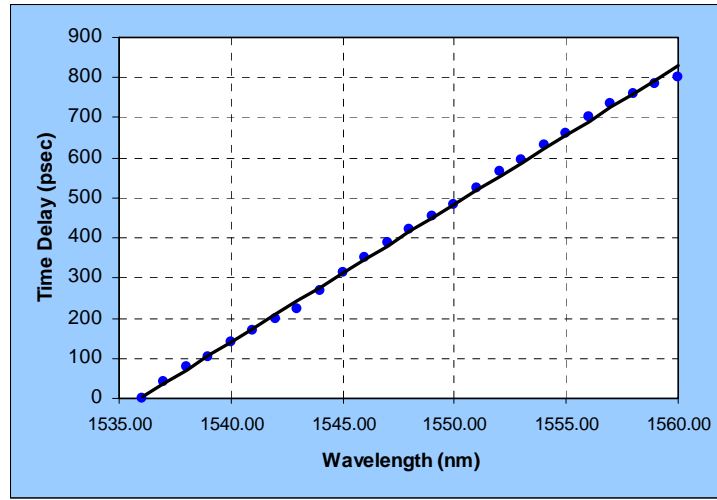
Figure 2.2.3: Analog-only mode demonstrated VFODL operation demonstrating high resolution near continuous time delay over a 800 ps range using wavelength tuning from 1536 nm to 1560 nm.

The switch port 1 is used as a reference time delay and an arbitrary fiber length of 40 cm is chosen for the VFODL design. The fibers connected to the consecutive ports are increased in length by 8 cm. This 8 cm fiber segment on double pass retroreflective delay is designed to give a 800 ps time delay. Hence, the lengths of ROFs are selected as 40cm, 40+8=48cm, 40+2×8=56cm,…,40+8×31= 288cm, for the 32 state digital part of the VFODL. Note that each ROF is a specially fabricated fiber with a gold reflective tip at its end, making a highly effective

and compact light reflector. The ROF coating is a broadband reflective coating with an average measured reflectivity of 87.5% (or optical loss of 0.7dB). By switching through the 32 switch settings, the time delay goes from 0, 800ps, 1600ps,…to 24,800ps, given that the wavelength is set for 1536 nm or alternatively from 800 to 25,600ps when the wavelength is set to 1560nm. The total optical loss of the demonstrated VFODL is 4.95dB calculated as 1.29dB (first circulator) + 2.13dB (second circulator + 0.47 dB (optical switch) + 0.7dB (ROF) +0.35dB (FBG) = 4.95dB. In effect, this loss can be further reduced by 1-2dB using lower loss and optimized components.

Table 2.2.1 shows the designed and demonstrated VFODL delays. Six switch ports, namely, port numbers 1, 2, 3, 30, 31, and 32 are engaged in the proof-of-concept measurements to demonstrate both short time delay control and long time delay control. As shown in Table 1, a combination of the digital switch setting and the laser wavelength can adjust the time delay across an entire 0 to 25.6 ns band, thus illustrating the power of the proposed VFODL.

Considering that the designed time delay step is 0.35ps due to the tuning step of the laser, a total of ~ 73,142 time delay bins can be generated across 25.6ns via the designed VFODL. This in effect is better than 16-bit VFODL realization. Because the deployed oscilloscope could measure upto a 0.5ps resolution, the demonstrated time bins capacity of the VFODL is 51,200. Figure 2.2.4 shows a sequence of time delay oscilloscope traces produced by analog plus digital mode operation of the designed VFODL. The top traces are the reference RF signal that feed the VFODL and are time aligned with the VFODL output at the wavelength of 1536nm and ROF at port 1 of switch in operation. The lower traces indicate the optically delayed signal from the VFODL. In Figure 2.2.4(a), the switch is set to engage the ROF at port 1, and the wavelength is set to 1560nm. This setting should generate a relative delay of 800ps, as indicated by the trace

markers. In Figure 2.2.4(b), the switch is set to port 2, with the wavelength set to 1547.2nm. In this case, the relative delay is 800ps from the ROF and 400ps from the wavelength sensitive delay, giving a total of 1200ps, as indicated in the traces. For the Figure 2.2.4(c) situation, the switch is engaged for port 2 and wavelength of 1553nm, generating a relative time delay of 1400ps. In this case, 800ps is from the ROF while 600ps is from the chirp FBG. In Figure 2.2.4(d), switch is set for port 3 with wavelength at 1536nm, generating a time delay of 1600ps, due only to the ROF. Finally in Figure 2.2.4(e), the switch activates port 32 with a wavelength of 1542nm, producing a total delay of 25,000ps, where 24,800ps is via the ROF and 200ps is due to the CFBG. Hence, the data indicates that via hybrid analog-digital control of the proposed VFODL, a near continuous time delay can be generated efficiently and simply over a long time delay range.

Table 2.2.1: Demonstrated VFODL design and delays.

Time Delay Range	Control Mechanism	Active Switch Port	Fiber Length at switch port
0-800psec (0 to T)	Analog (1536-1560nm)	1	40cm
800-1600 psec T to 2T	Analog+Digital	2	48cm
1.6-2.4nsec 2T to 3T	Analog+Digital	3	56cm
23.2 – 24.0 nsec 29T – 30T	Analog+Digital	30	272cm
24.0 – 24.8 nsec 30T – 31T	Analog+Digital	31	280cm
24.8 – 25.6 nsec 31T – 32T	Analog+Digital	32	288cm
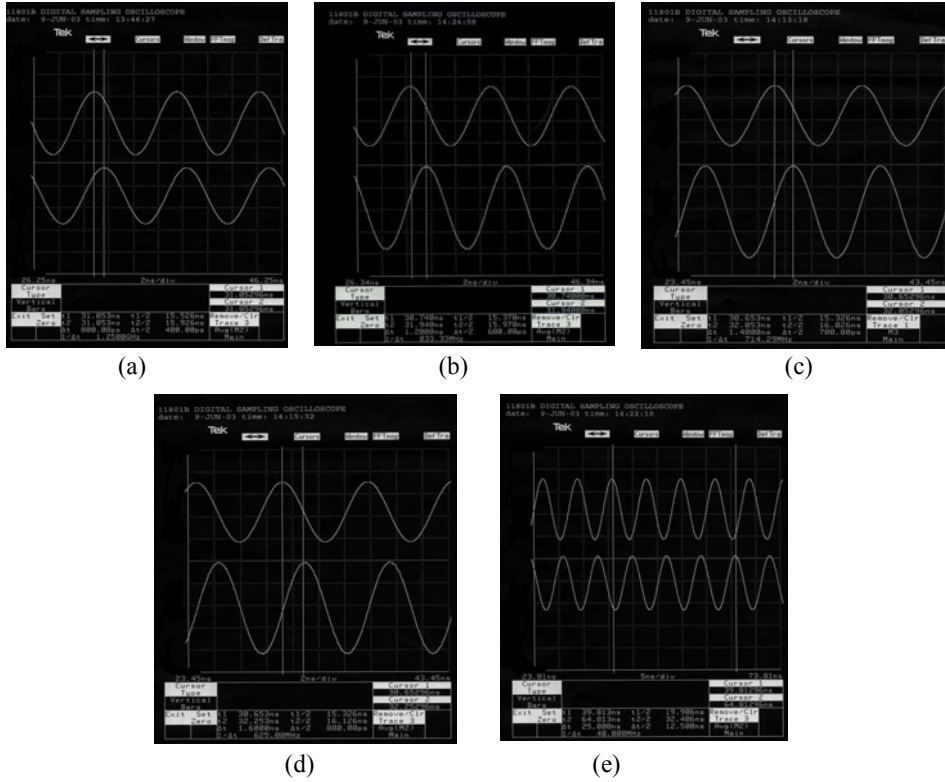
Figure 2.2.4: Proposed VFODL operations using the hybrid analog-digital mode. Top trace is the reference signal from the RF signal generator that is time aligned with the VFODL reference output for a $\lambda = 1536$nm and switch set to port 1. The bottom traces are the time delayed VFODL outputs for VFODL setting of (a) $\lambda = 1560.00$ nm and switch active for port 1 (b) $\lambda = $ 1547.20 nm and switch active for port 2   (c) $\lambda = 1553.00$ nm and switch active for port 2   (d) $\lambda = 1536.00$ nm and switch active for port 3 (e) $\lambda = 1542.00$ nm and switch active for port 32.

In the analog time delay unit, the timing jitter is due to the finite line width of the laser. The spectral linewidth of the laser used in the experiment is 220 KHz that corresponds to a linewidth of 2×10^{-6}nm. Using Eq. 2.2.4, the timing jitter associated with this line width is $\pm 2 \times 10^{-6} \times 35.1 = \pm 0.07$fs. This value is negligible in comparison to the tuning step-based resolution limit of 350fs. In the digital time delay unit, the timing jitter is associated with the material dispersion delay of the fiber. The maximum length of the fibers used is < 3m and the bandwidth is 22.88nm. Using typical values of $D_m = 17.92$ps/nm/km,[23] the timing jitter due to material dispersion is

1.23psec for a maximum time delay of 25.6ns. This corresponds to a 0.005% time jitter in the digital part of the demonstrated VFODL.

2.3 <u>Programmable Broadband Radio-Frequency Transversal Filter</u>

Over the years, a number of optical techniques have been proposed to realize programmable RF transversal filters. Early work focused on non-programmable or fixed response transversal filters using fixed weighting and time-delays via tapped optical fiber lengths.[28,29] Later various techniques were proposed to implement tunable RF transversal filters using optics. One method involves using a tunable laser to adjust the time delay tap within wavelength sensitive optics such as a precut dispersive fiber array [30,31] or a precut fiber array with multiple discrete FBG reflector segments.[32] A further improvement to this technique occurred when the discrete FBGs across the tunable laser band were replaced by compact single fiber segment CFBGs.[33,34] Other modifications include using fixed arrays with fixed chirp FBGs [35] and using a broadband laser source with tunable discrete FBGs as RF filter tuning controls.[36] Birefringent FBGs for such filters have also been deployed to reduce source coherence effect limitations on filter performance.[37] A special case of the transversal filter is the two tap notch filter where several methods have been proposed that are limited to only realize the notch goal.[38,39] So far, to the best of author's knowledge, these efforts to realize programmable RF filters via optics have been focused on achieving RF band tunability via the adjustment of the time delay values used to synthesize the filter. No effort has been made to realize an all-optical RF filter where both weighting and time delay controls are implemented via the optical hardware. Early efforts to realize this goal were made using liquid crystal (LC) optics, where

high coherence narrowband lasers were used with LC Spatial Light Modulator (SLM) implemented spatial wavefront selection leading to time and weight assignment.[40,41,42]

In general, a large number of taps is required to implement sophisticated filter algorithms. However, use of negative coefficients in the filter implementation reduces the required number of taps for a given specification. Note that certain types of filters such as practical high pass and bandpass filters can not be obtained by only using positive coefficients. Therefore, implementation of negative coefficients is highly desirable. Optical implementation of RF transversal filters is usually done through intensity-modulated optical systems as they provide a low cost, electromagnetic interference tolerant, large tap count, efficient weighting control structure.[43,44,45] However, direct implementation of negative coefficients is difficult as these power based systems can not use light intensity to represent negative coefficients. Over the years, a number of optical techniques have been proposed to realize programmable RF transversal filters with negative coefficients. An early technique to implement multi-tap negative coefficients transversal filter used differential detection.[46] This scheme is an opto-electronic approach where the positive and negative coefficients are detected by two separate photodetectors and the outputs of the two photodetectors are subtracted in the electrical domain to realize negative coefficients in incoherent or intensity-based optical systems. However, the setting of time delay taps and their weighting factors was realized by using an optical signal for each filter tap coupled with a variable optical attenuator (VOA) for power control.[47,48] This approach requires multiple laser sources, optical filters, and optical attenuators that increases the cost and size of the filter. Another approach used non-linear optical effects like all-optical wavelength conversion by cross gain saturation modulation [49,50] in a semiconductor optical

amplifier (SOA) or carrier depletion effect in laser diodes.[51,52] One of the main disadvantages of these approaches is the additional non-linear noise generated in the conversion process,[52] in addition to the fact that generation of multiple taps requires cascaded multiple fiber Bragg gratings [51] adding to the cost and complexity of the filter. Another indirect approach to produce negative coefficients is to use two separate RF-to-optical modulators.[53,54] One modulator is biased at the positive linear slope of the signal modulation transfer function while the other modulator is biased at the negative slope of the modulator transfer function. This solution requires two exactly similar modulators with the same frequency dependence of transfer function. Another limitation is the need to produce two synchronized modulating signals at high frequencies. Recently, the two modulators are replaced by one modulator but operating at two widely spaced optical bands to produce the same dual slope effect.[55] Nevertheless, multiple tap generation again requires multiple laser sources along with multiple VOAs.[54] In addition, the generation of multiple taps is limited to amplitudes between -1/3 and 1/3.[54] An alternate technique was proposed to realize negative filters by using dual-output modulators.[56,57] These techniques employ different time delay elements for every tap and hence phase noise can be a limiting issue in practical implementations. Another technique involving application specific 2×1 Mach-Zehnder modulator was proposed but again this technique requires a laser source, polarization controller, and an optical attenuator for every tap resulting in a potentially bulky and expensive RF transversal filter.[58]

In this section, a new technique relying on a broadband laser and optical spectrum control to realize an all-optical RF transversal filter is presented. Specifically, via the combination of a CFBG as explained in the earlier section, an SLM based on digital micromirrors, and a fiber-optic interleaver, a unique RF filter is realized. The proposed and demonstrated filter features a

compact high dynamic range programmable filter design that can provide high resolution RF

filter shaping for broadband RF bands.[59,60,61]

2.3.1 Optoelectronic RF Transversal Filter Theory

For a generalized finite impulse response (FIR) discrete transversal filter, the output

filtered signal *r(n)* is a weighted sum of *m* number of delayed input signal *s(n)* replicas and can

be expressed as:

$$r(n) = \sum_{m=0}^{M-1} A_m s(n - m\tau), \qquad (2.3.1)$$

where A_m is the weight of the mth coefficient of the transversal filter and τ is a time delay step

generated in the filter structure. Generally, A_m can be positive or negative depending upon the

nature of filter. The discrete time domain impulse response of such a system *h(n)* can be written

by using Delta function $\delta(n)$ as the input to the system.

$$h(n) = \sum_{m=0}^{M-1} A_m \delta(n - m\tau) \qquad (2.3.2)$$

where $\delta(n)$ represents a Fermi-Dirac delta function. The frequency response of this FIR discrete

filter can be calculated by taking the Z-transform of Eq. 2 giving:

$$H(z) = A_0 + A_1 z^{-1} + A_2 z^{-2} + \cdots + A_{m-1} z^{-(m-1)} = \sum_{m=0}^{M-1} A_m z^{-m} \qquad (2.3.3)$$

where z^{-1} represents a unit τ time delay. Note that these A_m coefficients are implemented in such

a way that there is relative time delay of τ seconds between two successive coefficients.

Therefore, in total there needs to be a total time delay of $(M-1)\tau$ between the first filter spectral

coefficient A_0 and the last coefficient A_{M-1}. Note that in the discrete domain, a signal $s(n)$ of N discrete sample values is said to be periodic with a period N if $s(n) = s(n+N)$. The corresponding discrete frequency is given by $F = \dfrac{1}{N}$. For the case of discrete filters, it is customary to present the frequency response with respect to normalized discrete frequency $\Omega = 2\pi F$ in an interval $[0, \pi]$ radian/sample. Outside this range, the frequency response of the filter is mirror image along a line at normalized frequency of π radian/sample. In other words, the response of a filter at a particular frequency of say Ω_1 radian/sample is equal to the response of the filter at $\Omega_1 + 2\pi k$ radian/sample where $k=0,1,2,3,\cdots$. The discrete domain frequency response of a filter is related to the Z-transform by:

$$H(\Omega) = H(z)\big|_{z=\exp(j\Omega)} \qquad\qquad (2.3.4)$$

The actual analog frequency f corresponding to a normalized discrete frequency Ω is given by

$f = \dfrac{(\Omega + 2\pi k) \times s_f}{2\pi}$ where s_f is the sampling frequency in sample/second or Hz. The sampling

frequency s_f in turn depends upon the basic time delay step τ and is given by $s_f = \dfrac{1}{\tau}$. Hence the

conversion of normalized discrete frequency to an analog frequency is given by $f = \dfrac{\Omega + 2\pi k}{2\pi\tau}$.

Thus, the minimum analog frequency f_0 occurring at $k = 0$ corresponding to the maximum

normalized discrete frequency $\Omega = \pi$ is is given by $f_0 = \dfrac{1}{2\tau}$ and hence depends on relative time

delay τ. The successive harmonics of f_0 given by $f_0 + k f_0$ has the same frequency response for the case of a discrete filter. This also defines the free spectral range (FSR) of the filter to be $2f_0$ as this is the unique range of frequencies in which the filter can be tuned. Hence, the transversal

filter (i.e., Eq. 2.3.1) can be used with both analog and discrete frequency representations. The experimental results shown in this paper are carried out with the analog frequency output format and represent the viability of analog filtering in the discrete domain. Specifically, the implemented RF filter uses discrete weight control and digital time delay selection to enable a discrete filter realization for analog input and output signals. In essence, the power of digital optics and digital optical processing is realized for an analog signal processing function.

There are number of methods available to calculate the value of filter tap coefficients. One widely used algorithm to calculate the filter weighting factors is the "Windowing Method". If w(n) denotes a window and the impulse response of the ideal filter is $h(n)$, i.e., the inverse Fourier transform of the ideal frequency response $H(\Omega)$, then the M number of windowed discrete filter coefficients are given by:[62]

$$b_M(n) = h(n)\, w(n). \qquad (2.3.5)$$

Rectangular, Blackman, Hamming, Gaussian, and Chebyshev are some of the commonly used windows. Note that for a generalized unity rectangular window N-tap filter, the filter frequency response is given by:

$$H(\Omega) = \frac{2 \times \sin(N\pi\Omega\tau)}{N\sin(\pi\Omega\tau)}. \qquad (2.3.6)$$

In a practical notch filter, Delta functions for sampling have a finite spatial extent. For instance, in the proposed optically implemented RF filter design, the pixelated nature of the DMD^{TM} chip in the equalizer optics produces finite size spatial sampling Delta functions. If $\Delta\lambda_e$ is the resolution of the spatial filter provided via the equalizer optics, then all the wavelengths in this range centered around the chosen wavelengths appear at the output with their respective

delays and weighting factors. The impulse response of a generalized RF transversal filter is given by:

$$h(t) = \sum_{j=1}^{N} \sum_{i=-M/2}^{M/2} A_{ji}(\lambda_{ji})\delta(t'+\tau_{ji}/2). \qquad (2.3.7)$$

Here A_{ji} is the weighting factor and τ_{ji} is the respective time delay for the ith wavelength in the jth tap. For the simple case of two-tap filter, the impulse response is given by:

$$h(t) = \sum_{i=-M/2}^{M/2} A_{1i}(\lambda_{1i})\delta(t'+\tau_{1i}/2) + \sum_{i=-M/2}^{M/2} A_{2i}(\lambda_{2i})\delta(t'-\tau_{2i}/2). \quad (2.3.8)$$

Here M is an integer limited by $\Delta\lambda_e = (\lambda_{jM/2} - \lambda_{-jM/2})$. A_{1i},τ_{1i} and A_{2i},τ_{21} are the wavelength dependent weighting factor and time delay pairs of the first and second taps, respectively. Note that tap time delays τ_{10} and τ_{20} correspond to the central wavelengths λ_{10} and λ_{20}, respectively. If we assume that the two weighting functions are made similar, i.e., $A_{1i}=A_{2i}=A_i$, as is the case because the DMD[TM] micromirror programmed window used to weight and time select the light can form two spatially similar sampling lobes, then the frequency response of the two-tap RF transversal filter obtained by Fourier transforming Eq. 2.3.7 becomes:

$$H(\Omega) = \sum_{i=-M/2}^{M/2} A_i(\lambda_i)\cos(\pi\Omega\tau_i) \quad , \qquad (2.3.9)$$

Here $\tau_i = (\tau_{1i} - \tau_{2i})$ and A_i is the weighting factor of the ith wavelength λ_i in any spatial sampling lobe as the two lobes are similar. Note that Eq. 2.3.9 gives the notch frequency $f_{null} = (2k+1)f_0$ for our proposed filter, where $f_0 = 1/2\tau_i$.

In general the response of an ideal filter with a band-limited frequency domain response is infinite in the time domain and hence needs infinite number of time delay taps to construct it. The windowing method reduces the number of required taps to M and the resultant filter is called

a filter of order *M*. Figure 2.3.1 shows a high pass filter with a cut-off normalized frequency of

0.5π radian/sample implemented using three, five, seventeen, and thirty three taps. Note that the

cut-off frequency is defined as the frequency at which the output response of the system becomes

one-half (0.5 × $H_{max}(f)$ or 10× $log_{10}(0.5)$ = -3 dB) of the maximum value $H_{max}(f)$. It is evident

that increasing the number of taps brings the actual filter response closer to the ideal response of

the filter. In short, implementation of a general RF transversal filter requires weighting control

and time delay control of a large number of taps.
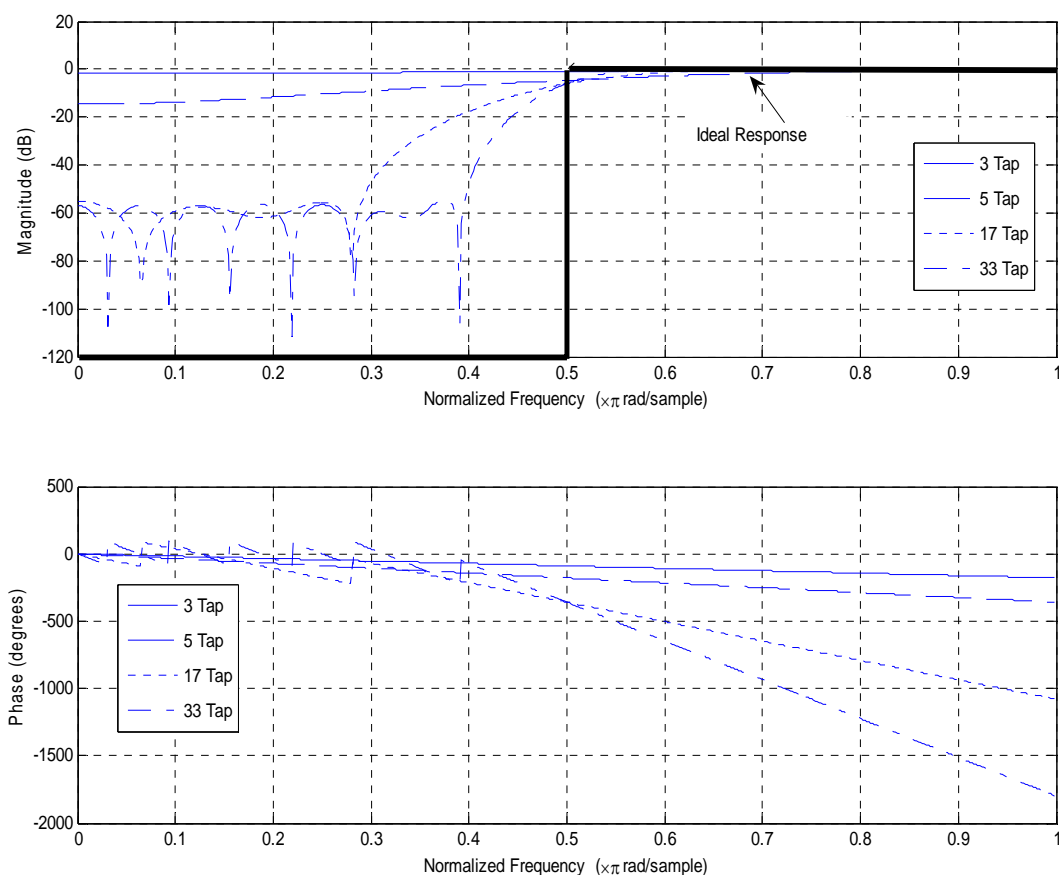
Figure 2.3.1: Theoretical plot of the magnitude and phase of the frequency response of a high
pass discrete filter with a cutoff frequency of 0.5 radian / sample using various number of taps.

61

2.3.2 Opto-electronic RF Transversal Filter Design

Figure 2.3.2 and Figure 2.3.3 show the architecture of the proposed RF transversal filter. A broadband light source (BOS) is intensity modulated by the to-be-processed input RF signal. The modulator M can be a high speed Mach-Zender interferometric waveguide modulator. The RF modulated optical signal is next fed to a CFBG via a circulator C_1. A CFBG is a piece of optical fiber with a linearly varying grating period along the physical length of the fiber. Thus each wavelength within the operational band of the grating is reflected
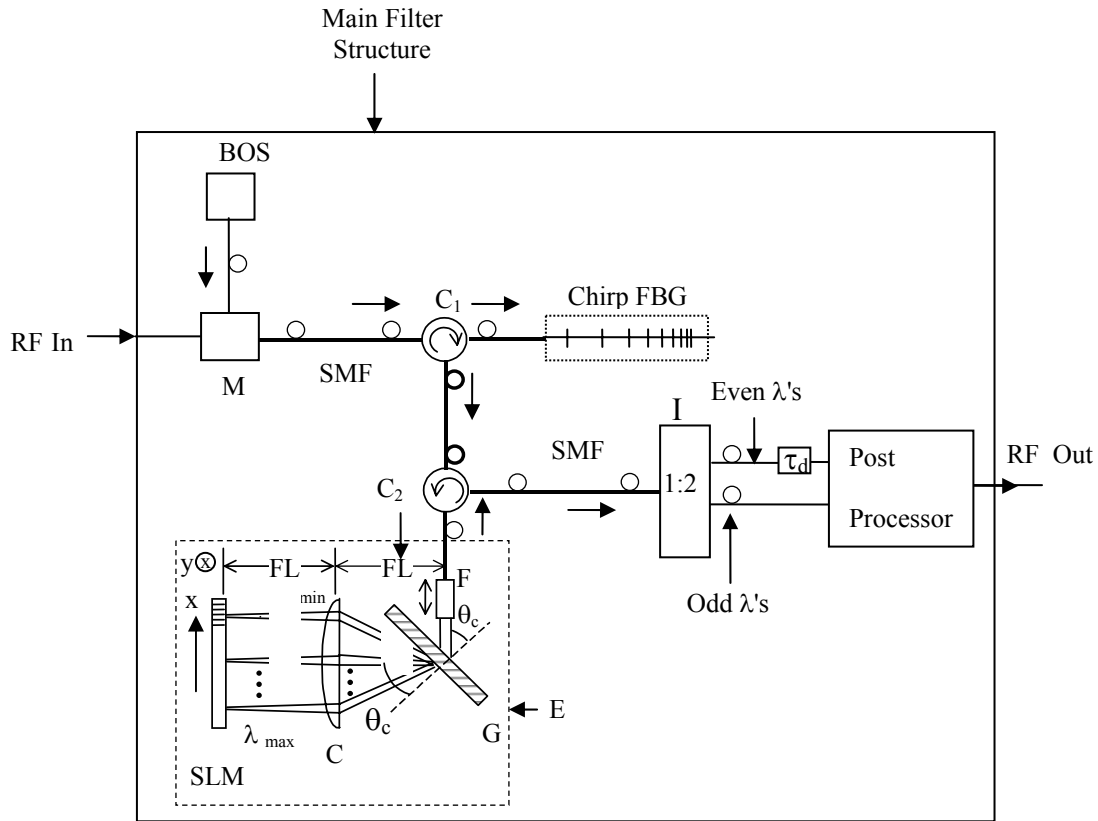
Figure 2.3.2: Proposed programmable broadband RF transversal filter using compact fiber-optics and spatial light modulator (SLM). M: High Speed Optical Intensity Modulator, BOS: Broadband Optical Source, τ_d: Fixed Path optical delay between odd and even wavelengths of the Interleaver, I: Interleaver, E: Equalizer Optics, C_1, C_2: Optical circulators, G: Grating, C:

Cylindrical lens, θ_c: Grating Bragg Angle, FL: Focal Length of C, SMF: Single Mode Fiber, F: Fiber lens.

from a different physical location along the length of the grating. This causes the different wavelength components of the optical source to acquire different amounts of time delays. The amount of time delay depends upon several parameters such as the grating length, the wavelength band of the grating, the effective refractive index of the grating medium, and the group velocity of the optical signal inside this grating medium. The RF modulated and delayed broadband optical signal next passes via the circulators C_1 and C_2 to enter optical equalization optics labeled as E. Here, a highly dispersive volume Bragg grating spatially disperses the optical spectrum which is then projected using a cylindrical lens C onto a spectrum control weight chip such as a Texas Instrument (TI) digital micromirror device (DMD^{TM}). Components of this spatially distributed optical spectrum are selectively weighted and retro-reflected from the DMD^{TM} by simple digital control of the micromirrors. This dynamic weighting and selective retro-reflection process is the key design feature of the proposed RF transversal filter. After the weighted and selected time delay signals exit from E via C_2, they are routed to a 1:2 channel wavelength Interleaver (I) that separates the even and odd wavelengths into two separate fiber channels as shown in Figure 2.3.3.(a). These even and odd wavelengths are used to represent the positive and negative weights for time delay signal pairs that are later used to synthesize via summation the transversal filter. Because the odd and even wavelengths always have a fixed time delay of τ_d between them, a fixed fiber delay of τ_d is added to the even wavelength channels before entering the photodetector PD_1. The odd wavelengths are sent directly for detection to PD_2. Hence, PD_1 and PD_2 operate with no relative RF delay. τ_d is determined by the wavelength resolution of the deployed interleaver I. Ideal design requires the wavelength resolution of I and

63

E match. The PD_1 and PD_2 RF signals representing the positive and negative weighted filter functions, respectively, of the transversal filter are subtracted electronically by the RF Differential Amplifier (DA) to produce the desired filtered RF output. Thus by changing the E settings by control of the digital micromirrors, the opto-electronic fully programmable RF filter is realized.

In the proposed filter, τ is selected by controlling the spatial modulation chip such as the DMD^{TM}. But first the chirp FBG is used to create different time delays between the different wavelength components of the light source. For efficient optical design, the source bandwidth $\Delta\lambda_s$ should be greater than the chirp FBG bandwidth $\Delta\lambda_{chirp}$. For appropriate incoherent optical summation at the photodiodes, the coherence time of the source $\Delta\tau_{coh} \ll \tau_{min}$, where τ_{min} is the minimum time delay unit between any two consecutive even or odd wavelengths selected via the DMD^{TM} across the source spectrum. Here $\Delta\tau_{coh} \sim \dfrac{1}{\Delta\upsilon} = \dfrac{\overline{\lambda_0}^2}{c\Delta\lambda_s}$ where $\overline{\lambda_0}^2$ is the mean wavelength of the source, c is the speed of light, and $\Delta\upsilon$ is the spectral line-width of the source. If $\Delta\lambda_e$ is the resolution of the filter provided via the equalizer optics, the minimum time delay provided via the chirp FBG, i.e., between any two consecutive even or odd wavelengths is given by $\tau_{min} = 2\Delta\lambda_e D_{cg}$. Here D_{cg} is the chirp FBG dispersion constant given by $D_{cg} = \dfrac{2L_g}{\Delta\lambda_{chirp}c}n_{eff}$, where L_g is the length of the chirp FBG and n_{eff} is the effective refractive index inside the chirp FBG. Hence the smallest sampling step for RF filtering is given by τ_{min} that in turn sets the maximum sampling frequency of the RF transversal filter given by $f_s = \dfrac{1}{\tau_{min}}$. Using the Nyquist criteria implies that the maximum RF frequency that can be processed by the proposed filter is

$f_{max} = \dfrac{f_s}{2}$. Any weighting factor via the DMD$^{\text{TM}}$ chip can be chosen to realize a low pass, band

pass, band reject, or notch filter for a f_{min}-f_{max} RF band. The weighting factor control or the

spectral shaping of the optical signal is done at the DMD$^{\text{TM}}$ chip after it has passed through the

CFBG. Hence any variation in the amplitude of the weighting factors of the taps due to the group

delay ripples of the linearly CFBG, variations in the reflection coefficient of the FBG, or

variations in source spectrum can be corrected using the DMD$^{\text{TM}}$ chip. Hence the proposed RF

transversal filter is highly appropriate when high precision in the control of weighting factors is

required. In generalized filter design, these weighting factors can be both positive and negative

for any given signal tap. Because intensity-based optics cannot represent negative numbers, the

proposed filter design uses a unique optical design using a 1:2 Wavelength Division Multiplexed

(WDM) Interleaver (I) device that spatially splits the spectrum into odd and even wavelengths.

By using even wavelengths for positive tap coefficients and odd wavelengths for negative tap co-

efficients, a generalized RF filter designs can be simply realized via final filter response

generated electronically via the use of a differential RF amplifier on the odd and even filter

response outputs.
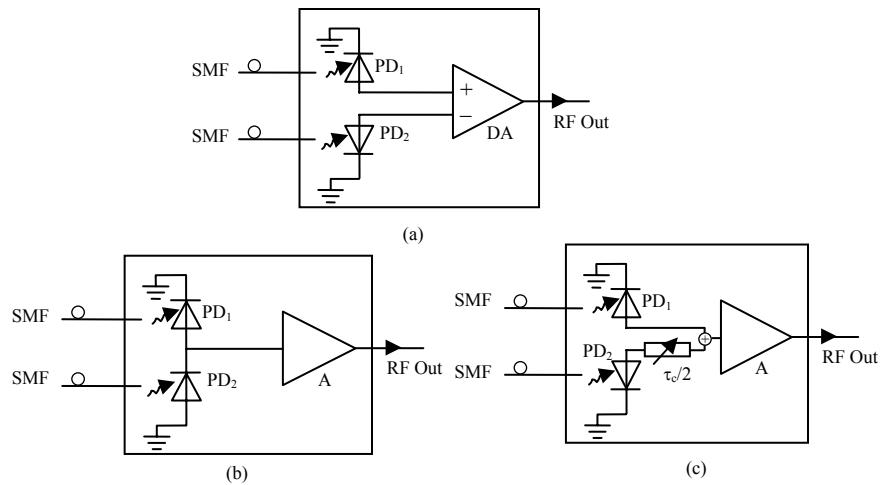
Figure 2.3.3: Post Processor optoelectronic designs to implement negative and positive weights using (a) Differential amplifier (DA), (b) interconnected dual-photodetector scheme, and (c) variable length RF delay cable for baseband operation. PD_1, PD_2: High speed photo-diodes, A: RF Amplifier.

Another approach as shown in Figure 2.3.3(b) replaces the differential amplifier by a non-differential or single input amplifier and two identical photodetectors connected as shown that gives the resultant current that is the natural difference of the two currents produced by the individual photodetectors. Thus, this operation automatically creates a negative (180^0 phase shift) on one side of the interleaver creating negative taps. This approach is a preferred approach as it will cancel any noise present between the two arms linked to the two photodetector channels. This approach also eliminates the need for a broadband differential amplifier.

Do note that the RF filters in practice usually operate as baseband devices, i.e., the modulated signal to be filtered is typically riding on a higher frequency carrier signal. Thus the actual signal for filtering has a lower bandwidth as compared to the carrier signal frequency. In this case, as shown in Figure 2.3.3(c), a fixed time delay corresponding to the carrier signal frequency can be introduced in one of the paths after photodetection. The amount of time delay should be equal to half the time period τ_c of the carrier signal frequency at f. This will introduce a 180^0 relative phase shift in one arm creating the required negative taps. This time delay element can simply be an extra cable length or a narrow-band RF phase shifter. The Figure 2.3.3(c) approach has been used in this paper for the baseband demonstration of positive plus negative coefficient filters. Next the experimental demonstration of positive tap only and multi-tap positive plus negative coefficient filters is described.

2.3.3 Two Tap Notch Filter Demonstration

As a first step for the demonstration of the proposed transversal filter, an experiment is performed to implement a two tap notch filter. The present laboratory demonstration deals with a simple 2-tap notch filter and hence a single photodetector output (from PD_1) is used and no interleaver "I" is deployed. The optical setup for the equalizer, also recently described in [63] provides a filter wavelength resolution $\Delta\lambda_e = 2.24\,\mathrm{nm}$ that in turn leads to a RF filter $\tau_{\min} = \Delta\lambda_e D_{cg} = 82.65\,\mathrm{ps}$ provided by the chirp FBG (D_{cg}=37 ps/nm), as two consecutive wavelengths can be deployed. Hence, the upper cut-off frequency of the experimental filter is $f_{\max} = \dfrac{1}{2\tau_{\min}} = 6.032\,\mathrm{GHz}$. Note that the optical filter wavelength resolution of 2.24 nm has already been experimentally demonstrated.[63] The bandwidth of the chirp FBG is 24 nm which sets the lower limit of operation of this filter as $f_{\min} = \dfrac{1}{2\tau_{\max}} = 563$ MHz ,where $\tau_{\max} = \Delta\lambda_{chirp} D_{cg}$. Here the time delay of $\tau_{\max} = 888$ ps was measured experimentally. It is important to note that the wavelength spread in the horizontal direction of the optically active processing plane of the DMD[TM] is 6.8 mm for the 24 nm bandwidth of the FBG used in this experiment. The pixel resolution of the DMD[TM] in both x and y direction is 19.5 μm. This provides a wavelength selection resolution $\Delta\lambda_{res}$ of $19.5\mu\mathrm{m} \times \dfrac{24\,\mathrm{nm}}{6.8\,\mathrm{mm}} = 0.069\,\mathrm{nm\,/\,pixel}$ in the horizontal direction via the DMD[TM] optical processor. This then corresponds to a time resolution of $\Delta\tau_{res} = \Delta\lambda_{res} \times D_{cg} = 0.06$ ps. The resultant RF frequency resolution is given by $|\Delta f| = \left|\dfrac{df}{d\tau}\right| \Delta\tau_{res} = \dfrac{\Delta\tau_{res}}{2\tau^2}$. Here τ represents the time delay between the two taps of the notch

filter. Using this relation, the resultant RF frequency resolution can be calculated. Figure 2.3.4 shows this calculated RF frequency resolution over the entire band of operation of the demonstrated filter. Here the RF frequency resolution is within 3.2% of the operating frequency.

The notch frequency can be selected anywhere in this range using appropriate time delay and wavelength selection via the digital micromirror on/off setting controls on the DMD[TM]. Specifically the weighting factors are controlled via the on/off settings of the digital micromirrors in the DMD[TM] chip in both the horizontal and the vertical direction. A measured 34.24 dB attenuation control with a resolution of 0.004 dB per micromirror or better than 13 bit control resolution has already been demonstrated.[63] The precise control of the time delays and weighting factors can be done by measuring the optical spectrum by an OSA and adjusting the on/off settings of the micromirrors. This approach provides a convenient way to calibrate the system for the in-situ experimental conditions. The worst case reconfiguration speed of the DMD[TM] is 1 ms which is the total chip setting time through a high speed serial computer interface. Hence, at present the operational speed of the proposed RF filter is 1 ms. In the ideal case, a sinusoidal response of the 2-tap notch filter is obtained when two equal power Delta function sampled optical beams are selected with some time delay between them. The exact value of the relative time delay sets the position of the notch. As mentioned earlier, the finite spectral resolution of the DMD[TM] leads to non-ideal Delta functions, and the RF filter impulse response is given by Eq. 2.3.7 for a two-tap notch filter. Here two spatial sampling lobes are generated by carefully adjusting the micromirrors in the DMD[TM] till near similar spatial (or optical spectral) lobes are observed via the optical spectrum analyzer (OSA) connected to the exit of the C_2 circulator. In effect, the first spatial lobe is centered at λ_{10}=1539.86 nm and the second spatial lobe is centered at λ_{20}=1556 nm. Furthermore, the position of the lobes selected

also sets the time delay $\tau_i = 592\,\text{ps}$ which corresponds to a null frequency of $f_{null} = \dfrac{1}{2\tau_i} = 845$

MHz.

Figure 2.3.5 shows the corresponding optical spectrum of the signal at C_2 where the wavelength axis also forms the indirect time delay axis for the RF filtering operation due to the mapping $\tau = \Delta\lambda D_{cg}$. Hence, the data in Figure 2.3.5 also shows the impulse response *h(t)* of the RF filter in the time domain.
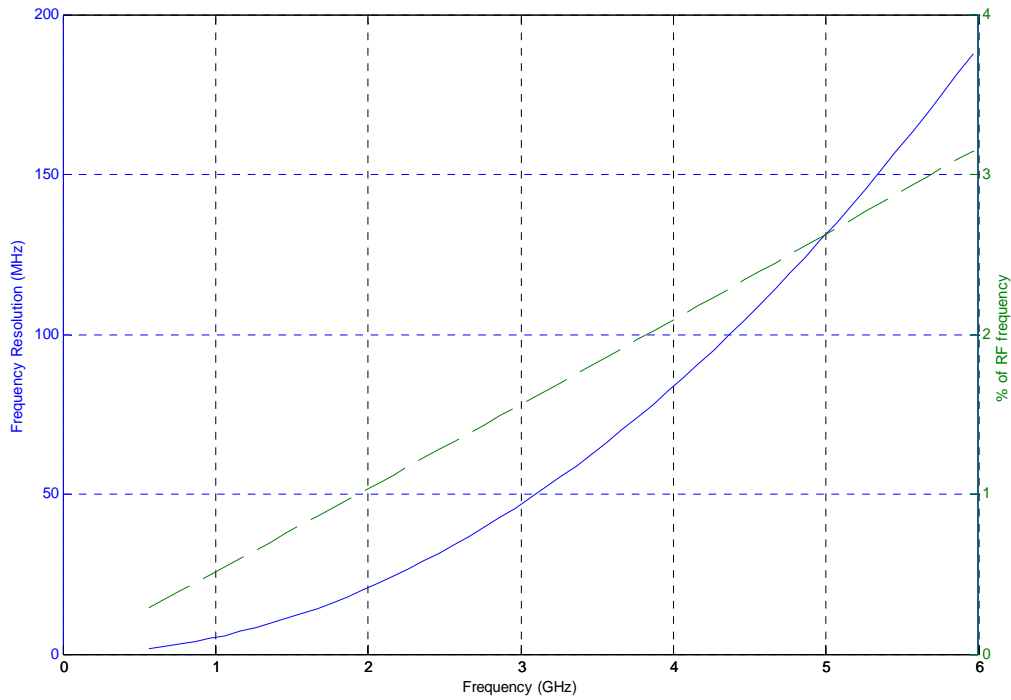
Figure 2.3.4: The calculated RF frequency resolution over the entire band of operation of the demonstrated filter. The left y axis represents the absolute frequency resolution in MHz (solid curve) and the right y axis shows the resolution in terms of percentage of the operating frequency (dashed curve).
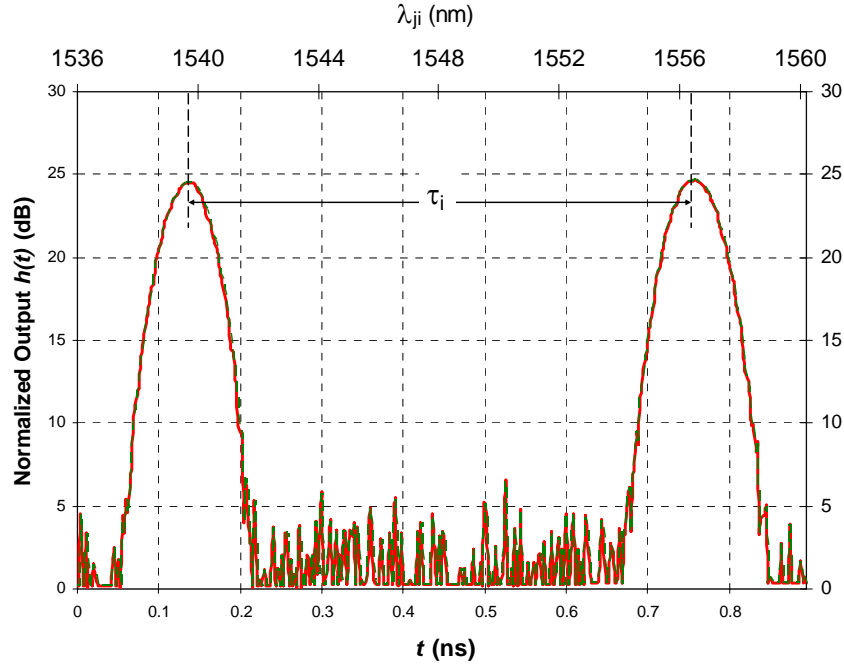
Figure 2.3.5: Time domain impulse response $h(t)$ of the demonstrated RF notch filter generated via the OSA where the upper x-axis is the λ_{ji} wavelength axis and the lower x-axis is the mapped time delay axis t.
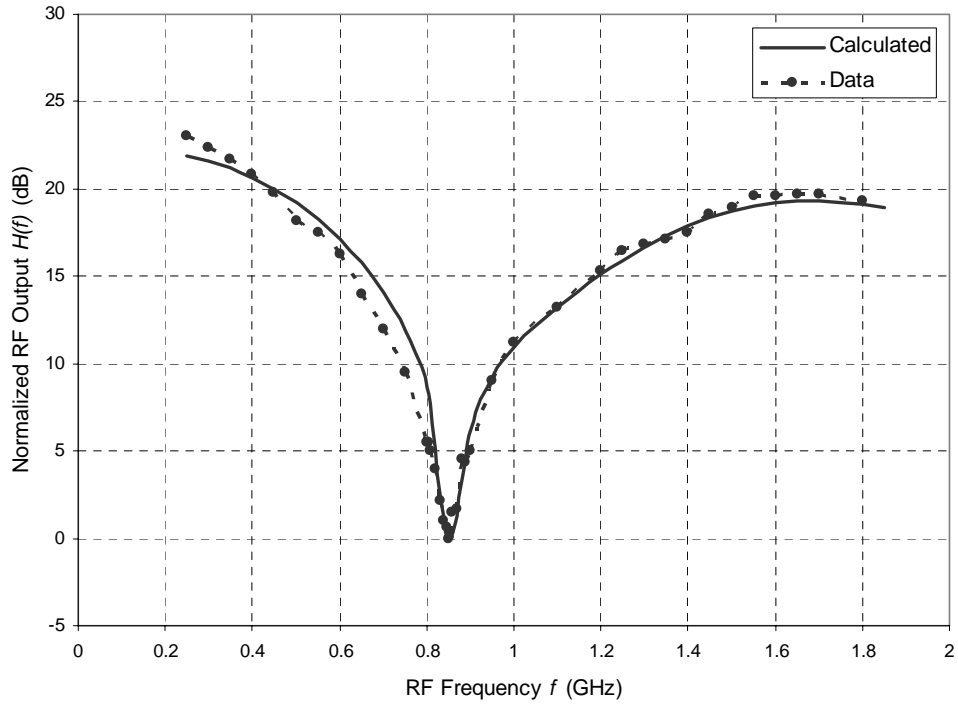
Figure 2.3.6: Frequency domain impulse response $H(f)$ of the demonstrated RF notch filter response with a null set at 845 MHz. The solid line is the calculated response of the RF filter by taking the Fast Fourier transform of the measured impulse response in time domain (i.e., shown

in Figure 2.3.5), while the dotted line is the measured frequency response taken by an RF spectrum analyzer using an RF sweep frequency input to the filter.

Frequency domain impulse response $H(f)$ can be calculated by taking the Discrete-time Fourier Transform of Eq. 2.3.8 if the weighting factors (A_{1i} and A_{2i}) and the time delays (τ_{1i} and τ_{2i}) are known. This required weighting factor and time delay data is measured as shown in Figure 2.3.5. Hence the frequency response $H(f)$ of the RF notch filter is calculated using a Fast Fourier Transform algorithm and this calculated response is shown in Figure 2.3.6 as a solid line. To verify this indirectly calculated result, the frequency response $H(f)$ of the RF notch filter is measured by applying a sweep RF signal at the modulator and measuring the output RF signal from the photodetector using an RF spectrum analyzer. This directly measured data is shown in Figure 2.3.6 as a dotted line and is in good agreement with the indirectly calculated response data.

71

Figure 2.3.7: Frequency domain impulse response $H(f)$ of the demonstrated RF notch filter response with a null set at 905 GHz showing the tunability feature of the demonstrated RF filter.

Next, the notch frequency is varied to 0.905 GHz by selecting another set of micromirrors on the DMD^{TM}. The directly measured RF filter response $H(f)$ is shown in Figure 2.3.7, indeed indicating a notch at the set 0.905 GHz frequency. These frequencies have been chosen to match the currently available RF design, test, and measurement hardware. Note that in both notch cases of Figure 2.3.6 and Figure 2.3.7, deep 25 dB notch depths are obtained via the careful weighting controls of the taps via the digital on-off operations of the micromirrors in the spatial tap. The loaded Q-factor, i.e., the ratio of the notch frequency to the 3-dB bandwidth of the demonstrated filter is measured to be 15.083. For applications demanding high Q-factor, this value can be improved by increasing the number of taps used in the experiment.

2.3.4 Negative and Positive Coefficient RF Filter Demonstrations

As a first step for the demonstration of the proposed multi-weight transversal filter, an experiment is performed to implement a seven tap all positive weight filter without the use of interleaver and using only one photodetector. The implemented filter is a seven tap FIR discrete low pass filter with a 3-dB cutoff normalized frequency of 0.3π radian/sample. The algorithm used to determine the tap weights is a Hamming window based inverse Fourier transform technique as explained in the previous section. The resultant coefficients A_0, A_1, A_2, A_3, A_4, A_5, and A_6 are 0.0087, 0.1564, 0.6610, 1.0000, 0.6610, 0.1564, 0.00870, respectively. Using a conversion $A_{m(dB)} = 10 \times \log_{10}(A_m)$ to a normalized dB scale, these coefficients in dB are $A_0 = -20.5832$, $A_1 = -8.0573$, $A_2 = -0.7982$, $A_3 = 0$, $A_4 = -1.7982$, $A_5 = -8.0573$, and $A_6 = -20.5832$. Note

72

that there exists a mapping between the wavelength and the time delay between different wavelength components. This mapping is due to the wavelength dependent time delay produced by the CFBG. This mapping is given by $\tau = \Delta\lambda D_{cg}$ where $\Delta\lambda$ is the wavelength difference from the starting wavelength or wavelength of the first weight A_0 and $D_{cg} = 37$ ps/nm is the dispersion of the CFBG. The dispersion of the CFBG is linear in the range of $1536 - 1560$ nm, as previously demonstrated in the design of the hybrid digital-analog time delay fiber-optic module using the same CFBG.[26] Figure 2.3.8 shows the implemented weighting factors of the seven tap filter. The weighting of the coefficients is measured through an OSA.
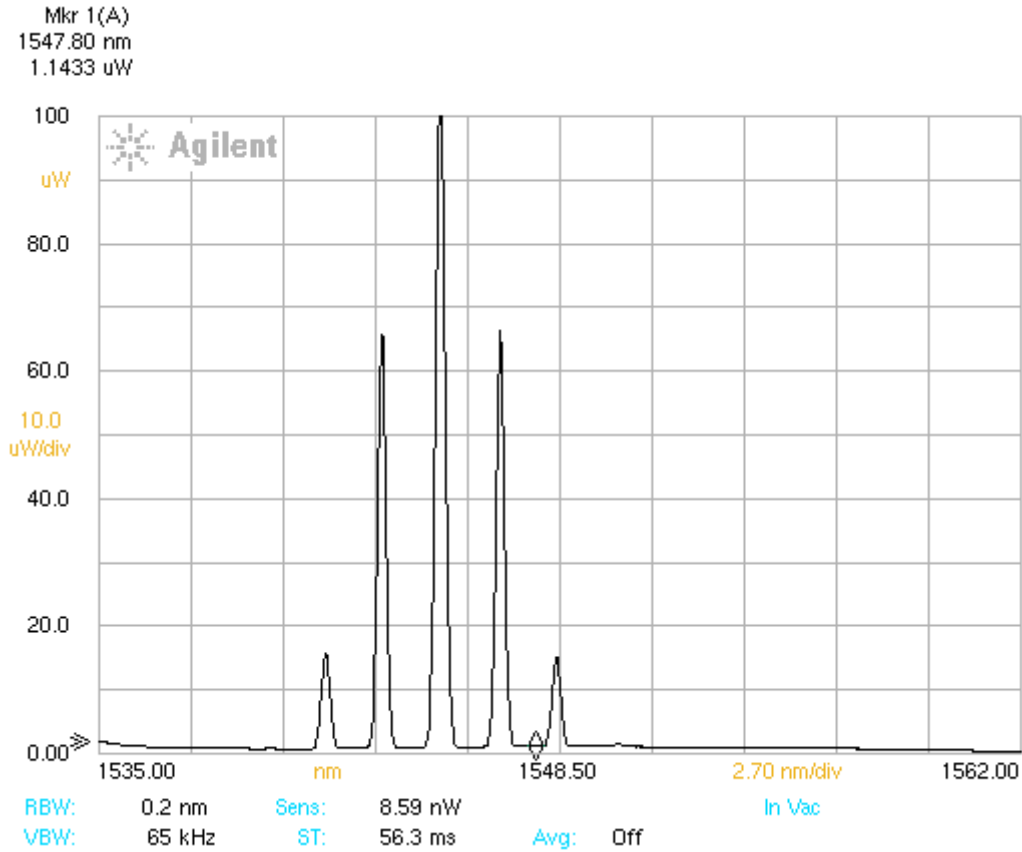
Figure 2.3.8: Optical spectrum of the DMD[TM] implemented seven-tap discrete RF low pass filter showing the strength of the seven tap-coefficients. The inter-tap wavelength gap $\Delta\lambda = 1.81$ nm which corresponds to a 66.97 ps tap delay step.

This measurement method within the RF filter design limits provides the RF filter apodization factors as the carrier (or optical) frequency is much higher than the signal (or RF) frequency. The side-bands produced during the modulation process lie within the finite extent of the corresponding optical carrier frequency lobe. For example, operating at 1540 nm, the corresponding carrier frequency is 3E8/(1540 nm) = 194.81 THz. If this carrier is modulated by a signal of 10 GHz bandwidth, the upper side-band will be at 194.82 THz. The corresponding wavelength associated with 194.82 THz is 1540.079 nm. Thus, this sideband is +0.079 nm away from the central wavelength. As the proposed minimum wavelength separation between taps is 0.8 nm >> 0.08 nm, therefore, the peak of the wavelength selected represents the apodization factor within the working resolution of OSA. For the seven taps filter, the central wavelengths chosen via the DMD^{TM} are 1540, 1541.81, 1543.62, 1545.43, 1547.24, 1549.05, and 1550.86 nm. This corresponds to a relative time delay with respect to the central wavelength of the first lobe or A_0 weight as 0, 66.97, 133.94, 200.91, 267.88, 334.85, and 401.82 ps. Hence a value of sampling time $\tau = 66.97$ ps is obtained. The corresponding analog frequency equal to the maximum normalized discrete frequency of π radian/sample is

$f_0 = \dfrac{1}{2 \times 66.97 \times 10^{-12}} = 7.470328\,\text{GHz}$. The frequency response of the filter shown in Figure 2.3.9 as dotted line is measured through an RF vector network analyzer. Because of the limited bandwidth of the amplifiers used in the experiment, only a portion i.e., 3.0-7.5 GHz of the full frequency range i.e., DC-7.474 GHz is shown. The theoretical response is shown as a solid line in Figure 2.3.9 and is calculated using MATLAB function subroutines. The two results are in agreement with each other.
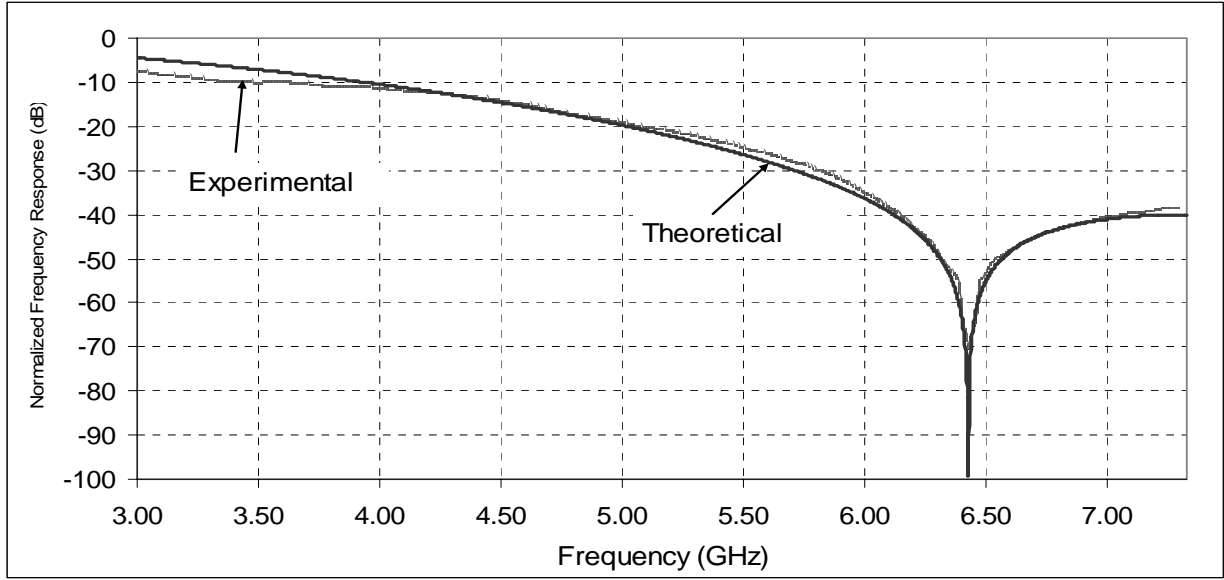
Figure 2.3.9: Frequency domain response $H(f)$ of the demonstrated seven tap low pass filter. The solid line is the theoretical frequency response of the RF filter while the dashed line is the frequency response measured by a RF vector network analyzer.

Another experiment was performed to create a two tap notch filter first with both positive taps $A_0 = 1$ and $A_1 = 1$ or [1 1]. Next an experiment is done with one positive and one negative tap of $A_0 = 1$ and $A_1 = 1$ or [1 -1]. The center wavelengths selected via the DMD^{TM} for this experiment were 1540.56 and 1546.52 nm giving $\Delta\lambda = 6$ nm. Note that these wavelengths were selected to match the standard C-band 100GHz Wavelength Division Multiplexing (WDM) Grid corresponding to a wavelength separation of 0.8 nm with 50 GHz offset corresponding to inter-channel wavelength separation of 0.4 nm so that these wavelengths could be separated by using a commercially available C-band interleaver. An interleaver separates the wavelengths into odd and even wavelengths. The two group of wavelengths coming from the two channels or arms of the interleaver have a wavelength separation of 0.8 nm among them (e.g., $\lambda_2-\lambda_0=\lambda_3-\lambda_1 = 0.8$ nm) while the wavelength separation between wavelengths of different channels is 0.4 nm (e.g., $\lambda_0-\lambda_1=\lambda_2-\lambda_1 = 0.4$ nm). Therefore if 1540.56 nm is designated as λ_0 then $\lambda_{15}= \lambda_0 + 15\times0.4$ nm =

75

1546.5 nm. The combined optical spectrum as obtained through the OSA is shown in Figure 2.3.10. Note that the two wavelengths are coming from two arms of the interleaver and are shown as two separate traces on the same graph. Note that a fixed length RF cable has been used to introduce a delay of τ_d in the even wavelength channel to time-align both even and odd interleaver wavelengths channels. The wavelength interval between these two wavelengths corresponds to a 222.0 ps time delay (i.e., = 6 nm × 37 ps/nm) that in turn sets the filter notch at 2.25 GHz with an FSR of 4.50 GHz when both taps are used as positive weights. Thus the second null frequency occurs at 2.25+4.5=6.75 GHz. In this case, the output from the two photodetectors were simply added by using a T-junction, amplified and detected via a network analyzer. The resultant frequency response is shown in Figure 2.3.11 with circular data markers.
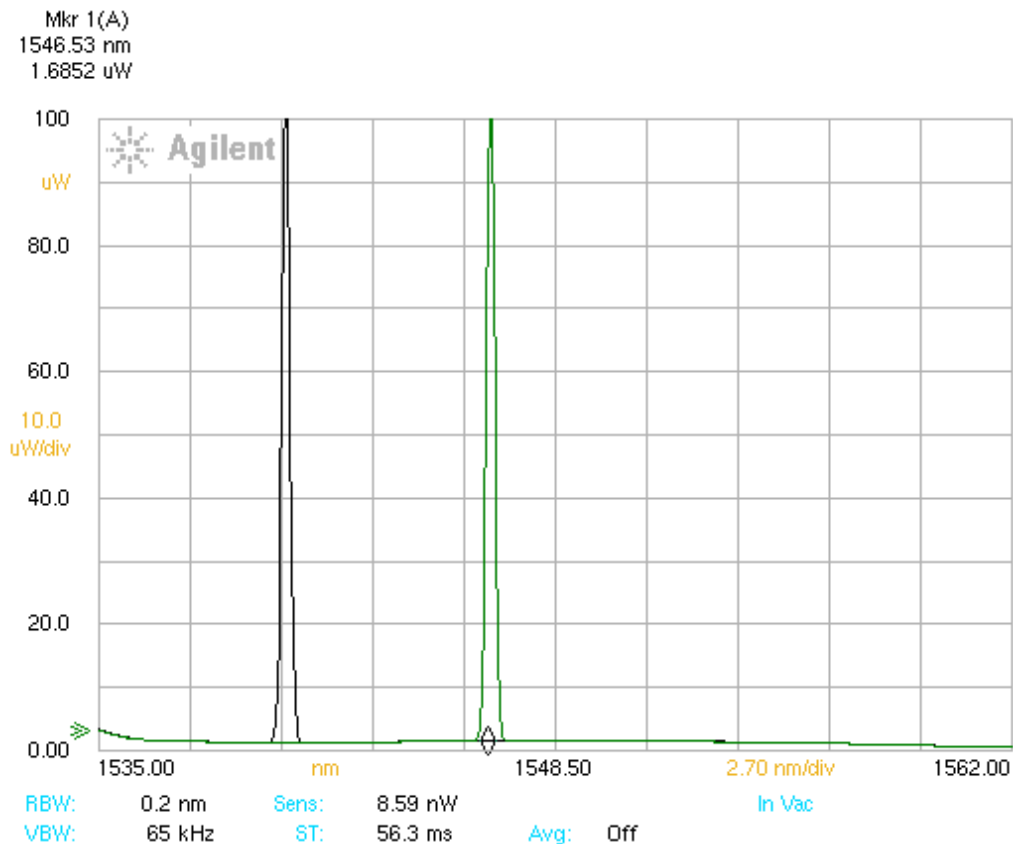
Figure 2.3.10: Optical spectrum of the DMD^{TM} implemented two-tap notch filter. The two equal power optical beams centered at 1540.56 and 1546.52 nm respectively are coming from the two arms of the interleaver.
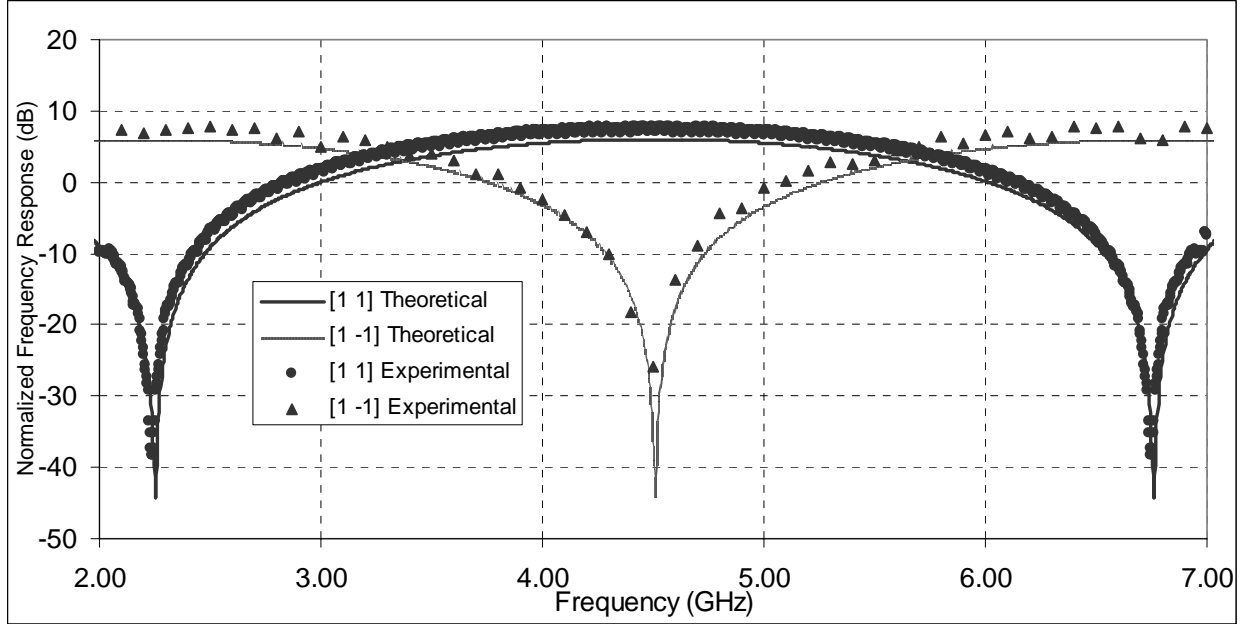
Figure 2.3.11: Frequency domain response $H(f)$ of the two tap notch filter. The solid line is the theoretical frequency response of the RF filter of the two tap positive ([1 1]) filter with notch at 2.25 GHz while corresponding measured frequency response is shown by circular data markers. The dashed line is the theoretical frequency response of the RF filter of two tap negative [1 -1] filter response with notch frequency at 4.5 GHz. The corresponding measured frequency response through an RF spectrum analyzer is shown by triangular data markers.

To test the generation of negative taps using the Figure 2.3.3(c) approach, variable length RF cables were used to introduce a 180^0 phase shift for a number of specific frequencies, starting from 2 GHz, with an increment of 100 MHz, for a total of fifty frequencies ending at 7 GHz. The 180^0 phase shift arrangement for a specific RF carrier was confirmed through the oscilloscope by ensuring that the two signals are of equal amplitude but are out of phase when the CFBG is not used. After this check, the CFBG was introduced and the output of the two photodetectors was added by using a T-junction with the given RF time delay in one of the combining arms for

negative tap generation. The resultant signal is measured through an RF spectrum analyzer. This process was performed for fifty different carrier frequencies modulating the electro-optic modulator (EOM) in the available range of designed filter frequencies. The resultant plot is shown in Figure 2.3.11 using triangular data markers along with the dashed-line theoretical plot. Note that in the case of [1 -1] filter, there is always a notch at DC or zero frequency while second notch occurs at $0+FSR = 2 \times f_0 = 4.5$ GHz as compared to the all positive [1 1] filter case. The frequency response for the [1 -1] filter case indeed shows a notch at 4.5 GHz as expected. This data demonstrates the implementation of negative taps using the proposed scheme. Note that this process was employed due to the unavailability of a broadband RF subtractor. However, these devices are commercially available with a broad spectral range of 2-38 GHz. If these devices are employed, the use of the RF delay cable can be avoided and the T-junction can be replaced by the 180^0 RF hybrid devices to perform the subtraction process.

To demonstrate multi-tap negative weight filters, another experiment was performed to implement a 13 tap FIR bandpass discrete filter with a normalized frequency 3-dB pass-band of 0.4π-0.6π radian/sample. The tap weights are found to be $A_0 = -0.0404$, $A_1 = 0.0000$, $A_2 = 0.2346$, $A_3 = 0.0000$, $A_4 = -0.7203$, $A_5 = 0.0000$, $A_6 = 1.0000$, $A_7 = 0.0000$, $A_8 = -0.7203$, $A_9 = 0.0000$, $A_{10} = 0.2346$, $A_{11} = 0.0000$, and $A_{12} = -0.0404$. The adjacent wavelength interval selected for these coefficients is 2.0 nm as per C-band 100 GHz channel-to-channel spacing so that any two successive wavelengths appear from a different channel of the C-band interleaver. The 2 nm spacing provides a filter analog maximum frequency of

$$f_0 = \frac{1}{2 \times 2\,\text{nm} \times 37\,\text{ps/nm}} = 13.34\,\text{GHz}.$$ The selected wavelengths are $\lambda_0 = 1536.61$, $\lambda_1 = 1538.58$, $\lambda_2 = 1540.56$, $\lambda_3 = 1542.54$, $\lambda_4 = 1544.53$, $\lambda_5 = 1546.52$, $\lambda_6 = 1548.51$, $\lambda_7 = 1550.52$, $\lambda_8 = 1552.52$, λ_9

$= 1554.54$, $\lambda_{10} = 1556.55$, $\lambda_{11} = 1558.58$, and $\lambda_{12} = 1560.61$ nm producing the even and odd wavelengths. The resultant optical spectrum is shown in Figure 2.3.12 indicating the non-zero weights.
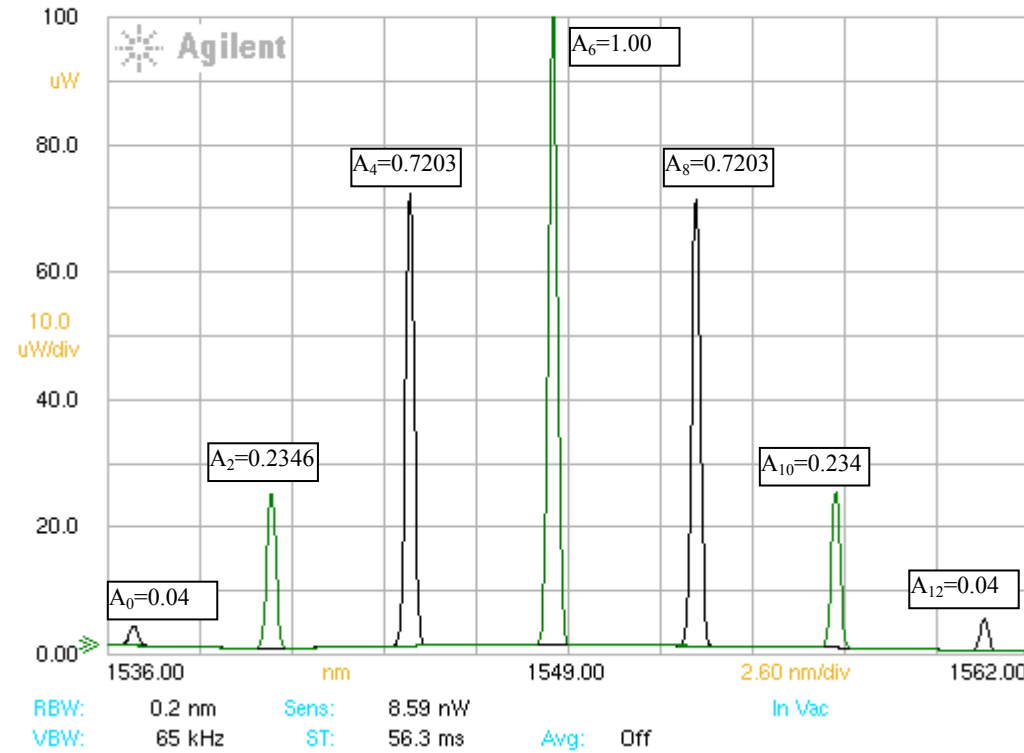
Figure 2.3.12: Optical spectrum of the DMD^{TM} implemented thirteen tap bandpass filter. The central wavelengths 1536.61, 1540.56, 1544.53, 1548.51, 1552.52, 1556.55, and 1560.61 are coming from one arm while 1538.58, 1542.54, 1546.52, 1550.52, 1554.54, and 1558.58 nm are coming from the other arm of the interleaver. Shown are 7 weights A_0, A_2, A_4, A_6, A_8, A_{10}, and A_{12} as the other weights A_1, A_3, A_5, A_7, A_9, and A_{11} are zero.

First the output of the two photodetectors is added together and the resultant RF spectrum is shown in Figure 2.3.13 with circular data markers. The results are in agreement with the theoretical values obtained by using all positive coefficients shown as a solid line. Next, the same Figure 2.3.3(c) approach of producing 180^0 phase shift through the variable RF delay cable

is employed for forty frequencies driving the EOM and the resultant RF spectrum is shown in Figure 2.3.13 by triangular data markers along with a dashed-line for theoretical response. The measured response is in good agreement with the calculated results. This check demonstrates the viability of multi-tap negative coefficient filter through the proposed approach.
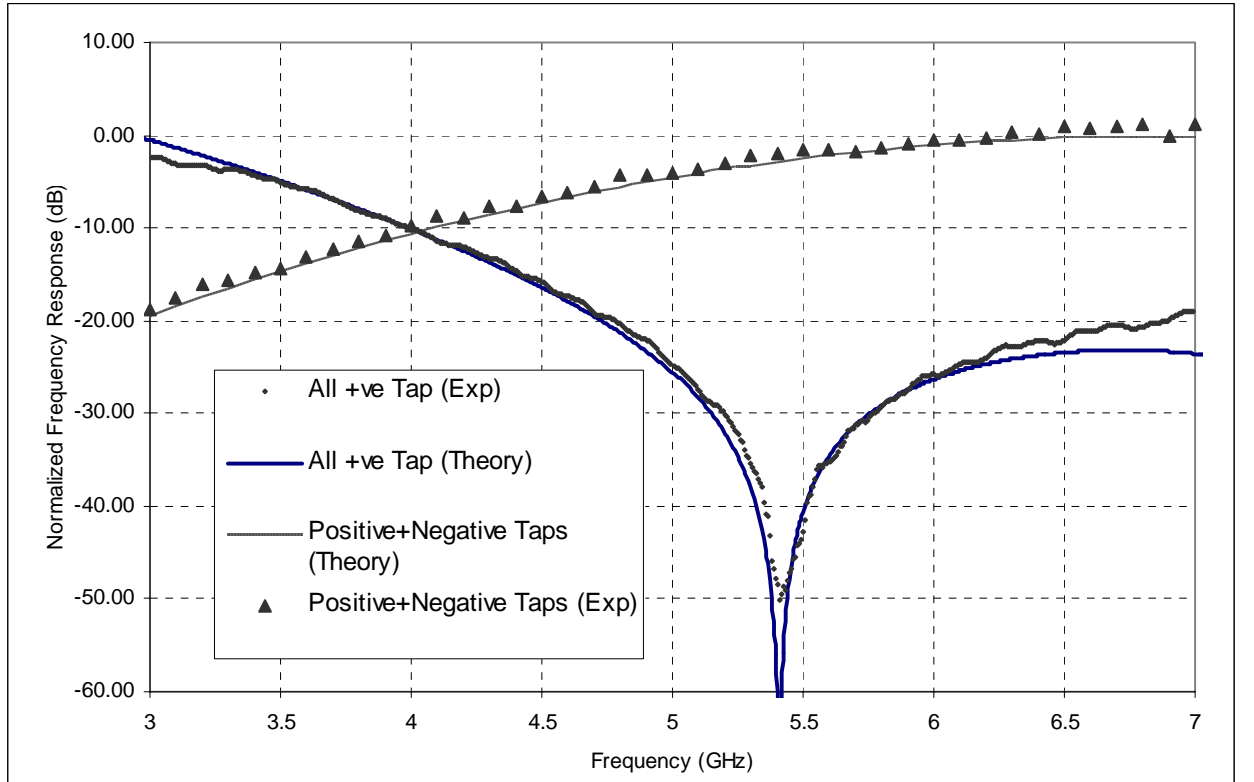
Figure 2.3.13: Frequency domain response *H(f)* of the 13 tap filter implemented in Figure 2.3.12. The solid line is the theoretical frequency response of the RF filter with all positive taps while the corresponding measured response is shown by circular data markers. The theoretical response of the filter with positive as well as negative weights is shown as dashed line while the corresponding measured response via an RF spectrum analyzer is shown by triangular data markers.

The highest frequency that can be processed using this system depends upon the wavelength selection resolution of the DMD^{TM} chip and the CFBG characteristics. Note that the

interleaver naturally acts as a filter with a minimum wavelength resolution of 0.4 nm. This 0.4

nm interval limits the maximum frequency of operation according to the dispersion of CFBG.

For the present case, this maximum frequency is given by $f_0 = \dfrac{1}{2 \times 0.4\,\text{nm} \times 37\,\text{ps/nm}} = 33.78\,\text{GHz}$,

and can be further increased by using a CFBG with a lower dispersion. The total number of taps

depends upon the bandwidth of the CFBG. In our case, the bandwidth of the CFBG is 26 nm that

translates into sixty five ($\dfrac{26}{0.4} = 65$) available taps for a minimum spacing of 0.4 nm. This

provides an ultra-high bandwidth with the flexibility of a large number of coefficients with full

control of weighting factor. It has already been shown that the DMD[TM] can provide a measured

34.24 dB attenuation control,[63] indicating the flexible design of the proposed filter in

implementing a large variety of filter shapes.

Conclusions

In this chapter begins demonstrated is an analog-digital variable optical delay line that provides the highly desirable features of near continuous high resolution time delays with a large number of time delay settings, all with the capability of producing long time delays. The design scheme is simple and uses cascading of a wavelength insensitive digitally switched optical delay line with a wavelength sensitive analog tuned optical delay line. The proposed VFODL parameters can be adapted for specific applications by selecting the CFBG and optical switch specifications. The demonstrated VFODL has successfully shown a < 0.5ps resolution over a 25.6ns time delay range with a 1ms time delay setting speed and a average 4.95 optical loss. The proposed VFODL can greatly impact applications such as phased array antenna controls, RF signal processing in the optical domain, biomedical optics, and packet switched optical communications. One application of the analog portion of the VFODL is RF transversal filter implementation using DMD^{TM} as spectrum shaping SLM. Based on analog VFODL, a fully programmable transversal filter using optics has been proposed using compact wavelength sensitive fiber optics and spatially inspired dynamic wavelength coded weighting and time selection optics. The large space bandwidth product of the SLM chip allows for generating many high resolution filter coefficients taps, both for the time domain and the weight functions of the input signal. Via the DMD^{TM} 2-D SLM, an all-optical highly repeatable all-digital and accurate filter synthesis is possible via digital micromirror controls. As a first step, the transversal filter is demonstrated as a two tap notch filter. Using the proposed filter, complex filtering algorithms such as Chebychev, Butterworth, Blackmann, and Hamming can be robustly implemented realizing a universal programmable RF filter that can be configured on demand. To conclude,

82

implemented are multi-tap positive and negative co-efficient RF transversal filters. A novel approach using a WDM C-band compatible interleaver for the realization of both positive and negative coefficients is demonstrated. A novel approach for baseband operation of the transversal filter using variable length RF cables is also presented. Using available components, upto sixty five taps can be simultaneously generated and reconfigured on demand within 1 ms. The demonstrated experiments show implementation of multi-tap notch, lowpass, and bandpass filters. A unique photodetection arrangement is proposed for implementing low-noise negative weight post processing that can be applied to any weight separated transversal filter optical design. Filter applications include signal processing for wireless communications, RF radar, laser radar, and Tera-Hertz imaging where high speed, adaptive, ultra-high bandwidth RF filters are required.

References

1. A. P. Goutzoulis, D. K. Davies, and J. M. Zomp, "Prototype binary fiber optic delay line", in *Optical Engineering*, Vol. **28**(11), pp. 1193-1202, (1989).
2. L. Pastur, S. Tonda-Goldstein, D. Dolfi, J. Huignard, T. Merlet, O. Maas, J. Chazelas, "Two-Dimensional Optical Architectures for the Receive Mode of Phased-Array Antennas", in *Applied Optics-IP,* Vol. **38** (14), pp. 3105-3111 (1999).
3. N. Madamopoulos and N. A. Riza, "Demonstration of an All-Digital 7-Bit 33-Channel Photonic Delay Line for Phased-Array Radars", *Applied Optics-IP*, Vol. **39** (23) pp. 4168-4181 (2000).
4. R. A. Soref, "Programmable time-delay devices", in *Applied Optics*, Vol. 23(21), pp. 3736-3737 (1984).
5. E. Ackerman, S. Wanuga, D. Kasemset, W. Minford, N. Thorsten, and J. Watson, "Integrated 6-Bit photonic trueitime-dalay unit for lightweight 3-6 GHz radar beamformer", in *IEEE International Microwave Symposiym Digest, Part II*, pp. 681-684 (1992).
6. G. A. Magel. T.-H. Lin, L. Y. Pang, and W. –R. Wy, "Integrated optic switches for phased-array applications based on electrostatic actuation of metallic membranes", in *Optoelectronic Signal Processing for Phased Array Antennas IV*, B. M. Hendrickson, eds, Proc. SPIE Vol. **2155**, pp. 107-113 (1994).
7. N. A. Riza and Dennis L. Polla, "Micromechanical fiber optic switches for optical networks", in *Integrated Optics and Microstructures*, M. Tabib-Azar and D. L. Polla, eds, Proc. SPIE **1793**, pp. 108-126 (1992).
8. N. A. Riza, "Acousto-optic device-based high-speed high-isolation photonic switching fabric for signal processing", in *Optics Letters*, Vol. **22** (13), pp. 1003-1005 (July 1997).
9. N. A. Riza, "Acousto-optically switched optical delay lines", in *Optics Communication*, Vol. **145**, pp. 15-20 (1998).
10. C. T. Sullivan, S. D. Mukherjee, M. K. H.- Brenner, A. Gopinath, E. Kalweit, T. Marta, W. Goldberg, and R. Walterson, "Switched time-delay elements based on ALGaAs/GaAs optical waveguide technology at 1.32μm for optically controlled phased array antennas", in *Optical technology for Microwave Applications IV and Optoelectronic Signal Processing for Phased –Array Antennas III*, S.-K. Yao, B. M. Hendrickson, eds, Proc. SPIE Vol. **1703**, pp. 264-271 (1992).
11. J. Stulemeijer, "Integrated Optics for Microwave Phased-Array Antennas", Chapter 4, Ph. D. Thesis, supervised under Prof. M. K. Smit, Technical University of Delft, Netherlands, February 2002.
12. G. A. Ball, W. H. Glenn, and W. W. Morey, "Programmable fiber optic delay line", in *Photonics Technology Letters*, Vol. **6**, pp. 741-743 (1994).
13. R. A. Soref, "Fiber grating prism for true time delay beam steering", in *Fiber and Integrated Optics*, Vol. **15**, pp. 325-333 (1996).
14. J. L. Corral, J. Marti, S. Regidor, J. M. Fuster, R. Laming, and M. J. Cole, "Continuously variable true time-delay optical feeder for phased-array antenna employing chirped fiber gratings", in *IEEE Transactions on Microwave theory and techniques*, Vol. **45**, pp. 1531- (1997).

15. A. Molony, L. Zhang, J. A. R. Williams, I. Bennion, C. Edge, and J. Fells, "Fiber bragg-grating true time-delay systems: discrete-grating array 3-b delay lines and chirped-grating 6-b delay lines", in *IEEE Transactions on Microwave theory and techniques*, Vol. **45**, pp. 1527-1530 (1997).

16. N. A. Riza and N. Madamopoulos, "Phased-array antenna, maximum-compression, reversible photonic beam former with ternary designs and multiple wavelengths", in *Applied Optics-IP*, Vol. 36 (5), pp. 983-996 (1997).

17. D. T. K. Tong and M. C. Wu, "Multiwavelength optically controlled phased-array antennas", in *IEEE Transactions on Microwave theory and techniques*, Vol. **46** (1), pp. 108-115 (1998).

18. S. Yegnanarayanan, P. D. Trinh, and B. Jalali, "Recirculating photonic filter: a wavelength-selective time delay for phased-array antennas and wavelength code-division multiple access", in *Optics Letters*, Vol. **21** (10), pp. 740-742, (1996).

19. N. A. Riza and S. Sumriddetchkajorn, "Micromechanics-based wavelength-sensitive photonic beam control architectures and applications," in *Applied Optics*, Vol. **39,** pp. 919-932 (2000).

20. A. Yariv, *Optical Waves in Crystals*, (Addison-Wesley, San Francisco, CA 1984).

21. G. Lachs, *Fiber Optic Communications*, (McGraw-Hill, USA 1998).

22. R. Kashyap, *Fiber Bragg Gratings*, Academic Press, London, UK 1999).

23. Notes on Corning ® SMF-28™ http://www.corning.com/opticalfiber/pdf/CO9562.pdf

24. G. Alibert, F. Delorme, P. Boulet, J. Landdreau, and H. Nakajima, "Subnanosecond tunable laser using a single electroabsorption tuning super structure grating", in *Photonics Technology Letters*, Vol. **9**, pp. 895-897,(1997).

25. R. Krahenbuhl, M. M. Howerton, J. Dubinger, A. S. Greenblatt, "Performance and modeling of advanced Ti:LiNbO$_3$ digital optical switches", in *J. of Lightwave Tech.*, Vol. **20**, pp. 92 - 99, (2002).

26. Nabeel A. Riza, Muzammil A. Arain and Sajjad A. Khan, "Variable Fiber-Optic Delay Line," *Journal of Lightwave Technology*, Vol. **22**, pp. 619-624 (2004).

27. Nabeel A. Riza, Sajjad A. Khan and Muzammil A. Arain, "Flexible beamforming for optically controlled phased array antennas," *Optics Communications*, Vol. **227**, pp. 301-310, (2003).

28. K. P. Jackson, S. A. Newton, B. Moslehi, M. Tur, C. C. Cutler, J. W. Goodman, and H. J. Shaw, "Optical Fiber Delay-Line Signal Processing", *IEEE Trans. on Microwave Theory and Tech.*, Vol. **33**, pp. 193-210, (1985).

29. S. Gweon, C. E. Lee, and H. F. Taylor, "Wide-band fiber optic signal processor", *Phot. Tech. Lett.*, Vol. **1**, pp. 467-468, (1989).

30. D. Norton, S. Johns, C. Keefer, and R. Soref, "Tunable microwave filtering using high dispersion fiber time delays ", *Phot. Tech. Lett.*, Vol. **6**, pp. 831-832, (1994).

31. M. E. Frankel and R. D. Esman, "Fiber-optic tunable microwave transversal filter," *Phot. Tech. Lett.*, Vol. **7**, pp. 191-193, (1995).

32. D. B. Hunter and R. A. Minasian, "Reflectively tapped fiber optic transversal filter using in-fiber Bragg gratings", *Elec. Lett.*, Vol. **31**, pp. 1010-1012, (1995).

33. D. B. Hunter, R. A. Minasian, and P. A. Krug, "Tunable optical transversal filter based on chirped gratings", *Elec. Lett.*, Vol. **31**, pp. 2205-2207, (1995).

34. R. A. Soref, "Fiber grating prism for true time delay beam steering", *Fiber and Integrated Optics*, Vol. **15**, pp. 325-333 (1996).

35. J. Capmany, D. Pastor, and B. Ortega, "New and flexible fiber-optic delay-line filters using chirped Bragg gratings and laser arrays", *IEEE Trans. on Microwave Theory and Tech.*, Vol. **47**, pp. 321-1326, (1999).

36. D. Pastor, J. Capmany, B. Ortega, "Broad-band tunable microwave transversal notch filter based on tunable uniform fiber Bragg gratings as slicing filters", *Phot. Tech. Lett.*, Vol. **13**, pp. 726-728, (2001).

37. W. Zhang, J. A. R. Williams, and I. Bennion, " Polarization synthesized optical transversal filter employing high birefringence fiber gratings", *Phot. Tech. Lett.*, Vol. **13**, pp. 523-525, (2001).

38. F. Coppinger, S. Yegnanarayanan, P. D. Trinh, and B. Jalali, "Continuously tunable photonic radio-frequency notch filter", *Phot. Tech. Lett.*, Vol. **9**, pp. 339-341, (1997).

39. J. X. Chen, Y. Wu, J. Hodiak, and P. K. L. Yu, "A novel digitally tunable microwave-photonic notch filter using differential group-delay module", *Phot. Tech. Lett.*, Vol. **15**, pp. 284-286, (2003).

40. N. A. Riza, "An optical transversal filter," U.S.A. Patent No. 5,329,118, July 12, 1994.

41. B. Moslehi, K. K. Chau, and J. W. Goodman, "Optical amplifiers and liquid-crystal shutters applied to electrically reconfigurable fiber optic signal processor", *Opt, Engg.*, Vol. **32**, pp. 574-581, (1993).

42. D. Dolfi, J. Tabourel, O. Durand, V. Laude, and J. Huignard, "Optical Architecture for programmable filtering and correlation of microwave signals", in *IEEE Trans. on Microwave Theory and Tech.*, Vol. **45**, pp. 1467-1471 , (1997).

43. K. Wilner and A. P. Van Den Heuvel, "Fiber-optic delay lines for microwave signal processing," *Proc. of the IEEE*, Vol. **64**, pp. 805-807, (1976).

44. N. A. Riza, "Optical transversal filter," US Patent No. 5,329,118 , July 12, (1994).

45. B. Moslehi, K. K. Chau, and J. W. Goodman, "Optical amplifiers and liquid-crystal shutters applied to electrically reconfigurable fiber optic signal processor", *Opt, Engg.*, Vol. **32**, pp. 574-581, (1993).

46. S. Sales, J. Capmany, J. Martí, and D. Pastor, "Experimental demonstration of fiber-optic delay line filters with negative coefficients," *Elec. Lett.*, Vol. **31**, pp. 1095-1096, (1995).

47. J. Capmany, J. Cascón, J. L. Martín, S. Sales, D. Pastor, and J. Martí, "Synthesis of fiber-optic delay line filters," *J. of Lightwave Tech.*, Vol. **13**, No. 10, pp. 2003-2012, (1995).

48. B. Vidal, V. Polo, J. L. Corral, and J. Martí, "Photonic microwave filter with negative coefficients based on WDM techniques," *IEEE Phot. Tech. Lett.*, Vol. **16**, No. 9, pp. 2123-2125, (2004).

49. F. Coppinger, S. Yegnanarayanan, P. D. Trinh, and B. Jalali, "All-optical incoherent negative taps for photonic signal processing," *Elec. Lett.*, Vol. **33**, No. 11, pp. 973-975, (1997).

50. F. Coppinger, S. Yegnanarayanan, P. D. Trinh, and B. Jalali, "All-optical RF filter using amplitude inversion in a semiconductor optical amplifier," *IEEE Trans. on Microwave Theory and Tech.*, Vol. **45**, No. 8, pp. 1473-1477, (1997).

51. S. Li, K. S. Chiang, W. A. Gambling, Y. Liu, L. Zhang, and I. Bennion, "A novel tunable all-optical incoherent negative-tap fiber-optic transversal filter based on a DFB laser diode and fiber Bragg grating," *IEEE Phot. Tech. Lett.*, Vol. **12**, pp. 1207, 1209, (2000).

52. X. Wang, L. Y. Chan, and K. T. Chan, "All-optical incoherent negative tap fiber optic delay lines using injection-locked F–P laser diode," *Proc. 1998 11th Annual Meeting IEEE Lasers Electro-Optics Society*, pp. 229–230 (1998).

53. J. Capmany, D. Pastor, A. Martinez, B. Ortega, and S. sales, "Microwave photonic filter with negative coefficients based on phase inversion in an electro-optic modulator,' *Opt. Lett.*, Vol. **28**, pp. 1415-1417, (2003).

54. S. Mansoori, A. Mitchell, and K. Ghorbani, "Photonic reconfigurable microwave filter with negative coefficients," *Elec. Lett.*, Vol. **40**, , pp. 541-543, (2004).

55. N. You and R. Minasian, "All-optical photonic signal processors with negative coefficients," *J. of Lightwave Tech.*, Vol. **22**, pp. 2739-2742, (2004).

56. D. B. Hunter, "Incoherent bipolar tap microwave photonic fiber based on balanced bridge electro-optic modulator," *Elec. Lett*., Vol. 40, pp. 856-857, (2004).

57. B. Vidal, J. L. Corral, and J. Martí, "All-optical WDM microwave filter with negative coefficient," *IEEE Phot. Tech. Lett.*, Vol. **17**, pp. 666-668, (2005).

58. D. Pastor*,* J. Capmany*,* B. Ortega*,* A. Martinez, L. Pierno, and M. Varasi, "Reconfigurable RF Photonic Filter With Negative Coefficients and Flat-Top Resonances Using Phase Inversion in a Newly Designed 2✕ 1 Integrated Mach–Zehnder Modulator," *IEEE Phot. Tech. Lett.*, Vol. **16**, pp. 2126-2128, (2004).

59. N. A. Riza and M. A. Arain, "Programmable Broadband Radio-Frequency Transversal Filter Using Compact Fiber-Optics and Digital MEMS-based Optical Spectral Control," *Appl. Opt.*, Vol. **43**, pp. 3159-3165, (2004).

60. N. A. Riza, M. A. Arain, and F. N. Ghauri, "Tunable Microwave/Millimeter Wave Transversal Filter using Retro-Reflective Spatial Photonics," International Topical Meeting on Microwave Photonics, MWP 2004, October 4-7, in Maine, USA, pp. 36-39, (2004).

61. M. A. Arain and N. A. Riza, "An Opto-electronic Approach for Adaptive Radio-Frequency Transversal Filter Implementation with Negative Coefficients using Optical Spectrum Shaping," submitted for publication in *Appl. Opt.*

62. A. Ambardar, "*Analog and digital signal processing*", 2nd ed., (Brooks/Cole Pub. Co., Pacific Grove, CA, 1999).

63. N. A. Riza and M. J. Mughal, "Broadband optical equalizer using fault tolerant digital micromirrors," *Optics Express*, Vol. **11**, pp. 559-1565, (2003), http://www.opticsexpress.org.

CHAPTER THREE: OPTICAL PATH LENGTH MEASUREMENTS USING HETERODYNE INTERFEROMETERY

3.1 <u>Introduction</u>

Optical interferometry is a useful tool in a number of applications such as thickness measurements, turbulent flows and surface structure characterization.[1,2] A number of different types of optical interferometers are available and can be selected for a particular application.[3,4] One of the main design issues in optical interferometers is mechanical and thermal instability. Another problem is the mechanical motion of optical components involved to implement scanning interferometry, which increases the phase noise and is also one of the main reasons for the low speed scanning instruments.[5,6,7,8]

Interferometers invariably are used to measure the phase difference between two optical beams. This phase difference can be due to different amounts of distance traveled by the two beams, different refractive indices of the mediums in which the two waves are traveling, or a combination of both refractive index and distance differences. The mentioned phase difference then produces a fringe pattern that can either vary in space or in time. Depending upon the fringe pattern analysis method, interferometers can be broadly divided into two categories. In one type of interferometers, the phase information is encoded in the intensity pattern and this pattern is recorded on large area detectors, holograms, or as images in a Charged Coupled Device (CCD) camera. The intensity pattern is then processed to give the phase information. The phase information contains phase ambiguity because of wrapping of the phase in the $0\text{-}2\pi$ phase interval. To avoid this ambiguity, rigorous phase unwrapping algorithms are used.[9] Also these

types of interferometers are slower because of the low speed recording process and the large image data processing requirements. Examples of these types of interferometers are homodyne Michelson type interferometer, Mach-Zehnder type interferometer, and Fizeau interferometer such as used for surface profilometry and characterization.[10,11]

In the other type of interferometer, the phase difference is measured directly. As the phase of an optical beam cannot be directly measured, the heterodyne process is used to convert optical phase data onto a lower radio frequency (RF). Examples of such heterodyne interferometers are acousto-optic heterodyne interferometers, Zeeman-effect interferometers, and dual frequency interferometers.[12,13] In all these interferometers, high speed photodetetors are used to extract optical phase data from the photodetected RF signal making these heterodyne interferometers suitable for fast temporal effect sensing applications.

In this section, a novel scanning optical interferometer is presented that uses double Bragg cell deflection approach for heterodyne interferometry in an in-line architecture. The most dominant source of noise in an interferometer is phase fluctuations introduced by air currents or temperature differences in the optical path. The proposed and demonstrated interferometer has a near common optical path so that the temperature, mechanical, and atmospheric variations affect both the signal and reference beams. Thus at the interferometer output while undergoing heterodyne detection, the unwanted phase variations are cancelled out. This particular feature of the proposed heterodyne scanning interferometer results in a low noise level. In the next sections, a number of different architectures are described for optical path length measurements, surface profilometry, and sensing applications along with proof-of-concept experiments.[14,15,16,17,18]

3.2 <u>Optical Path Length Measurements</u>

When a light beam travels equal amounts of distance through materials of different refractive indices, it accumulates different amounts of phase shifts. One measure of this total phase shift is the optical path length (OPL) between two points $P(x_1, y_1, z_1)$ and $Q(x_2, y_2, z_2)$ defined as $OPL = \int_{P}^{Q} n(x, y, z) \, ds$ where n(x, y, z) is the refractive index and *ds* is the distance traveled. If OPL is multiplied with the wave number *K*, the phase change (ϕ) is obtained. *K* is given by $2\pi / \lambda$, where λ is the wavelength in air. If the refractive index is constant in a material, which is usually the case, the OPL is calculated by measuring ϕ while a light beam passes through a material. In this case:

$$\phi = (2\pi / \lambda) \times OPL = (2\pi / \lambda)nt = 2\pi \, nt / \lambda, \quad (3.2.1)$$

where *t* is the thickness of the material. This enables the measurement of the thickness of any material if the refractive index of the material is known or the calculation of the refractive index of the material if its thickness is known. Note that usually, absolute phase difference is not of significant importance. The relative phase shift carries the required information that is either due to a time varying change in refractive index or the change in the thickness *t*. Consider a general sensing parameter *P* which induces a refractive index and thickness perturbation in a material. In this case, the phase between the reference and signal beams is given by:

$$\phi(P_1) = \frac{2\pi}{\lambda}[n(P_1)] \, t(P_1) , \quad (3.2.2)$$

where $n(P_1)$ is the refractive index when parameter P has a value of P_1 and $t(P_1)$ is the thickness at that instant. When the parameter *P* undergoes a change ΔP, the change in optical beam relative

phase $\Delta\phi(\Delta P)$ is given by:

$$\Delta\phi(\Delta P) = \frac{24\pi}{\lambda}\big[\{n(P_1) + \Delta n(\Delta P)\}\{t(P) + \Delta t(\Delta P)\}\big]$$

$$= \frac{2\pi}{\lambda}\big[\{n(P_1)\}\Delta t(\Delta P) + t(P)\Delta n(\Delta P) + \Delta n(\Delta P) \times \Delta t(\Delta P)\big]. \qquad (3.2.3)$$

Note that the higher order term Δn $(\Delta P) \times \Delta t(\Delta P)$ is a product of two small perturbations and therefore is orders of magnitude smaller than the other terms. In this case, Eq. 3.2.3 can be re-written as:

$$\Delta\phi(\Delta P) = \frac{4\pi}{\lambda}\big[\{n(P_1)\}\Delta t(\Delta P) + t(P)\Delta n(\Delta P)\big]. \qquad (3.2.4)$$

Usually external parameters do not influence the refractive index and thickness at the same scale. Specific materials can be chosen which exhibit variation in only one of the properties (refractive index or thickness) for the parameter to be measured. In this case, Eq. 3.2.4 can be simplified for the two special cases when only one of the perturbations is present. Consider the specific case when the perturbations in the refractive index and thickness of the sensing zone are not coupled together. Specifically, if the perturbations are only in the refractive index, Δt is zero and Eq. 3.2.4 reduces to:

$$\Delta\phi(\Delta P) = \frac{2\pi}{\lambda}\big[\Delta n(\Delta P)t(P)\big], \qquad (3.2.5)$$

giving the direct measure of the relevant sensing parameter change to be the change in refractive index given by:

$$\Delta n(\Delta P) = \frac{\Delta\phi(\Delta P)}{2\pi}\frac{\lambda}{t}. \qquad (3.2.6)$$

However, if the changes are only in the thickness of the material and the refractive index remains constant, then Δn is zero and Eq. 3.2.4 reduces to:

$$\Delta\phi(\Delta P) = \frac{2\pi}{\lambda} n(P_1)\Delta t(\Delta P).$$
(3.2.7)

In this case, the direct measure of the relevant sensing parameter change is the change in thickness given by:

$$\Delta t(\Delta P) = \frac{\Delta\phi(\Delta P)\lambda}{2\pi \times n(P)}.$$
(3.2.8)

The OPL change of a material can be calculated in two different ways by this technique. For measuring thickness when the material is transmissive in nature, as shown in Figure 3.2.1(a), the phase difference between the two components of light is given by:

$$\phi = \frac{2\pi}{\lambda} \times n \times t.$$
(3.2.9)

(a)

(b)
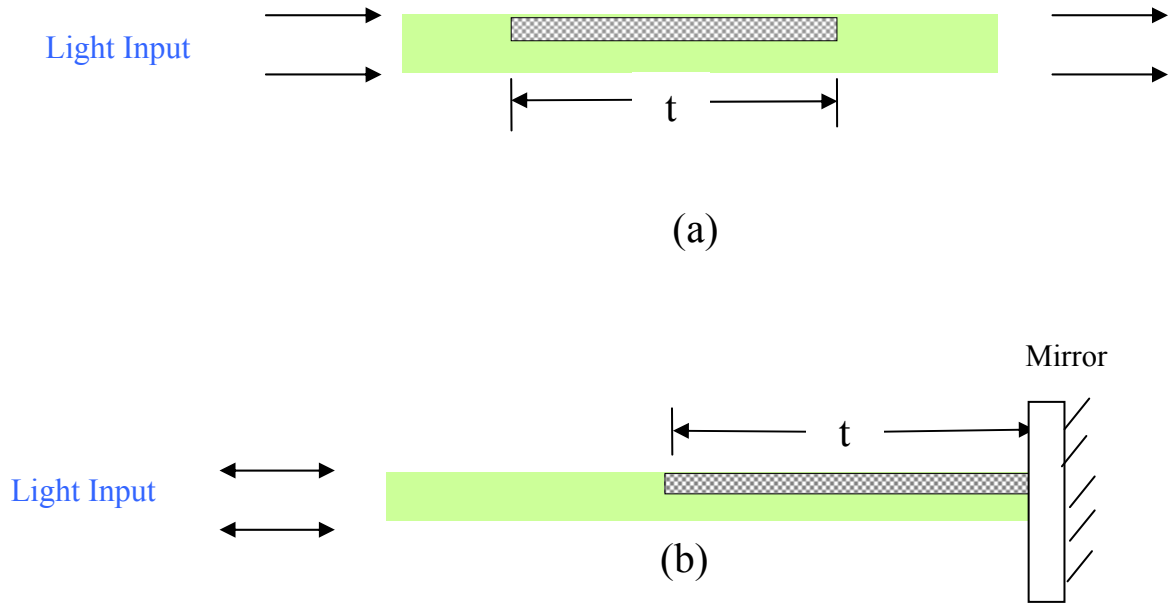
Figure 3.2.1: Geometry for calculating phase shift introduced in the two components of the optical beam by a material when it is (a) transmissive material (b) reflective material for optical path length measurement.

However if the material is reflective in nature, as shown in Figure 3.2.1(b), the refractive index of the material is not needed to calculate its thickness and the phase shift introduced by the material is given by:

$$\phi = \frac{4\pi}{\lambda} t.$$
(3.2.10)

Note that here the refractive index of the material is not needed as the beam does not pass through it. Therefore, depending upon the geometry of the sensing element, an appropriate expression for the OPL change is selected that produces an RF phase change in the detected heterodyne signal. This detected phase change in the RF signal via a lock-in amplifier or phase meter gives the measurement of the respective parameter.

3.3 Theory of Design of Heterodyne Interferometer

The electric field of an optical wave with a wavelength of λ can be expressed as:

$$E(t, r) = E_{max} \, e^{j(2\pi vt - k \cdot r)}.$$
(3.3.1)

Here E_{max} is the maximum amplitude, v is the optical frequency, $k = 2\pi n/\lambda$ is the wave vector where n is the refractive index of the medium in which wave is traveling and r is the coordinate axis dependent unit vector of the point in space where the electric field is to be expressed. When comparing two electric fields, it is customary to suppress the space dependency, i.e., $k \cdot r$ term in one of the electric fields as the coordinate axis can be fixed arbitrarily. Hence an electric field can be expressed as $E_1(t) = E_1 e^{j(2\pi vt + \alpha)}$ where α is the optical phase with respect to the reference phase. In general, the light output from an Acousto-optic Device (AOD) such as in Figure 3.3.1 consists of an undiffracted DC beam of magnitude E_{dc} and a +1 order positive

Doppler shifted diffracted beam of magnitude E_d. Note that the relative amplitude of the two beams can also be controlled by selecting the input beam incident angle on the AOD. The diffraction efficiency of an AOD is given by:

$$\eta = |E_d|^2 / |E_{dc}|^2 = \sin^2(\sigma/2), \qquad (3.3.2)$$

where $\sigma \equiv 2\pi\Delta nL / \lambda \cos(\theta_o)$ and L is the length of the acousto-optic interaction and θ_o is the input beam incident angle. The Doppler shifted +1 order beam can be expressed as $E_d(t) = E_d e^{j(2\pi vt + 2\pi ft + \beta)}$ where f is the Radio Frequency (RF) drive frequency of the AOD while β is the relative phase shift with respect to the reference phase. Note that the diffraction efficiency can be made flat over a range of wavelengths by appropriately selecting the parameters of the AOD. For the proposed Figure 3.3.1 interferometer design at a given wavelength, the +1 order beam and the DC beam are retro-reflected and pass through the AOD again while preserving the Bragg angle condition. A variety of sensing schemes can be selected for specific applications. In all cases, a mirror or a sensing element reflects the light back to the AOD. Hence a second deflection takes place and the +1 order beam undergoes double diffraction and becomes in-line with the undiffracted DC beam. This (+1,+1) double diffracted beam is given by:

$$E_2(t) = E_2 e^{j(2\pi vt + 4\pi ft + \beta)}. \qquad (3.3.3)$$

Next, the DC and the double diffracted beams undergo heterodyne detection via a high speed photo-detector. The resultant RF signal is detected by a high speed photodetector and is given by:

$$
\begin{aligned}
i(t) &\propto |E_1(t) + E_2(t)|^2 = \{E_1(t) + E_2(t)\}\{E_1(t) + E_2(t)\}^* \\
i(t) &= C\left[E_1^2 + E_2^2 + E_1 E_2 e^{j(\alpha - 4\pi ft - \beta)} + E_1 E_2 e^{-j(\alpha - 4\pi ft - \beta)}\right]
\end{aligned}
\qquad (3.3.4)
$$

94

The first two terms are DC terms and hence can be filtered out as DC bias. Using Euler's identity, Eq. 3.3.4 reduces to:

$$i_f(t) = 2CE_1E_2 \cos(4\pi ft + \beta - \alpha). \quad (3.3.5)$$

Here, $\beta-\alpha = \frac{2\pi}{\lambda} \times OPL$ between the two beams. The value of this OPL depends upon the geometry and design of the system as explained in the earlier section. The information of OPL information is encoded in the phase of the detected signal and hence if a lock-in amplifier is used, the phase of the signal can be measured and the optical path length can be determined if a desired RF phase reference is present. The generation of reference RF phase can be produced in two ways.

1. External Reference Phase Generation

2. Internal Reference Phase Generation
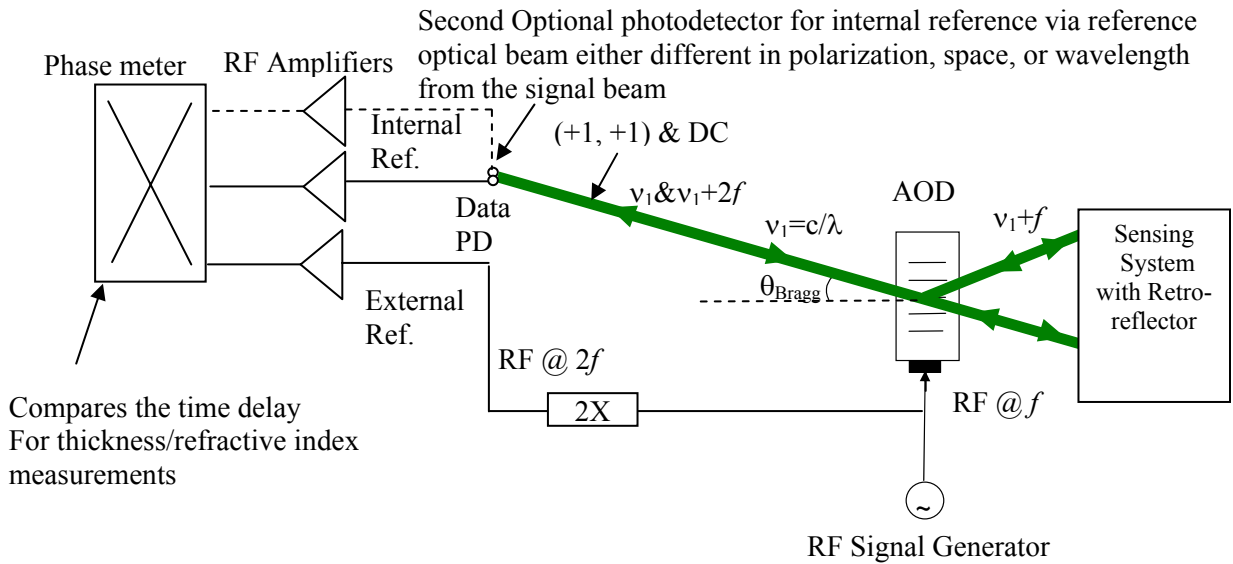
Figure 3.3.1: Generalized Heterodyne Scanning Interferometer for high precision optical path length measurements showing both internal and external reference schemes.

3.3.1 External Reference Phase Generation

The external phase generation is preferred for low noise environment. The lock-in amplifier needs a stable reference phase for phase measurement. One approach is to pass the signal from RF signal generator through a frequency doubler and feed this as reference phase signal to the lock-in amplifier. The other approach is to use another signal generator operating at $2f$ and phase locked to the signal generator driving the AOD. Note that this system is less immune to noise as the noise in the signal is due to the thermal and vibrational stresses produced in the free space path and the reference phase does not have same correlated noise. However, for low noise environments, this method can be employed.

3.3.2 Internal Reference Phase Generation

Internal reference phase can be generated by the Figure 3.3.1 system for high precision measurements in noisy environment. This is done by using another optical beam either with a different polarization, wavelength or special location but close to the original data signal beam. This is explained later in the specific interferometers. Here, another beam is subjected to same double diffraction through the same AOD but do not pass through the sensing element and hence does not acquire a varying phase. Instead it can be reflected from reference optical quality mirror. In this manner, the reference optical beam passes through the same optics/optical path (except the sensing element) and hence has same correlated noise after heterodyne detection. When this signal is compared with the data signal, phase change due to correlated noise is cancelled out thus realizing high stability, low noise and high precision heterodyne interferometer.

Another important aspect of the interferometer is the scanning capability of the proposed

architecture. Here scanning is done electronically via changing the AOD drive frequency. In our

application, we operate in the Bragg regime where just one diffraction order, e.g., first order is

produced. In this regime, the angle θ_i between the incident optical beam and the acoustic grating

must be fixed to a particular value θ_b. This angle called the Bragg angle is dependent on λ, the

optical wavelength in the air, and f, the RF signal frequency, which is chosen through the Bragg

equation:

$$\sin(\theta_b) = \frac{f_b \lambda}{2V_a},\qquad (3.3.6)$$

where V_a is the acoustic velocity in the Bragg cell and f_b is the Bragg frequency. This is shown

in Figure 3.3.2.
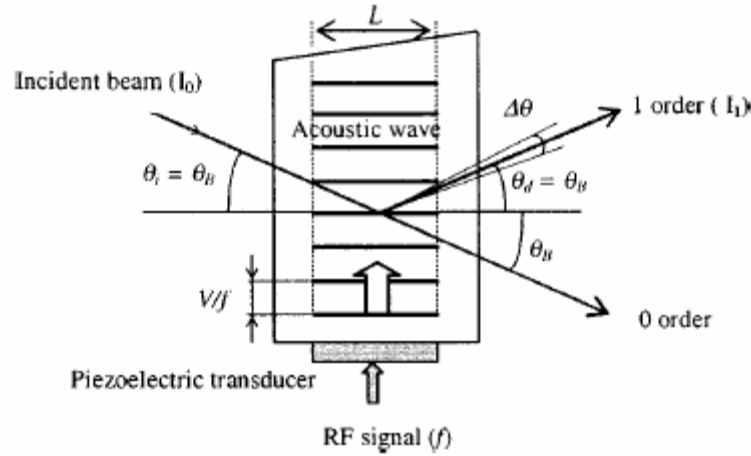
Figure 3.3.2: Acousto-optic cell used as a deflector in the Bragg regime. The piezoelectric transducer is connected to an RF generator.

As seen from Figure 3.3.2, the deflected first order beam is also at an angle $2\theta_b$ from the

transmitted beam. If the RF drive frequency is changed from f_b to some other value, the deflected

beam is deflected at another angle other than $2\theta_b$ within the range ($\Delta\theta$) thus realizing an efficient

method of scanning. Note that changing the deflection angle also changes the diffraction efficiency, but AODs with wider coverage are commercially available where the diffraction efficiency stays flat over a considerable frequency range. Usually, a spherical lens of focal length FL is used after the AOD that makes the undiffracted DC beam and the +1 order beam parallel to each other. Now the change of frequency results in a linear displacement instead of angular displacement. The scanning distance covered by the laser beam in such a geometry is given by $\Delta x = \{ \theta_{stop} - \theta_{start} \}$ FL where θ is given by θ (mrad) = [λ (μm) $\times f$ (MHz)] / V_a (mm/ μs). Next, various configurations of heterodyne interferometer are described.

3.4 Space Multiplexed Heterodyne interferometer Design

Figure 3.4.1 shows the proposed scanning heterodyne optical interferometer for reflective optical sensing applications. The basic architectural and component simplicity gives this proposed interferometer exceptional mechanical and vibrational stability. To form a high speed non-mechanical scanning interferometer, it is critical to keep the processed output beams fixed at the heterodyne detector location. In the design shown in Figure 3.4.1, this task is accomplished by using double Bragg cell diffraction in the system. In effect, double diffraction via the single Bragg cell prevents the scanning beam from moving at the detector plane. Next the operational setup of the demonstrated interferometer is described.
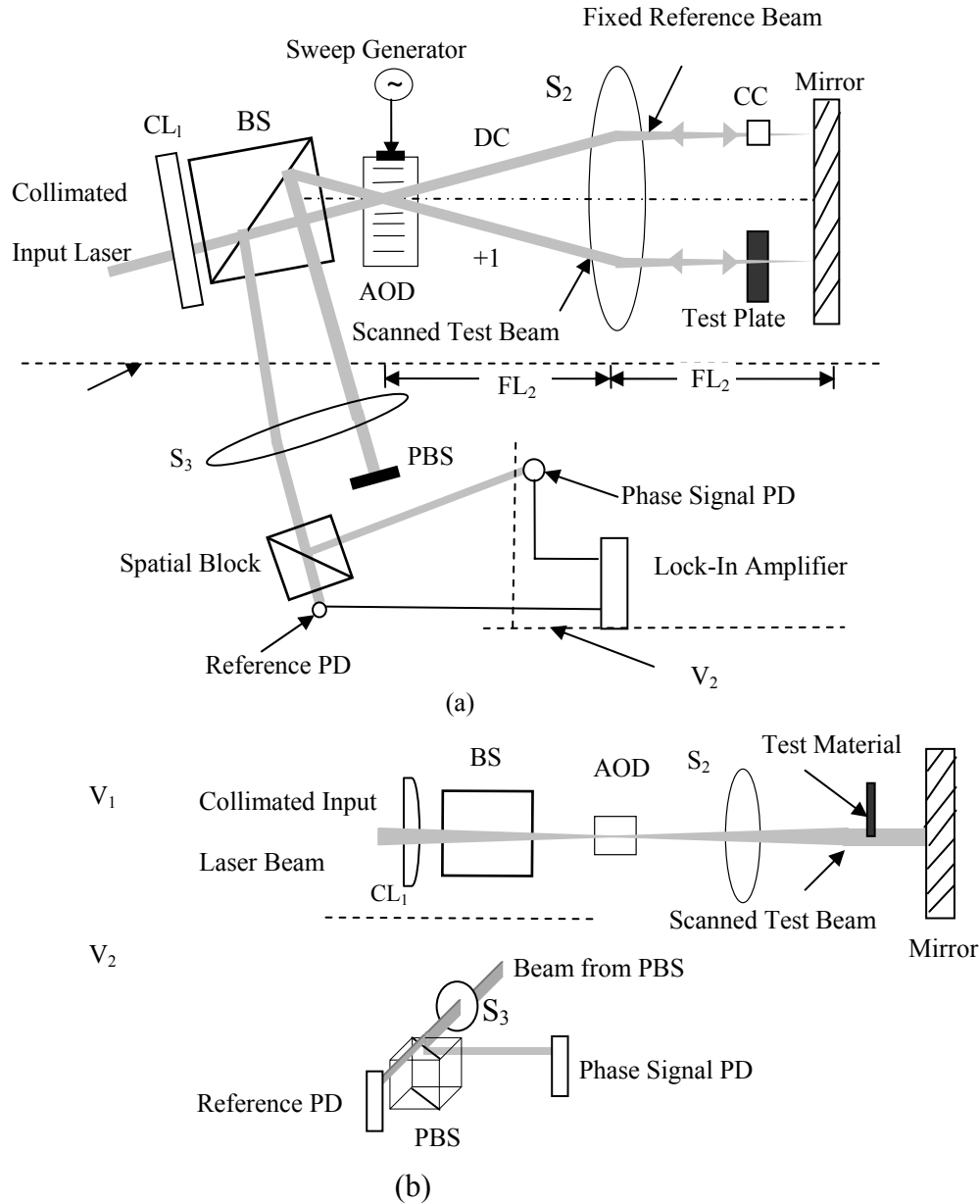
Figure 3.4.1: Top view and side views of the reflective design novel scanning heterodyne optical interferometer (a) Top View (b) Two views at SV_1 and SV_2 planes shown in (a). Here V: View, CC: Calibration Cell, BS: Beam Splitter, PBS: Polarization Beam Splitter, and PD: Photodetector.

Vertically or s-polarized light from a 514.5 nm Argon-ion laser passes through a spatial filter assembly consisting of an X40, NA 0.65 objective lens and a 10μm pin hole. A 10 cm focal length lens S_1 is used to collimate the light. Using a 30 cm focal length cylindrical lens CL_1, the

collimated light is Bragg-matched as a horizontal line in the AOD. Light after passing through

the cylindrical lens passes through a beam splitter. The AOD used is a flint glass Bragg cell with

a center frequency of 70 MHz and a 3-dB bandwidth of 40MHz. The active AOD aperture is 39

mm × 2mm with an access time of 10 μs. The AOD is driven by a HP 83752A frequency

synthesizer coupled with an IntraAction PA-4 power amplifier with a 40 dB gain. The light

output from the AOD consists of an undiffracted DC and +1 order positive Doppler shifted

diffracted beam. These DC and +1 order beams then pass through a lens S_2 of focal length FL_2

which is placed at a distance of FL_2 from the AOD. These beams after passing through the lens

become parallel to each other. A mirror is placed at a distance equal to the focal length of the

lens from S_2. The light on the mirror is a vertical line. The DC beam acts as a reference, while

the +1 order beam acts as the scanning beam (see Figure 3.4.1(b). The test medium is inserted in

the upper half of the scanning beam. Thus, the upper half of the scanning beam undergoes a

different phase shift than the lower half of the beam. The phase difference between the two is

calculated using $\phi = 2\pi n t / \lambda$ and is given by $\varphi = 4\pi (n-1) t / \lambda$. Here the phase difference is

twice the transmissive measurement case because the light passes twice in the test medium. After

applying the frequency sweep signal, only the DC and the (+1,+1) double diffracted beams

remain stationary on the photodetector. On the other hand, the other diffracted beams do not

remain stationary and are blocked by a spatial block. A polarization beam splitter (PBS) is used

to separate the reference beam and the signal beam pair containing the phase information. The

PBS is placed such that the upper portion that contains the phase delayed beam does not pass via

the PBS and hence passes without deflection to the photoreceiver, while the lower portion that

acts as a reference signal undergoes a 90° deflection. In this way the two beams are spatially

separated. The lower signal generates the 2*f* frequency phase reference signal for the electronic

phase meter, while the heterodyne detected 2*f* frequency signal coming from the top contains the phase data. Both the reference phase and the test medium phase 2*f* frequency signals are fed to the electronic phase meter for test medium phase map generation. Here we have used frequency sweep for horizontal beam scanning and thus test medium scanning is controlled electronically without using any mechanical motion. Vertical scanning can be done in two ways. In one design, because a vertical line scans the test medium in the x-direction via the use of the Bragg cell, the output at the photoreceiver port is also a vertical line. Therefore, mechanical motion of the detector in the vertical direction can be used for vertical scanning. In the second method using parallel electronic processing, a multiple element linear high speed detector array is positioned along the vertical direction at the photoreceiver plane, thus eliminating the need for any mechanical motion.

3.4.1 Experimental Demonstration

In the experiment, when no test material is inserted, the phase difference between the two detected signals is always zero over the whole frequency range of the AOD. This important attribute is due to the common optical and RF paths in the instrument. First a 6 μm thick parallel-rub Nematic Liquid Crystal (NLC) cell is used to test the instrument. The AOD is driven at a frequency of 70 MHz. The NLC cell is placed with its nematic director along the linear s or vertical polarization of the scanning optical beam. Any amount of optical phase shift between 0 and 3.3158π for this particular NLC cell, which corresponds to an optical path length difference of 280nm, can be introduced by varying the amplitude of the 1 KHz square wave voltage drive signal applied to the cell.
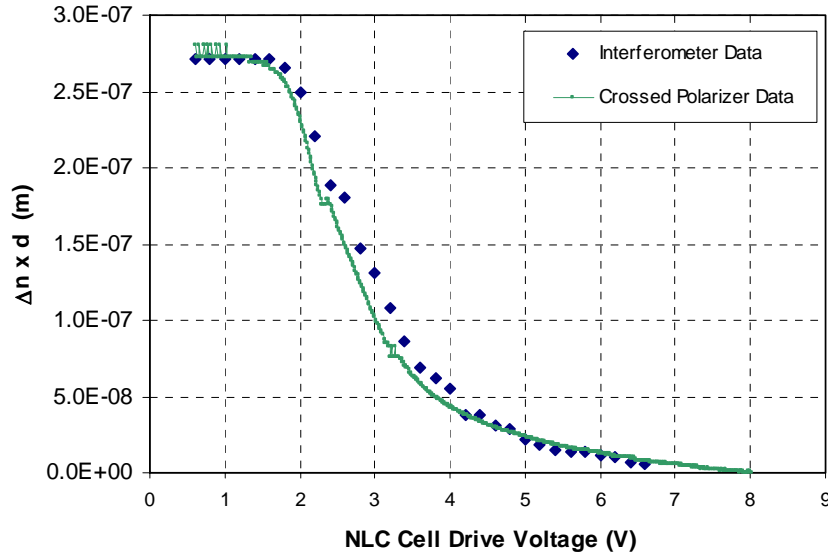
Figure 3.4.2: Measured data for the optical path length difference produced by a parallel-rub NLC cell when its drive voltage is varied. Δn is the birefringence and d is the cell thickness.

Figure 3.4.2 shows the optical path length difference $\Delta n \times d$ as the NLC cell voltage is changed from 1.6V to 6.5 V where Δn is the birefringence as a function of voltage and d is the cell thickness. To verify the results, the phase retardation of the NLC was measured as a function of applied voltage by measuring the transmitted intensity of the NLC cell when placed between two cross-polarizers with the director of the NLC cell at 45° with respect to the polarizer axes.[19] The data is plotted on the same figure and is in good agreement with the results obtained by the interferometer measurements. Note that the measurements of the thicknesses are measured to a value of about 3.315π which corresponds to $(3.315/2) \times \lambda/(2n) = 272.22$ nm. However, by the use of an electronic phase meter capable of measuring multiple 2π cycles, a wider range of thickness values can be measured.

102

(a)   (b)

(c)   (d)
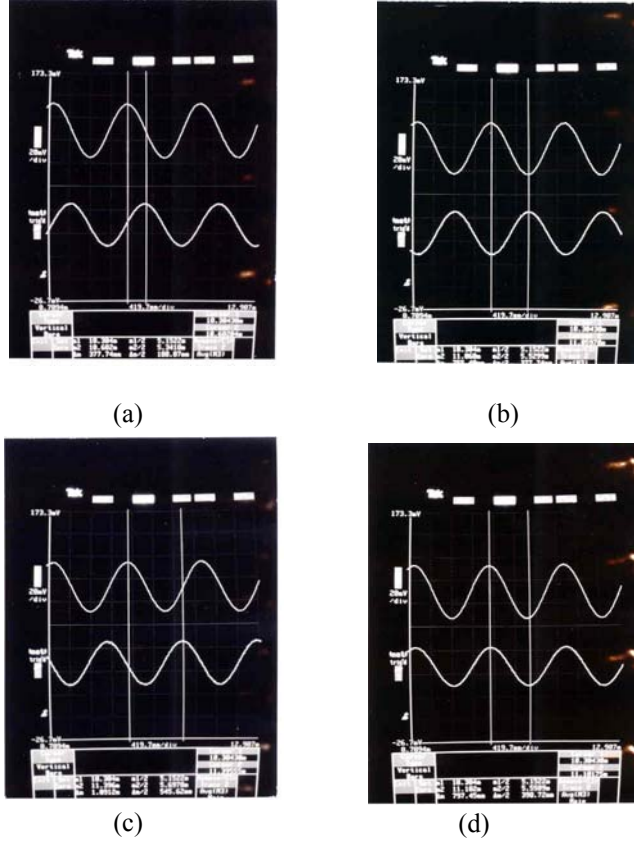
Figure 3.4.3: Oscilloscope traces of the output from the photoreceivers when the test material, i.e., an NLC cell is inserted in the scan beam with 70 MHz drive signal and when the voltage amplitude level corresponds to (a) 90^0 optical phase shift (b) 180^0 optical phase shift (c) 270^0 optical phase shift and d) 360^0 optical phase shift.

Figure 3.4.3 shows the corresponding oscilloscope traces of the outputs from the photodetectors for Bragg cell frequency of 70 MHz with various amounts of phase shift introduced through the NLC cell by changing the voltage level. Next a glass plate with refractive index of 1.5 is inserted as a test material and a frequency sweep signal starting from 52MHz to 90MHz is used to scan the plate for thickness measurements. The phase difference is measured using a RF lock-in amplifier SR 844 from Stanford Research Systems with an instrument resolution of 0.02^o. However, in the experiment the fluctuations of the phase readings obtained from the lock-in amplifier amounts to $\pm0.05^o$ which corresponds to an instrument

working resolution of 0.1° that in turn sets the thickness measurement resolution of 1.42^{0}A for the interferometer. The test plate is scanned to get the relative thickness as compared to the 70 MHz reference position on the plate. This data is shown in Figure 3.4.4. As a laser of 514.5 nm wavelength is used in this experiment, thickness values upto $514.5/2 = 257.5$ nm can be measured using this setup. The scanning distance covered by the laser beam is given by $\Delta x = \{ \theta_{stop} - \theta_{start} \}$ FL$_2$ where θ is given by θ (mrad) = [λ (μm) $\times f$ (MHz)] / V$_a$ (mm/ μs). Here V$_a$ is the acoustic velocity of RF wave in the AOD. In this experiment using flint glass AOD with f_{start} = 52MHz and f_{stop} = 90 MHz, f $_2$ = 15 cm, and V$_a$ = 3.846 mm/ μs, a total scan distance of about 540 μm is achieved in the x-direction. This distance can be increased by increasing the frequency sweep range for a wider bandwidth AOD. This experiment was performed to show the scanning capabilities of our proposed interferometer. The basic accuracy demonstration was done with the NLC cell experiment.
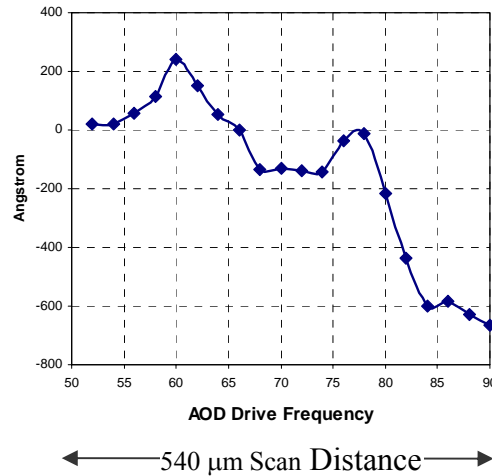
Figure 3.4.4: Experimental data of relative thickness of the test plate inserted in the interferometer relative to 70 MHz center frequency position with scanning performed by a frequency sweep signal of 52 MHz to 90 MHz.

3.5 Precision Polarization Multiplexed Heterodyne Interferometer Design

Figure 3.5.1 shows how using polarization multiplexing, an optimized interferometer design is realized with the desired common phase noise leading to greatly improved detection efficiency with a minimal of optical components. First a combination of a linear polarizer P and a laser
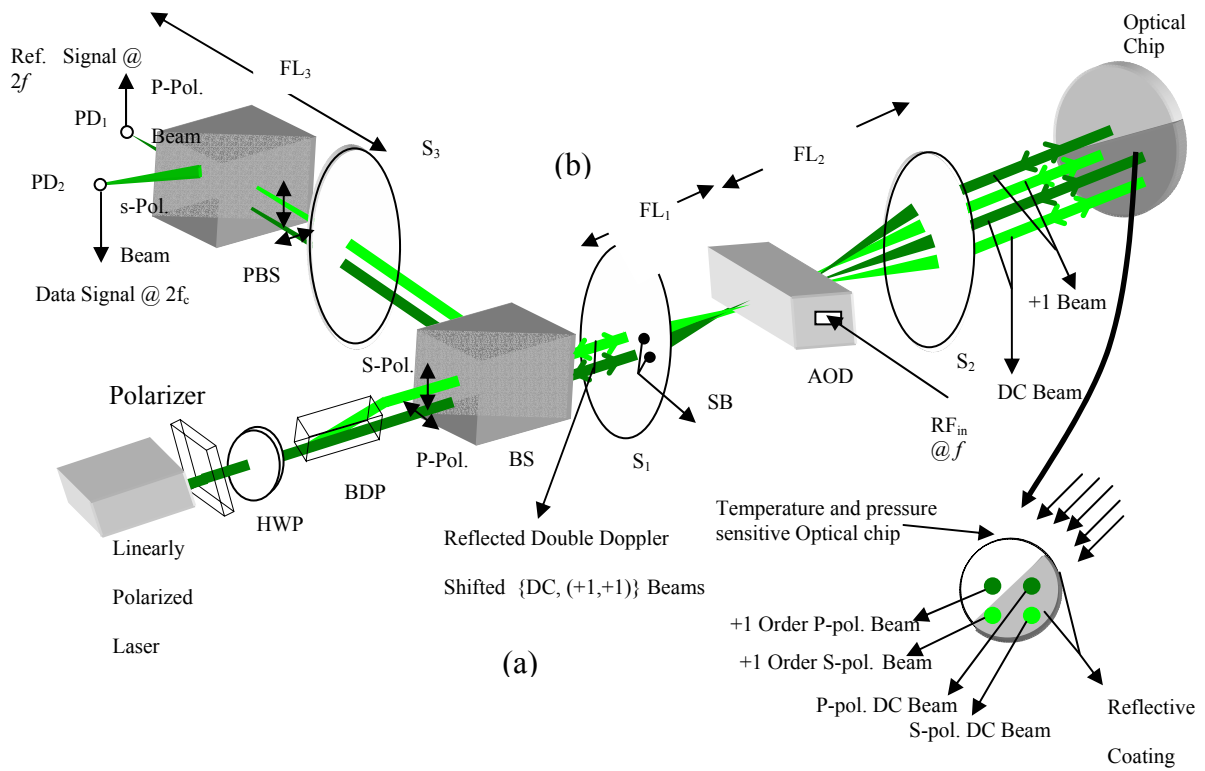
Figure 3.5.1: Schematic diagram of the proposed polarization multiplexed heterodyne scanning interferometer including the novel optical sensor chip for internally referenced phase measurements for high stability. HWP: Half wave plate, BDP: Beam displacement prism, P-Pol: Horizontal polarization, S-Pol. Vertical Polarization, BS: Beam splitter, S: Spherical lens, SB: Spatial block, AOD: Acousto-optic Device, PD: Photodetector.

produces a pure linearly polarized beam. Next a half wave plate (HWP) is used that can change the linear polarization orientation depending upon the orientation of the optic axis of the HWP

with respect to the input beam linear polarization. A beam displacement prism (BDP) then divides the input beam into horizontally (P) and vertically (S) polarized beams. The BDP is oriented in such a way that the two beams are displaced vertically from each other. One of the beams acts as a reference beam while the other beam acts as a signal beam. A desired vertical inter-beam displacement can be obtained by proper selection of the length of the BDP crystal. The rotation control of the HWP makes a powerful mechanism to control the relative power in the signal and reference beams. Specifically, if a linear polarizer P with its axis along the horizontal direction is selected, and the optic axis of the HWP is at θ with respect to the polarizer axis, the resultant beam is polarized at 2θ with respect to the horizontal direction. This beam then passes through the BDP which produces reference and signal beams with normalized powers of $\cos^2(2\theta)$ and $\sin^2(2\theta)$, respectively. Hence, any optimum ratio of optical powers between the two beams can be obtained by properly selecting the orientation of the HWP. This in turn provides a power control feature for the reference and signal coded beam in the proposed sensor. The two S and P polarized optical beams obtained after the BDP are focused into the AOD or Bragg cell by a spherical lens S_1 of focal length FL_1 placed at a distance of FL_1 from the Bragg cell at the respective Bragg angle. The AOD is driven by an RF of f frequency.

The light output from the AOD consists of two undiffracted DC P and S polarized beams of normalized powers of $(1-\eta)$ and two +1 order positive Doppler shifted diffracted P and S polarized beams of normalized power η, where η is the diffraction efficiency of the AOD Bragg cell. These DC and +1 order beams then pass through a lens S_2 of focal length FL_2 which is placed at a distance of FL_2 from the AOD. These beams after passing through the lens become parallel to each other. Note that the four beams coming from S_2 are all parallel plane waves and hence have a small divergence. Hence, the sensor chip can be placed at a convenient distance for

the setup while maintaining the same pass return path for the beams and hence preserving the Bragg condition in the AOD eliminating the need to place the sensor chip at the focal length.[15] Note that in the Ref. [15] design, the light output at the sensor plane as well as at the high speed photodetector plane is a vertical line that reduces the over all optical efficiency of the system. The proposed Figure 3.5.1 design achieves an optically efficient point-to-point design with a minimal number of optical components. This is because the light beams at the sensor chip are small circular beams and the beams at the high speed detectors are focused points thus creating a power efficient system.

The +1 order P-polarized beam produces a signal coded beam that passes through the active zone of the sensor chip and is reflected from the back surface with a reflectivity of R_1. On the other hand, the P-polarized DC beam and the S-polarized DC, +1 beam pair are reflected back from the in-active zone of the sensor chip with a reflectivity of R_2. Thus a variable OPL difference is introduced between the sensing beam pair and the reference beam pair that depends upon the thickness and the refractive index of the active zone of the sensor chip. The material of the sensor chip can be chosen to be sensitive to the measured sensor process variable such as temperature or pressure. Note that S-polarized beam pair (DC and +1 order) and the DC P-polarized beam are reflected from the chip front surface and hence do not pass through the sensor chip active layer. These four beams are thus reflected back into the system and are double diffracted on the return path. The +1 order beams produce a double diffracted (+1,+1) order beams that become collinear with their respective DC beams and are stationary. The other pair (+1, -1) order beam are blocked spatially. First a BS in the return path deflects the light at 90^0 and then a PBS is used to separate the P-polarized and S-polarized beam pairs. Photodetector PD_1 detects the sum of the P-polarized DC with a normalized optical field amplitude of

$\sqrt{(1-\eta)^2 R_2}$ and the double diffracted (+1,+1) order beam with a normalized amplitude of

$\eta\sqrt{R_1}$. PD$_2$ detects the sum of the S-polarized DC beam with normalized amplitude of

$\sqrt{(1-\eta)^2 R_2}$ and the double diffracted (+1,+1) order beam with a normalized amplitude of

$\eta\sqrt{R_2}$. Both PD$_1$ and PD$_2$ produce heterodyne detected signals at 2f. An efficient heterodyne

detection process is implemented when the amplitudes of the respective signals are equal. This

condition is achieved in the proposed design by controlling the orientation of the BDP and the

HWP in Figure 3.5.1, along with power control of the RF signal applied to the Bragg cell. The

signal from PD$_1$ acts as a reference phase signal while the signal from PD$_2$ is the data signal

coded with the OPL variation information. Both the reference phase and the test medium phase

2f frequency signals are fed to an electronic phase meter for sensor parameter measurements.

Most importantly, the phase between the two signals remains constant including over the wide

frequency range of operation of the AOD as the frequency is swept to implement scanning. This

phase meter output signal phase stability is due to the near common paths traveled by the two

beams pairs in the entire interferometer, hence undergoing the same phase noise conditions due

to the same environmental perturbations within the beam paths. As the sensing parameter

changes, the OPL in the sensor chip changes and produces a phase difference between the RF

signals feeding the phase meter. This phase difference $\Delta\phi$ can directly be calibrated in terms of

the sensing parameter, thus realizing a high precision OPL sensor.

In general, the reflectivity of the active zone R_1 of the sensing chip can be different from

the reflectivity R_2 of the in-active zone of the sensor chip. This will create reference and signal

beams of unequal magnitudes and also an un-optimal heterodyne signal which hinders optimal

phase detection at the phase meter that requires two equal power signals for optimal noise rejection. As mentioned earlier, the orientation of the HWP and the BDP provides the control of optical power in the reference and signal beams. Another important aspect is the different reflectivities of the individual pixels that will create an un-optimal heterodyne detected RF signals at frequency $2f$. This requires power control within the DC and the +1 order beams. This control is provided by the adjusted power of the RF signal applied to the AOD that changes the diffraction efficiency of the AOD in the proposed design. Thus an optimal power split ratio between the DC and the +1 sensing beam can be obtained for the sensing pixel. Hence, the power split control in the reference and signal beam by the orientation of the HWP and the BDP along with the power control of the +1 order beams realizes a sensing system for widely different sensing materials and sensor chips.

3.5.1 Experimental Demonstration

Vertically or s-polarized light from a 532 nm 15 mW Nd:YAG laser passes through a HWP oriented at 22.5^0 to the vertical axis. A BDP is oriented at 45^0 to the horizontal direction producing two vertically displaced equal power beams with a separation of 2 mm. The upper beam is s-polarized while the lower beam is p-polarized. These beams pass through the BS and are focused into an AOD at the respective Bragg angle using a $FL_1 = 10$ cm biconvex lens S_1. The AOD used is a flint glass Bragg cell with a center frequency of $f = 70$ MHz and a bandwidth of 40MHz. The active AOD aperture is 39 mm $\times$ 2mm with an access time of 10 μs. The AOD is driven by a frequency synthesizer coupled with a power amplifier with a 40 dB gain.

To demonstrate the validity of the proposed architecture, a 6 μm thick parallel-rub Nematic Liquid Crystal (NLC) chip is used to test the instrument. The chip has four identical LC pixels which can be controlled independently by varying a voltage signal to the respective pixel electrodes. The NLC chip is placed with its nematic director along the linear p-polarization of the
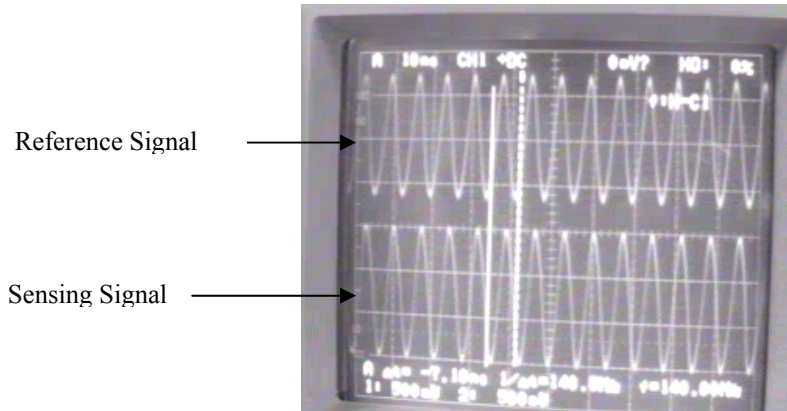
Figure 3.5.2: Oscilloscope traces of the 140MHz output from the photoreceivers when sensor test material, i.e., an NLC chip is inserted in the system. The AOD drive is 70 MHz. The upper trace is the reference phase data obtained from PD_1 while the lower trace is the signal phase obtained from PD_2.
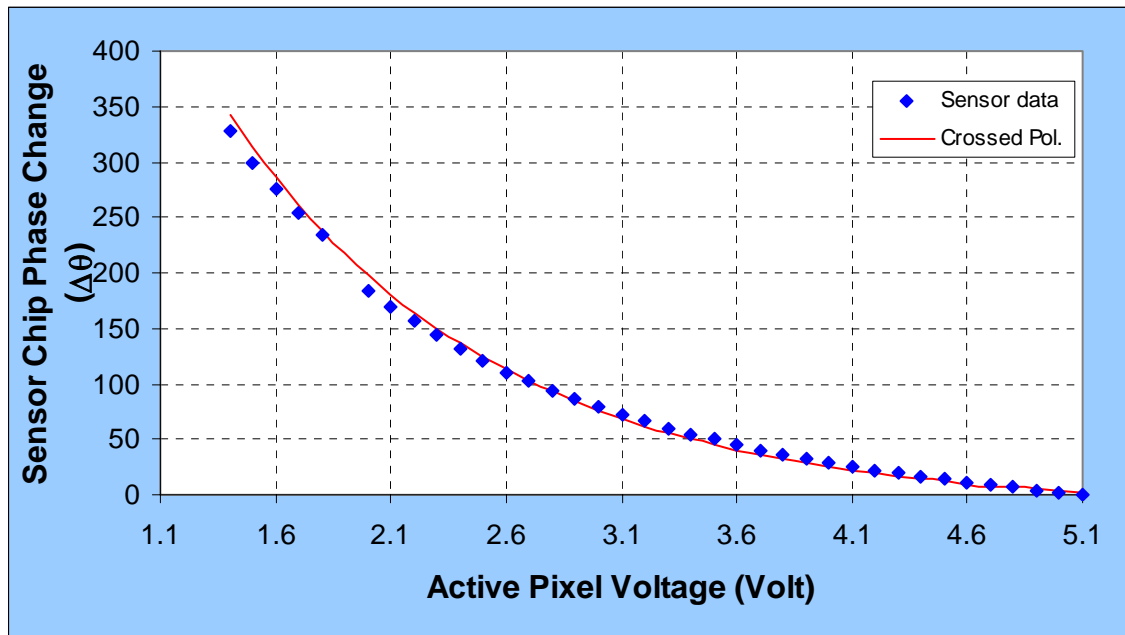
Figure 3.5.3: Experimental data of relative phase shift introduced in the NLC chip in the interferometer by varying the amplitude of the voltage drive signal to the sensing LC pixel.

scanning optical beam. Any amount of optical phase shift between 0 and 330^0 for this particular NLC chip, which corresponds to an optical path length difference of 243.833 nm, can be introduced by varying the amplitude of the 1 KHz square wave voltage drive signal applied to the one active pixel in the NLC chip that corresponds to the +1 order P-polarized beam. Note that the other three LC pixels are not driven by the voltage signal and thus do not introduce any OPL variation. The OPL variation is only introduced in the +1 order p-polarized beam that creates a signal coded beam. Figure 3.5.2 shows a oscilloscope trace of the detected $2f$=140 MHz sensing and reference signals that feed the phase meter. The upper signal is the reference signal while the lower signal is the sensor phase coded signal. The phase angle $\Delta\theta = \theta_s\text{-}\theta_r$ is a function of the LC chip voltage and the LC chip thickness d. This phase difference $\Delta\theta$ is measured using a RF lock-in phase meter with an instrument resolution of 0.02^o. In the experiment a $\pm0.05^0$ fluctuation in phase readings is obtained from the lock-in phase meter which corresponds to experimentally demonstrated resolution of 0.1^o. This in turn sets the OPL measurement resolution of 1.4Å for the demonstrated sensor. Figure 3.5.3 shows the LC sensor chip active pixel phase variations versus the pixel drive voltage. To verify the results, the phase retardation of the NLC chip was measured as a function of applied voltage by measuring the transmitted intensity of the chip when placed between two cross-polarizers with the NLC director of the chip at 45° with respect to the polarizer axis. The data is in good agreement with the results obtained by the interferometer measurements.

3.6 <u>Wavelength Multiplexed Heterodyne Interferometer Design</u>

The proposed and demonstrated architecture of the wavelength multiplexed heterodyne interferometer is shown in Figure 3.6.1. Here two laser sources of wavelengths λ_1 (reference beam) and λ_2 (signal beam) with orthogonal polarizations are used. A PBS combines these two beams and makes them in-line. Next, these beams pass through a BS and an AOD that is fed with an RF of f. Note that here a broadband operation AOD ensures proper diffraction efficiency across the two wavelengths. The +1 order beams are spatially separated on account of different Bragg angles corresponding to the two different wavelengths. These beams pass through a cylindrical lens and become parallel to each other. The two DC beams and the +1 order reference beam are reflected from a highly flat reference mirror while the +1 order signal beam at λ_2 is reflected from the test surface. These retroreflected beams traverse back and are double diffracted by the AOD. The undiffracted DC beams and the two double diffracted (+1,+1) order beams are stationary while the two (+1,-1) and undiffracted +1 order beams are spatially blocked. The two in-line { DC, (+1,+1)}beam pairs are deflected first through the BS and then are separated from each other by using a PBS. The reference beam at wavelength λ_1 is heterodyne detected through high speed photodetector PD_1 while the signal beam is detected by PD_2. Therefore two signals at a RF frequency of $2f$ are obtained. These two signals are then fed into a lock-in amplifier and the relative RF phase between the two beams is measured. This relative phase shift changes as optical beam scanning in one dimension over the test sample is done by changing the RF drive frequency of the AOD. As the two DC beams and the +1 order reference beam are reflected from a flat surface, these beams do not introduce any additional RF

phase shift. However, the +1 order signal beam is reflected from a different point on the surface of the test sample leading to a possible change in relative RF phase shift in the lock-in amplifier. Hence, this measured RF phase information provides metrology data for the surface of the test sample. In addition, the RF amplitude data provides a measurement of the light spatial attenuation characteristics in the sample. Using the full RF frequency range of AOD, a one dimensional surface profile map of the test sample can be generated. For a complete two dimensional map, either the sample or the sample engaging signal beam can be translated in the orthogonal linear dimension.

Figure 3.6.1: Proposed wavelength multiplexed acousto-optic scanning heterodyne interferometer with RF self-referencing capability. BS: Beam splitter; PBS: Polarization Beam Splitter; AOD: Acousto-optic Deflector; PD: Photodetector.

3.6.1 Experimental Demonstration

As a first demonstration of the proposed internally referenced interferometer concept using wavelength multiplexing, a high flatness mirror is used as a reference surface while a poor flatness quality mirror is used as a test plate.
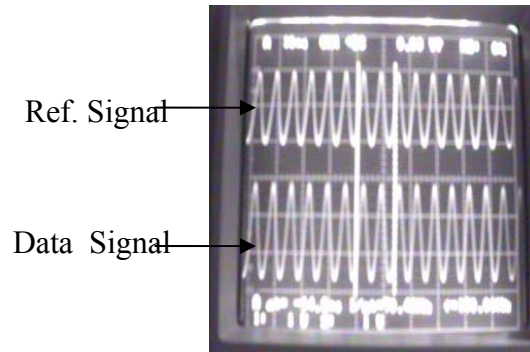
Figure 3.6.2: Oscilloscope traces of the two RF signals @ 70 MHz. The upper signal is the reference signal obtained via heterodyne detection of DC and (+1,+1) order optical beam at wavelength λ_1. The lower signal is obtained via heterodyne detection of DC and (+1,+1) order optical beam at wavelength λ_2.
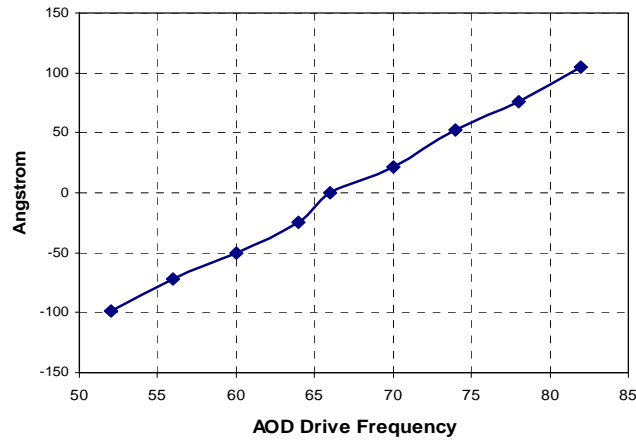
Figure 3.6.3: Relative thickness data of the test plate obtained through scanning the AOD drive frequency from 52 MHz to 85 MHz.

114

An argon ion laser with a wavelength of 514.5 nm is used as a signal wavelength while a 632 nm HeNe laser is used as the reference wavelength for internal RF reference signal generation. An AOD with a center frequency of 70 MHz and bandwidth of 40 MHz is used for the experiment. Figure 3.6.2 shows the oscilloscope traces of the two detected RF signals. The phase difference is measured using a RF lock-in amplifier SR 844 from Stanford Research Systems with an instrument resolution of 0.02^o. However, in the experiment the fluctuations of the phase readings obtained from the lock-in amplifier amounts to $\pm0.05^o$ which corresponds to an instrument working resolution of 0.1^o that in turn sets the thickness measurement resolution to 1.4 Å for the demonstrated interferometer. The test plate is scanned to get the relative thickness as compared to the 70 MHz reference position on the plate (see Figure 3.6.3). As a laser of 514.5 nm wavelength is used in this experiment, thickness values up-to 514.5/2 = 257.5 nm can be measured using this interferometer.

3.7 Fiber Coupled In-line Heterodyne Optical Interferometer

Figure 3.7.1 shows the proposed fiber-coupled scanning heterodyne optical interferometer system with a remoted compact front-end and a minimally invasive sensor chip. An IR laser is single mode fiber (SMF)-connected to a fiber-lens (F) through a three port circulator C. The collimated light exiting F is Bragg-matched to the AOD center frequency. The light output from the AOD consists of an undiffracted DC beam and a +1 order positive Doppler shifted diffracted beam. These DC and +1 order beams then pass through a lens S_1 of focal length FL_1 which is placed at a distance of FL_1 from the AOD. The DC and +1 order beam pair after passing through the lens S_1 become parallel to each other. The optical sensor chip is placed

at a distance FL_1 from the lens S_1. The fixed DC beam acts as a reference beam and is reflected from the reference in-active zone of the sensor chip. On the other hand, the +1 order beam acts as the scanning beam that is reflected from the selected active sensing zone of the sensor chip. Note that the free-space architecture of the proposed system takes advantage of the ultra-low loss SMF-SMF self imaging coupling technique leading to a low loss interferometer design despite using fiber-optics.[20] While enabling high speed non-mechanical scanning on the sensor chip, it is critical to keep the processed output beams fixed to launch light back into the SMF. In Figure 3.7.1 this task is accomplished by using double Bragg cell diffraction within the single Bragg cell, where the output +1 diffracted beam scans the sensor chip with the changing AOD drive frequency, yet the double diffracted (+1,+1) scan beam is in-line with the DC or original input beam to provide precise coupling back into the SMF lens entrance face. Note that both the DC and the diffracted beam pass via the same optical components in the free-space front-end optics and the remoting SMF. Thus any environmental effects such as vibrations affect both beams and are cancelled out on heterodyne detection. Note that the AOD is set to produce 50% diffraction efficiency to ensure equal beam intensities at the sensing chip. When the DC and +1 beams are reflected back, these beams are again Bragg matched for 50% diffraction efficiency. After passing through the AOD twice, the two beams, i.e., (DC, +1,+1) and (+1,-1) orders both have equal intensities and hence introduce a 3 dB optical loss in the front-end of the system. The proposed system configuration provides a useful control mechanism for the output beam intensities at the sensor chip. Specifically, the diffraction efficiency of the AOD can be varied by changing the RF power of the AOD drive signal. This feature can be used to cancel out the differences in the reflectivities of the inactive and the active zones of the optical sensor chip to produce equal power DC and double diffracted beams for efficient heterodyne detection.

116
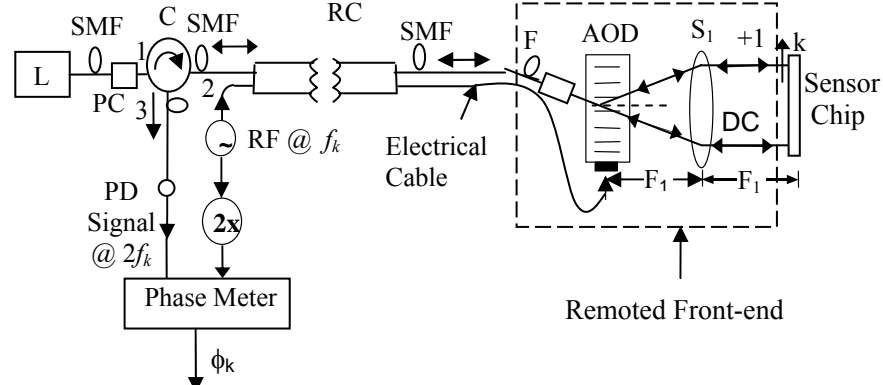
Figure 3.7.1: Fiber coupled scanning heterodyne optical interferometric sensing architecture showing fiber-remoted sensing head and the related RF electronics. L: Laser, C: Circulator, SMF: Single Mode Fiber, F: Fiber Lens, S_1: Spherical Lens, FL_1: Focal Length of S_1, AOD: Acousto-optic Device, PD: High Speed Photo-detector, f_k: RF frequency for k^{th} scan position, RC: Remoting Cable, PC: Polarization Controller.

The SMF coupled returning optical signal pair then goes from port 2 to the port 3 of the circulator. At port 3, a high speed photo-detector (PD) is connected where heterodyne detection takes place and a signal at $2f_k$ is generated where f_k is the AOD drive frequency for the kth scan position of the sensor chip.

As shown in Figure 3.7.1, the use of the remoting cable (RC) allows the possibility of placing the sensor front-end at some distance from the detection unit. The cable contains one SMF and one RF cable that feeds the AOD. Because both the DC and (+1,+1) optical beams from the interferometric sensor front-end travel at the same time through the same fiber, any phase noise due to environmental effects of the SMF affect both optical beams and hence gets cancelled out on heterodyne photo-detection. Hence the fiber can have any desired long or short length. On the other hand, the RF cable length and packaging must be appropriately designed to reduce introduction of RF phase noise due to cable environmental effects. For example, the AOD RF drive frequency of 100 MHz is approximately 3 m of cable length for a 2π radian phase cycle. For a low RF phase noise under 1/1000 of one full RF phase cycle, the RF cable length

117

fluctuations due to environmental effects must be kept under 3 mm. It is common practice to use microwave antenna cabling with the optimized packaging for tens of meters lengths for low noise (e.g., < 1/1000 of cycle) RF signal remoting. Hence, the proposed RC in Figure 3.8.1 can also deploy such cabling giving typical distances of up-to tens of meters between the detection and front-end sensor units.

Figure 3.7.2 shows the design of the proposed sensor chip that interfaces to the proposed Figure 3.7.1 front-end interconnection. The signal and the reference beams pass through the different cells of the sensor chip. Specifically, the fixed reference beam strikes the inactive sensor zone on the chip while the scanned signal beam can access any one of N sensing zones on the chip. The phase difference between the retro-reflecting fixed reference beam and the signal scan beam is given by:

$$\phi_k = \frac{4\pi}{\lambda}(OPL_{sk} - OPL_{ref}) = \frac{4\pi}{\lambda}[n_{sk} - n_{ref}]t. \qquad (3.8.1)$$
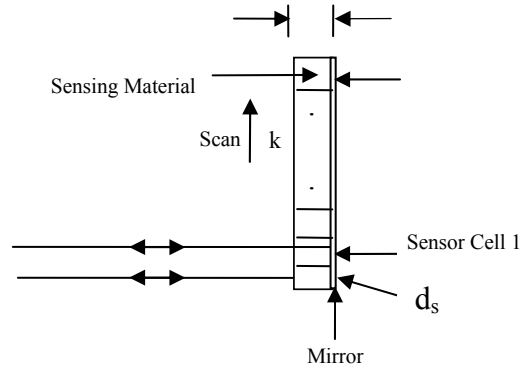
Figure 3.7.2: Proposed reflective optical sensor chip design for the cable-remoted front-end. The chip contains N active sensing zones accessed via the scanned signal beam and one in-active reference zone accessed by the fixed reference beam exiting the interferometer front-end.

Here n_{sk} is the refractive index that the kth scan position (k= 1, 2, …, N) signal beam sees

while passing through the kth active cell of the sensor chip. On the other hand, the reference beam is subjected to a fixed refractive index n_{ref} of the reference cell. The refractive index or the thickness of each active sensor cell can be custom designed with specific materials that are sensitive to external parameters like temperature, pressure, bio-molecular, and gas concentrations. On the other hand, the reference cell is designed to be insensitive to the sensing parameters under observation.

The sensing parameter measurement accuracy depends upon the measured accuracies of the relative phase shift measured in the proposed interferometer. It has been shown that the phase in such an interferometer design can be measured to $\pm 0.01^0$ accuracy.[15] In the case of Eq. 3.2.7, the second factor is the thickness of the sensing zone material which governs the accuracy of the measurements. For applications where absolute values are not required, the calculations can be carried out by using $\Delta n(\Delta P) \times t(P)$ instead of $\Delta n(\Delta P)$ to give an incremental change in the parameter P. This eliminates the inaccuracies due to the thickness measurement uncertainties. The Figure 3.7.1 interferometer can then be calibrated directly in terms of the phase to measure variations in the parameter P. In a similar fashion, uncertainties due to the measurement inaccuracies of $\{n(P)-n_{ref}\}$ can be avoided by calibrating the instrument in terms of $\Delta t \times \{n(P)-n_{ref}\}$.

An important point to note about the proposed architecture is that multiple sensing parameters that are connected with the measured RF phase can be measured separately. In this case, every cell in the sensor chip can be used to measure a specific parameter depending upon the material chosen. For example, one cell material can be chosen to have a large thermo-optic coefficient (or dn/dT where T is the temperature) and a low photo-elastic coefficient (or dn/dPa where Pa is the pressure). Then this cell can be used to measure the temperature T of the

environment. At the same time, another cell material in the chip can be chosen with a low thermo-optic coefficient but with a high photo-elastic coefficient. This cell can then be used to measure changes in pressure. Thus the true-power of the proposed sensor is in addressing a large number of cells by using electronically controlled scanning for measuring multiple material specific parameters via various cells.

3.7.1 Experimental Demonstration

A proof of concept experiment of the Figure 3.7.1 system has been performed at the eye safe wavelength of 1550 nm. The laser is fiber connected to a fiber lens of 6 cm half self-imaging distance. The AOD used is a Chalcogenide glass Bragg cell with a center frequency of 100 MHz and a bandwidth of 1.25 MHz. The active AOD aperture is 20 mm × 4 mm with a 3.9 mm/ μs acoustic wave velocity. The AOD is driven at 100 MHz by an RF frequency synthesizer coupled with a power amplifier with a 40 dB gain. The desired $2f_k$ reference signal is generated using an RF frequency doubler device. A spherical lens S_1 of focal length FL_1= 10 cm is used as the Fourier transforming lens. In the experiment when a simple mirror is used as the reflector sensor chip, the RF phase difference between the RF signals produced by the high speed photodiode and the signal from the frequency doubler is constant over the whole RF frequency range of the AOD. This important attribute is due to the common optical and RF paths in the system. A polarization controller (PC) is inserted before the FL to produce s-polarized optical beams to match the vertical nematic director of an inserted test parallel-rub NLC cell. A variable OPL is introduced by varying the amplitude of the 1 KHz square wave voltage drive signal applied to the NLC cell used as a two zone sensor chip. Note that the +1 order beam is passing

through the electrically active NLC cell while the DC beam passes through the electrically in-active part of the two pixel NLC cell.

Figure 3.7.3 shows the OPL difference $\Delta n \times t$ (µm)as the NLC cell voltage is changed from 1.1 V to 5.1 V, where Δn is the NLC birefringence as a function of voltage and t is the NLC cell thickness. To verify the results, the same NLC cell is inserted between a pair of cross polarizers and the intensity is measured as the cell voltage is changed. The birefringence is measured from this intensity data and is shown as a solid line in Figure 3.8.3. This result is in good agreement with the experimental values obtained from the interferometer.

The present overall length of the sensor head is 26 cm, i.e., 6 cm half-self-imaging distance of FL plus 20 cm for the 2FL geometry of the S_1 spherical lens. Note that this front-end size can be greatly reduced by using a smaller focal length spherical lens and a FL with a shorter self-imaging distance leading to a compact and flexible sensor front-end. The total optical loss of the demonstrated interferometric system is 4.69 dB calculated as 1.29 dB circulator loss + 0.2 dB free-space SMF coupling loss + 3 dB system loss due to AOD Bragg diffraction + 0.2 dB Fresnel loss of lens S_1, NLC cell, mirror, AOD, and mirror. In effect, this total system loss can be further reduced by using lower loss optimized components with anti-reflection coatings for the wavelength of operation. At present, the AOD used in the experiment has a limited 3 dB bandwidth of 1.25 MHz that is not optimized for high diffraction efficiency scanning of the optical beam. However, by using AODs designed as deflectors and not modulators, one can generate wide linear range scanning, such as demonstrated in earlier work.[15]
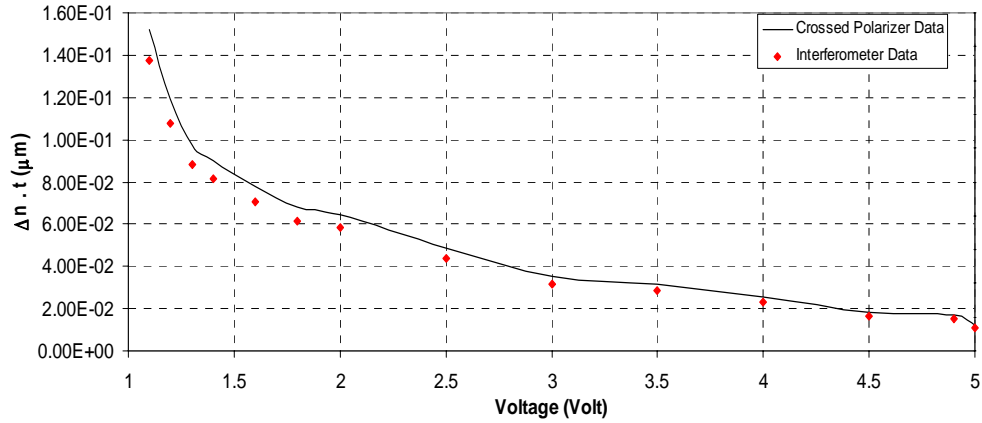
Figure 3.7.3: Interferometer sensed data (plotted as diamonds) showing the OPL difference $\Delta n \times t$ (in μm) produced by varying the drive voltage in volts of a parallel-rub NLC cell used as a two zone sensor chip. Δn is the voltage controlled NLC birefringence and t is the fixed NLC cell thickness. The solid line data is the OPL difference of the NLC cell measured using the standard crossed polarizer method.
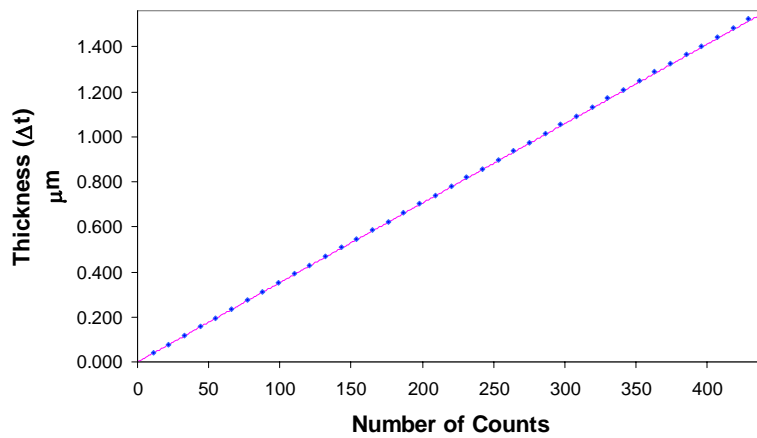
Figure 3.7.4: Interferometer sensed data (plotted as diamonds) showing the OPL difference Δt (in μm) produced by varying the number of counts of the drive signal of the precision motorized translational stage. The solid line data is the calibrated data from the specifications of the motorized stage.[22]

The Figure 3.7.3 results have shown how refractive index changes can be measured with

the proposed instrument for a sensing zone where the physical path length is fixed such as for the

NLC cell. To perform an experiment where the instrument measures the sensing zone physical

path length changes given the path refractive index stays fixed, the NLC cell is replaced by a

fixed mirror acting as a reference cell and a precision positioned moving mirror acting as a sensing cell. In this case, the motion of the mirror along the optical axis simulates a sensing zone with changing path length and fixed refractive index (e,g, index of air). Figure 3.8.4 shows the measured experimental results indicating the sensing zone thickness changes with the fixed sensing zone refractive index. These results indeed match the calibrated solid curve data.[21]

In the proposed interferometer, polarization plays a role when the sensor chip requires probing by polarized light such as in the conducted experiment using liquid crystals. If the sensor chip is polarization in-sensitive, no particular polarization control in the system is required as all other components in the system (i.e., AOD, S_1, and F) are of the polarization-independent type. This point has been experimentally verified in the case of the Figure 3.7.4 experiment where the PC was used to vary the polarization state of the optical beam and no change in the output of the photodetector was observed. Hence if the SMF undergoes environmental effects that alter the polarization state of the fiber lens output light, a polarization independent sensor chip is preferred. Otherwise, a polarizer can be added between the F and AOD to deliver the correct polarization. In addition, a PC must be used at the laser end of the system to ensure that sufficient and stable optical power is delivered to the remoted front-end during the sensor operation time.

<u>Conclusions</u>

In conclusion, successfully implemented is a compact mode reflective heterodyne scanning optical interferometer that for example can be used to measure optical path length changes up to an angstrom level. The proposed reflective design uses an in-line RF and optical design, in addition to using few optical components in the non-common path scanning arm. The proposed instrument has the capability to measure path length changes on the atomic scale. In addition, the high speed scanning capability of the system can allow fast sensing measurements produced by the various spatially separated sensing zones on the proposed array-type sensor chip. Precise analog control of the Bragg cell drive frequency and RF power allows agile optimization of the heterodyne detected output signal-to-noise ratio.

Various design schemes to implement the proposed scanning heterodyne interferometers are presented and experimentally verified. Specifically, space multiplexed, polarization multiplexed, and wavelength multiplexed designs are presented. Successfully implemented is a fiber-coupled reflective heterodyne scanning optical interferometer that can be used for optical sensor applications at an eye safe wavelength. The demonstrated architecture is highly stable and robust to environmental effects as the reference and signal beams travel a near common optical path. The use of a fiber- remoted optical sensing front-end interfaced via free-space laser beams to an optical sensor chip provides a minimally invasive and versatile measurement technique for in-situ sensing measurements.

Proof-of-concept experiments include measurement of optical path length measurements due to thickness change and refractive index change. This design has inturn led to an interferometer demonstration with exceptionally low phase noise and a $1.42^{o}A$ measurement

resolution. It is expected that the demonstrated instrument can be a useful tool for biomedical applications involving molecular and cellular mapping, optical sensing applications, and refractive index and thickness measurement for optical metrological applications.

References

1. P. Hariharan, *Handbook of Optics*, 2nd ed. Edited by M. Bass (McGraw-Hill, New York, 1995).
2. P. K. Rastogi, Springer Series in Optical Sciences, Vol. **68**, (Springer, New York, 1994).
3. J. Schwider, D. R. Herriot, J. E. Gallagher, D. P. Rosenfeld, A. D. White, and D. J. Brangaccio, "Digital Wavefront Measuring Interferometer for Testing Optical Surfaces and Lenses," *App. Opt.*, Vol. 13, pp. 2693-2703 (1974).
4. R. Dandliker, Progress in Optics, Vol. 17, Edited by E. Wolf (North-Holland Publishing Company, New York, 1980).
5. S. Kim, I. Chang, D. Kim, T. Kim, and S. Yoo, "Very Large Scale Phase Measuring Interferometry for Profile Measurement of Aspheric Surfaces with Nanometer Accuracy," in The Pacific Rim Conference on Lasers and Electro-Optics, (IEEE, New York, 1999), pp. 70 -71.
6. J. E. Greaber, "Optical scanning interferometer for dynamic imaging of high-frequency surface motion," in Ultrasonics Symposium, 2000 (IEEE, New York, 2000), pp. 733 -736.
7. Y. Watanable and I. Yamaguchi, "Digital Hilbert transform for separation measurement of thickness and refractive indices of layered objects by use of a wavelength-scanning heterodyne interference confocal microscopes," *App. Opt.*, Vol. **41**, pp. 4497-4502 (2002).
8. T. Fukano and I. Yamaguchi, "Separation of measurement of the refractive index and the geometrical thickness by use of a wavelength-scanning interferometer with a confocal microscope," *App. Opt.*, Vol. **38**, pp. 4065-4073 (1999).
9. K. Creath, "Temporal Phase measurement Methods," in *Interferogram Analysis: Digital Fringe Pattern Measurement Techniques,* ed. D. W. Robinson and G. T. Reid, (Institute of Physics Publishing Ltd. , Bristol, England, 1993).
10. T. Suzuki, T. Maki, X. Zhao, and O. Sasaki, "Disturbance-free high-speed sinusoidal phase-modulating laser diode interferometer," *Appl. Opt.*, Vol. **41**, pp. 1949-1953, (2002).
11. K. Hibino, B. F. Oreb, P. S. Fairman, and J. Burke, "Simultaneous measurement of surface shape and variation in optical thickness of a transparent parallel plate in wavelength-scanning Fizeau interferometer," *Appl. Opt.*, Vol. **43**, pp. 1241-1249, (2004).
12. C. Chou, J. Shyu, Y. Huang, and C. Yuan, "Common-path optical heterodyne profilometer: a configuration" *Appl. Opt.*, Vol. **37**, pp. 4137-4142 (1998).
13. D. Lin, Z. Liu, R. Zhang, J. Yan, C. Yin, and Y. Xu, "Step-height measurement by means of a dual-frequency interferometric confocal microscope, " *Appl. Opt.*, Vol. **43**, pp. 1472-1479, (2004).
14. N. A. Riza, "Scanning heterodyne optical interferometer", *Rev. Sci. Instrum.*, Vol. **67**, pp. 2466-2476, (1997).
15. N. A. Riza and M. A. Arain, "Angstrom-Range Optical Path-Length Measurement with a High-Speed Scanning Heterodyne Optical Interferometer", *Appl. Opt.*, Vol. **42**, pp. 2341-2345, (2003).
16. Muzammil A. Arain and Nabeel A. Riza , "Precision Polarization Multiplexed Heterodyne Acousto-optic Interferometric Sensor," *Opt. Eng.*, Vol. **44** (5), (2005).

17. Muzammil A. Arain and Nabeel A. Riza, "Fiber Coupled In-line Heterodyne Optical Interferometer for Minimally Invasive Sensing," accepted for publication in Journal of Lightwave Technology, IEEE/OSA.

18. N. A. Riza and M. A. Arain, "Angstrom Sensitivity Polarization Multiplexed Heterodyne Acousto-optic Interferometric Sensor," in proceedings of IEEE Sensors 2004 October 24-27, Vienna, Austria, (Institute of Electrical and Electronic Engineers, New York, 2004).

19. I. C. Khoo and S. T. Wu, *Optics and Nonlinear Optics of Liquid Crystals*, Volume 1, (World Scientific, New Jersey, 1993).

20. M. van Buren and N. A. Riza, "Foundations for Low-Loss Fiber Gradient-Index Lens Pair Coupling with the Self-Imaging Mechanism," *Appl. Opt.,* Vol. **42**, pp. 550-565, (2003).

21. MP 42 E User Manual, M-126 Series Linear Positioning Stages, PI Inc., www.pi.ws.

CHAPTER FOUR: FREE-SPACE OPTICAL INTEFEROMETRIC SENSOR

4.1 Introduction

There are numerous vital sensing scenarios in commercial and defense sectors where the environment is extremely hazardous. Specifically, the hazards can be for instance due to extreme temperatures, extreme pressures, highly corrosive chemical content (liquids, gases, particulates), nuclear radiation, biological agents, and high Gravitational (G) forces. Realizing a sensor for such hazardous environments remains to be a tremendous engineering challenge. One specific application is fossil fuel fired power plants where temperatures in combustors and turbines typically have temperatures and pressures exceeding 1000 °C and 50 Atmosphere (atm). Future clean design zero emission power systems are expected to operate at even high temperatures and pressures, e.g., > 2000 °C and > 400 atm.[1] In addition, coal and gas fired power systems produce chemically hazardous environments with chemical constituents and mixtures containing for example carbon monoxide, carbon dioxide, nitrogen, oxygen, sulphur, sodium, and sulphuric acid. Over the years, engineers have worked very hard in developing electrical high temperature sensors (e.g., thermo-couples using platinum and rhodium), but these have shown limited life-times due to the wear and tear and corrosion suffered in power plants.[2] Electrical/electronic sensors have suffered from a number of draw-backs and complications that include (i) melting of the solder joint between the sensor device and the bonding wire, (ii) requirement of high temperature insulation for the electrical wires connecting the device to the electrical signal processing unit, and (iii) inconvenience in mounting or embedding the device in rotating

128

components such as turbine blades. Other limitations that are inherent to the use of thermocouples are cold junction compensation, linearization issues, long term stability of the thermal contacts, and corrosion of the expensive metallic contacts.[3]

Researchers have turned to optics for providing a robust high temperature sensing solution in these hazardous environments. The focus of these researchers has been mainly directed in two themes. The first theme involves using the optical fiber as the light delivery and reception mechanism and the temperature sensing mechanism. Specifically, a Fiber Bragg Grating (FBG) present within the core of the single mode fiber (SMF) acts as a temperature sensor. Here, a broadband light source is fed to the sensor and the spectral shift of the FBG reflected light is used to determine the temperature value. Today, commercial FBG sensors are written using Ultra-Violet (UV) exposure in silica fibers. Such FBG sensors are typically limited to under 600 °C because of the instability of the FBG structure at higher temperatures.[4] Recent studies using FBGs in silica fibers has shown promise up-to 1000°C.[5,6] To practically reach the higher temperatures (e.g., 1600°C) for fossil fuel applications, single crystal Sapphire fiber has been used for Fabry-Perot cavity and FBG formation.[7-9] The single crystal Sapphire fiber FBG has a very large diameter (e.g., 150 μm) that introduces multi-mode light propagation noise that limits sensor performance. An alternate approach proposed replaced the Sapphire fiber front-end sensing element with a complex assembly of individual components that include a Sapphire bulk crystal that forms a temperature dependent birefringent Fabry-Perot cavity, a single crystal cubic zirconia light reflecting prism, a Glan-Thompson polarizer, a single crystal Sapphire assembly tube, a fiber collimation lens, a ceramic extension tube, and seven 200 μm diameter multimode optical fibers. Hence this proposed sensor front-end sensing element not only has low optical efficiency and high noise generation issues due to its multi-mode versus SMF design, the sensor

front-end is limited by the lowest high temperature performance of a given component in the assembly and not just by the Sapphire crystal and zircornia high temperature ability. Add to these issues, the polarization and component alignment sensitivity of the entire front-end sensor assembly and the Fabry-Perot cavity spectral notch/peak shape spoiling due to varying cavity material parameters.

It has long been recognized that SiC is an excellent high temperature material for fabricating electronics, optics, and optoelectronics. For example, engineers have used SiC substrates to construct gas sensors.[10] Prior works include using thin films of SiC grown on substrates such as Sapphire and Silicon to act as Fabry Perot Etalons to form high temperature fiber-optic sensors.[11-13] Although SiC thin films on high temperature substrates such as Sapphire can operate at high temperatures, the SiC and Sapphire interface have different material properties such as thermal coefficient of expansion and refractive indexes. In particular, high temperature gradients and fast temperature/pressure temporal effects can cause stress fields at the SiC thin film-Sapphire interface causing deterioration of optical properties (e.g., interface reflectivity) required to form a quality Fabry-Perot etalon needed for sensing based on SiC film refractive index change. Note that these previous works also had a limitation on the measured unambiguous sensing (e.g., temperature) range dictated only by the SiC thin film etalon design, i.e., film thickness and reflective interface refractive indices/reflectivities. Thus making a thinner SiC film would provide smaller optical path length changes due to temperature and hence increase the unambiguous temperature range. But making a thinner SiC film makes the sensor less sensitive and more fragile to pressure. In addition, temperature change is preferably estimated based on tracking optical spectrum minima shifts using precision optical spectrum analysis optics, making precise temperature estimation a challenge dependent on the precision

130

(wavelength resolution) of the optical spectrum analysis hardware. In addition, better temperature detection sensitivity is achieved using thicker films, but thicker etalon gives narrower spacing between adjacent spectral minima. Thicker films are harder to grow with uniform thicknesses and then one requires higher resolution for the optical spectrum analysis optics. Hence there exists a dilemma where a thick film is desired for better sensing resolution but it requires a better precision optical spectrum analyzer (OSA) and of course thicker thin film SiC etalons are harder to make optically flat. Finally, all to these issues the Fabry-Perot cavity spectral notch/peak shape spoiling due to varying cavity material parameters that in-turn leads to deterioration in sensing resolution.

Ideally, one would like a robust optical sensor that can be remoted, is minimally invasive, works at high temperatures (e.g., 2000^{0}C) and pressures including chemically corrosive environments, requires low cost low loss optics, has high sensing resolution over any extended wide unambiguous range, and provides easy access to many sensing points. In this section, such a sensor is proposed and demonstrated. This sensor utilizes agile optical wavelength control with single instantaneous wavelength optical path length interferometry in a naturally forming single crystal SiC weak etalon to enable extreme conditions temperature sensing. A precision targeted free-space laser beam reads sensing parameters off the remotely placed SiC sensor chip, thus producing no physical contact between the harsh environment and the light delivery and processing optics. Many low cost SiC optical chips can be distributed in the desired sensing zone where a scanning free-space laser beam rapidly engages these sensor front-end chips to produce signals for later data processing and environmental parameter recovery. Proposed for this sensor are multi-wavelength signal processing techniques that make the sensor robust to maintaining ideal front-end processing conditions, a task impractical for hazardous conditions. Next a proof-

of-concept experiment for temperature measurement up-to 1000 ^{0}C is successfully implemented and described. The paper ends with a conclusion and future directions summary.

4.2 <u>Minimally Invasive Optical Sensor Design and Operational Principles</u>

4.2.1 Proposed Sensor Optical Design

Figure 4.2.1 shows the proposed high temperature minimally invasive optical sensor. The sample front-end is composed for example of three weak Etalon Optical Sensor Chips (EOSCs) using single crystal SiC. Light from a tunable laser passes via fiber-optics such as a polarization controller (PC) and isolator (I) to exit via a fiber lens (FL$_1$) to produce a freespace beam. This light then passes via a polarizer P$_1$ (at a slight angle to the horizontal or p-polarization direction) and a polarizing beam splitter PBS$_1$ to produce a s or vertically polarized reflected beam that via mirror M$_5$ enters photodetector PD$_2$ whose output is used to access sensor efficiency. The straight linearly (or horizontally) polarized beam from PBS$_1$ passes via a quarter-wave plate QWP$_1$ (or 45^0 power Faraday rotator) and a bulk spherical lens S$_1$. The use of QWP$_1$ gives polarization insensitivity to the SiC sensing operations as circularly polarized light strikes the SiC crystal that can possess some birefringence. The lenses are used to reduce beam spreading loss. The mirrors M$_1$, M$_2$, M$_3$, and M$_4$ are 2-axis mirrors that are adjusted to select the desired EOSC and implement normal incidence alignment with the etalon chip. All mirror optics can

also be made of high temperature capability SiC foam material such as used for space telescope applications.
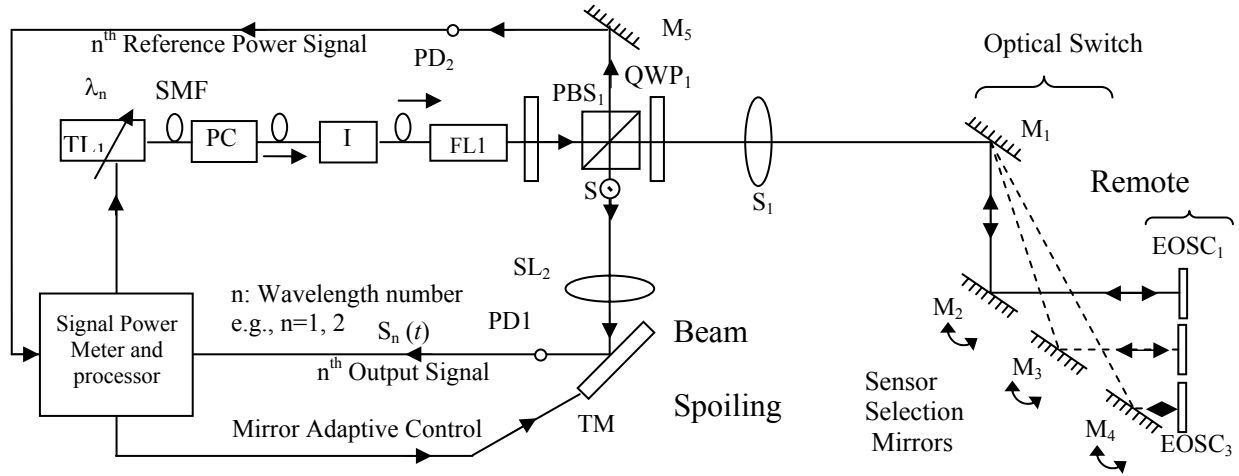
Figure 4.2.1: Proposed extreme environment minimally invasive optical sensor using single crystal SiC. PD_1/PD_2: Freespace Coupled Photo-detector; $M_1/M_2/M_3/M_4$: Chip Selection and Alignment Mirrors; M_5: Feedback Mirror; EOSCs: Etalon Optical Sensor Chips, e.g., Single Crystal Silicon Chip; PC: Polarization Controller; TL_1: Tunable Laser ; I: Fiber Optic Isolator; FL_1:Fiber Lens of self imaging type with half self imaging distance d_s where beam waist w_i is located ; P_1: Polarizer with a small angle along p-polarization direction; PBS_1:Polarization Beam Splitter; SL1/SL2: Imaging Lenses of focal lengths FL_1/FL_2; TM: Beam Spoiling Correction Adaptive Mirror; QWP_1: Quarter-wave Plate or 45^0 power Faraday Rotator; SMF: Single Mode Fiber.

Because of its high refractive index (e.g., 2.57), single crystal SiC chip acts as a natural weak etalon in air with about 20% optical reflectivities at the two air-SiC interfaces. Light reflected from the chosen etalon chip traces the path back via the mirrors and S_1 to reflect via PBS_1 as vertically polarized light towards spherical lens S_2. The returning light via S_2 then passes via the beamforming mirror TM to strike a freespace coupled photodetector PD_1. TM is a beam spoiling correction mirror such as a deformable mirror that as needed corrects wavefront distortions and keeps the returning beam aligned on PD_1 to produce the optimal sensing signal based on optical path length changes in the front-end etalon chip. Because the EOSCs can be

mounted on various platforms that may have vibrations or other beam perturbing environmental effects such as air currents, pressure gradients, thermal gradients, the returning freespace beam from the sensing zone can suffer unwanted beam motions and wavefront distortions. Hence, for proper sensor operation, the returning beam must strike the active detection zone of the free-space large area (e.g., a few millimeter diameters) point photodetector. Note that as the SiC crystal etalon optical path length changes due to change in sensing zone temperature, the etalon reflected signal power varies and can undergo several power variation cycles. To maintain proper sensor operation and calibration as explained next, the instantaneous PD_1 produced power level signal is normalized before signal processing required to compute the sensed temperature. This normalization is done in a no-moving parts electronic fashion by sweeping the laser wavelength to synthesize optical path length changes and then measure the nearest power maximum and minimum and using these max/min data for the instantaneous reading normalization, hence giving robustness to the sensor operations.

4.2.2 Proposed Sensor Theoretical Foundations

The proposed non-invasive sensor utilizes the SiC crystal Fabry-Perot cavity interference to extract sensing information. Specifically, classic expression for the reflectance from a Fabry-Perot type interference due to multiple reflections between two parallel dielectric plates with front surface power reflection of R_1 and back surface power reflectance R_2 is given by:[14]

$$R_{FP} = \frac{R_1 + R_2 + 2\sqrt{R_1 R_2}\cos\phi}{1 + R_1 R_2 + 2\sqrt{R_1 R_2}\cos\phi} \ .$$

(4.2.1)

Note that the SiC chip also acts as a natural optical window that can be placed as a sealing window separating an extreme temperature hazardous zone from a safe lower hazard zone. In this case for the single crystal SiC chip, R_1 is the reflectivity provided by the air-SiC interface facing the light beam present in the preferably friendlier zone while R_2 is the reflectivity provided by the SiC-air interface present in the hazardous extreme temperature zone. It is also possible to place the SiC chip as a mounted chip exposed to the entire extreme temperature zone with both crystal interfaces engaging the light beam equally exposed to high temperature.

An optical path length (OPL) parameter in radians for the proposed sensor is defined as:

$$\text{OPL} = \phi = \frac{4\pi n(\lambda)d}{\lambda}, \qquad (4.2.2)$$

where ϕ is the round-trip propagation phase in the SiC crystal of thickness d and refractive index n at a tunable laser wavelength λ at normal incidence. It can be shown that for Eq. 4.2.1, the maximum value of the reflectivity $R_{FP_{\max}}$ occurs when $cos(\phi) = 1$ and the minimum value of reflectivity $R_{FP_{\min}}$ occurs when $cos(\phi) = -1$ where:

$$
\begin{aligned}
R_{FP_{\max}} &= \frac{R_1 + R_2 + 2\sqrt{R_1 R_2}}{1 + R_1 R_2 + 2\sqrt{R_1 R_2}} = \frac{(r_1 + r_2)^2}{(1 + r_1 r_2)^2} \\
R_{FP_{\min}} &= \frac{R_1 + R_2 - 2\sqrt{R_1 R_2}}{1 + R_1 R_2 - 2\sqrt{R_1 R_2}} = \frac{(r_1 - r_2)^2}{(1 - r_1 r_2)^2}
\end{aligned}
\qquad (4.2.3)
$$

Note that the Eq. 4.2.3 expressions are simplified by using the relations $R_1 = r_1^2$ and $R_2 = r_2^2$ where r_1 and r_2 are the Fresnel amplitude reflection coefficients for the chip front and back interfaces, respectively. Given the input light travels through air with refractive index $n_0 = 1$, SiC chip with index n, and external hazardous zone with index n_1, the Fresnel power reflection coefficients for the SiC chip front and hazard zone interfaces can be written as:

135

$$R_1 = |r_1|^2 = \frac{(n - n_0)^2}{(n + n_0)^2}$$

$$R_2 = |r_2|^2 = \frac{(n_1 - n)^2}{(n_1 + n)^2}.$$

(4.2.4)

Traditionally, a high quality Fabry-Perot cavity with deep highly narrow notches (or peaks) is designed by making highly reflective (> 95 % reflectivity) internal surfaces of the Etalon. For 6H-SiC in the near infrared region with $n = 2.57$ [15-16] and the SiC chip placed in air, using Eq. 4.2.4 gives $R_1 = R_2 = R = 0.193$. Although single crystal SiC acts as a natural etalon, it is also a very weak etalon in air due to its near 19 % reflectivity at the crystal interfaces. In fact, the classic Fabry-Perot effect is so weak that the interaction of laser light with the natural SiC crystal in air can be well approximated by classic two beam interferometry. This can be verified by the fact that the first light beam reflected off the first air-SiC interface has 19.3% (as $R = 0.193$) of the input beam laser power while the beam reflected by the second SiC-Air interface and returning to the sensor detector as a second optically delayed beam has a 12.5% of input laser power [as $R(1-R)^2 = 0.125$]. The third beam returning to the sensor detector after three reflections and double delay due to the SiC-Air interfaces and has only a 0.47 % power of the original input laser beam. Hence for the proposed SiC crystal-based sensor, one can use the first two beams from the SiC chip as the dominant terms for optical interference leading to the classic two-beam interferometry situation. Furthermore, if the SiC chip is placed in a hazard zone where the hazard zone contains materials other than air, R_1 and R_2 will further decrease making the two-beam interference approximation even stronger. Using this SiC specific two-beam approximation, the instantaneous detected optical power can be rewritten as:

$$P_m = K \cdot R_{FP} \approx K\left[R_1 + (1 - R_1)^2 R_2 + 2(1 - R_1)\sqrt{R_1 R_2} \cos\phi\right]$$

(4.2.5)

136

where R_{FP} is the instantaneous optical reflectivity of the basic front-end SiC Fabry-Perot element while K is a constant that depends upon the experimental conditions such as input power, power meter response gain curve, beam alignments, and losses due to other optics. In addition, optical noise in the system with time can also change the amount of light received for processing, thus varying the constant K.

The overall goal of the proposed optical sensor is to use a minimally invasive technique to measure a single crystal SiC chip-based optical parameter that can then provide the temperature at the remoted SiC chip position. As seen from Eq. 4.2.5, the optical phase ϕ of the SiC chip is an appropriate sensor parameter for measurement and sensor processing. Eq. 4.2.5 also shows that the SiC sensor measured P_m power values will approximate a sinusoidal functional behavior. This behavior is favorable for further data processing that will utilize phase difference values of these measured sinusoidal optical power data signals. Do note that exact expressions for the $P_{m_{max}}$ and $P_{m_{min}}$ values can be given as in these cases $cos(\phi) = 1$ (for a maximum) and $cos(\phi) = -1$ (for a minimum). These instantaneous $P_{m_{max}}$ and $P_{m_{min}}$ are given by:

$$P_{m_{max}} = KR_{FP_{max}} = K\frac{R_1 + R_2 + 2\sqrt{R_1 R_2}}{1 + R_1 R_2 + 2\sqrt{R_1 R_2}}$$

$$P_{m_{min}} = KR_{FP_{min}} = K\frac{R_1 + R_2 - 2\sqrt{R_1 R_2}}{1 + R_1 R_2 - 2\sqrt{R_1 R_2}}.$$

(4.2.6)

Measurement of these localized maximum and minimum optical power values is important for normalizing the measured raw P_m data to generate the measured $cos(\phi)$ function that cannot exceed ± 1 values. Given any measurement P_m that follows a sinusoidal measurement

137

behavior with a given $P_{m_{\max}}$ maximum value and $P_{m_{\min}}$ minimum value as achieved for a weak SiC etalon, this sinusoidal function rides on a Bias level given by Bias= $0.5\{ P_{m_{\max}} + P_{m_{\min}} \}$ with a max-to-min power swing given by $\{ P_{m_{\max}} - P_{m_{\min}} \}$. To normalize this sinusoidal function so its maximum and minimum values are +1 and − 1, respectively, one must subtract the bias from the power value P_m and then divide the whole function by 0.5 of the swing value, i.e.., implement the calculation $\{ P_m - \text{Bias}\}/ \{0.5[P_{m_{\max}} - P_{m_{\min}}]\}$, which gives the normalized value of the cosine function or Eq. 4.2.7. This measured $cos(\phi)$ function using the normalization of the raw P_m data is given as:

$$\cos(\phi) = 2\frac{P_m - 0.5\times(P_{m_{\max}} + P_{m_{\min}})}{P_{m_{\max}} + P_{m_{\min}}}. \qquad (4.2.7)$$

where $P_{m_{\max}}$ and $P_{m_{\min}}$ are the sensor measured localized optical power maximum and minimum values, respectively. The measured optical phase and phase difference values will then be used to compute the temperature measured by the sensor. Do note the equivalence of Eq. 4.2.5 representing the sensor theory and Eq. 4.2.7 that is used to implement the sensor data processing. Specifically, Eq. 4.2.5 can be rewritten to show that the Cosine of the OPL is equal to the measured optical power P_m minus a bias term and the resulting value divided by another scaling term. In effect, Eq. 4.2.7 and Eq. 4.2.5 have the same format and hence Eq. 4.2.7 is used for real-time sensor data processing.

Note that based on the dynamic range of the single crystal SiC defined OPL parameter ϕ change due to temperature, the $cos(\phi)$ sinusoidal behavior can be over many cycles.

Furthermore, based on the specific experimental conditions, the values of $P_{m_{\max}}$ and $P_{m_{\min}}$ can change for each specific cycle. Hence for calculating the OPL via an instantaneous P_m for a given sensing parameter condition, the $P_{m_{\max}}$ and $P_{m_{\min}}$ values within the respective OPL change single cycle should be used. Thus, for proper sensor operation of determining an instantaneous cos(OPL) and hence the instantaneous measurement parameter of temperature, the numerical operation of Eq. 4.2.7 needs to be implemented. This operation is done by measuring PD_1 provided three power levels; namely, optical power P_m at the chosen wavelength and then measuring the closest (i.e., within one optical power min/max cycle), the values of $P_{m_{\max}}$ and $P_{m_{\min}}$. Key to these measurements is that the scaling factor K should be the same for all three measurements. As mentioned before, K depends on various experimental parameters such as laser power and beam alignment that can be maintained during a given measurement set. In addition, P_m, $P_{m_{\max}}$, $P_{m_{\min}}$ depend on the instantaneous values of R_{FP}, $R_{FP_{\max}}$, and $R_{FP_{\min}}$, respectively. Note from Eq. 4.2.4 that $P_{m_{\max}}$ and $P_{m_{\min}}$ only depend on the SiC etalon interface Fresnel power coefficient values of R_1 and R_2. In-turn, R_1 and R_2 depend on the instantaneous refractive index n of SiC and the refractive indices of the chip front (i.e., n_0) and back-face (i.e., n_1) materials. On the other hand as seen from Eq. 4.2.1, P_m not only depends on the instantaneous values of R_1 and R_2, but also depends on the cos (OPL) value where the OPL term contains not only the instantaneous refractive index of SiC, but also the instantaneous SiC chip thickness d and the optical wavelength λ set for the tunable laser. Here-in lies the method to rapidly measure the instantaneous values $P_{m_{\max}}$, $P_{m_{\min}}$ for a given measured instantaneous P_m at the chosen wavelength. Specifically, after recording P_m, the tunable laser is rapidly swept in

139

wavelength about λ to make $cos(OPL) = 1$ and thus produce a $P_{m_{max}}$ measurement. Similarly, the

tunable laser is swept in wavelength about λ to make $cos(OPL) = -1$ and thus produce a $P_{m_{min}}$

measurement. As all three PD_1 power measurements are now available, Eq. 4.2.7 is solved to get

a value for the instantaneous $cos(OPL)$ that will undergo signal processing to determine the

sensing parameter of temperature. A key condition for the accuracy and robustness of this

normalization process is that the instantaneous SiC refractive index n over the wavelength sweep

range is essentially constant, thereby keeping R constant for all three PD_1 power measurements

of P_m, $P_{m_{max}}$, and $P_{m_{min}}$. It is also important that all three measurements are taken for the same

exact experimental conditions (apart from wavelength) so that K and T are the same during this

measurement set. One can study the effect of changing wavelength on the SiC refractive index

by differentiating the OPL $\phi = \{4\pi /\lambda\} \{n\, d\}$ with respect to the wavelength giving:

$$\frac{d\phi}{d\lambda} = 4\pi d\left[\frac{-n}{\lambda^2} + \frac{1}{\lambda}\frac{dn}{d\lambda}\right] \text{or } d\phi = 4\pi d\frac{\lambda dn/d\lambda - n}{\lambda^2}d\lambda \quad (4.2.8)$$

The maximum wavelength change is required when either $P_m = P_{m_{max}}$ or $P_m = P_{m_{min}}$. In both

these cases, a maximum $d\phi = \pi$ is required to change the PD_1 power reading from the maximum

to minimum or vice versa. Hence, using Eq. 4.2.8 with the maximum tunable laser wavelength

change conditions given by:

$$d\phi = \pi, \ d\lambda = \Delta\lambda_{max}, \text{ and } dn = \Delta n, \quad (4.2.9)$$

where $\Delta\lambda_{max}$ is the needed maximum wavelength change and Δn is the refractive index change

caused by this wavelength change. Using the Eq. 4.2.9 conditions and rearranging the terms of

Eq. 4.2.8, one gets the needed maximum wavelength change $\Delta\lambda_{max}$ to be:

$$\Delta\lambda_{max} = \lambda\frac{\Delta n}{n} - \frac{\lambda^2}{4nd} \qquad (4.2.10)$$

Equation 4.2.10 thus provides a relationship for the maximum change in tunable laser wavelength required to produce the desired local maxima $P_{m_{max}}$ and minima $P_{m_{min}}$, given an instantaneous P_m value of the sensor. Note that Eq. 4.2.10 requires knowledge of the change in refractive index Δn of the SiC material with respect to the wavelength. For 6H-SiC single crystal material, this change in refractive index in the infrared band (e.g., 1500-1600 nm) is very small, e.g., < 0.01 % .[15-16] For example, assuming a 0.01% change in refractive index for a 300 µm thick SiC chip with a refractive index of 2.57 at a wavelength of 1550 nm, the resultant $\Delta\lambda_{max}$ is found to be 0.77887 nm. However, if one neglects the change in refractive index term in Eq. 4.2.10, $\Delta\lambda_{max} = 0.77902$ nm. Note that the 0.00015 nm difference in $\Delta\lambda_{max}$ for these two cases is extremely small and practically out of the tuning step of a typical commercial laser source. Hence, a small < 1 nm range wavelength sweep of an eye safe 1550 nm band tunable laser will be sufficient to generate the required $P_{m_{max}}$ and $P_{m_{min}}$ values of light power required for normalization (via Eq. 4.2.7) of sensor instantaneous P_m data.

For another set of new P_m, $P_{m_{max}}$, $P_{m_{min}}$ measurements for perhaps a different K (scaling constant affected by for instance receiver beam alignment) and T (i.e., temperature in hazardous zone) situation, a new cos(OPL) can be computed that is also correctly normalized for further signal processing. Thus, each near instantaneous three power set reading of P_m, $P_{m_{max}}$, and $P_{m_{min}}$ is self-normalized to give the appropriate cos(OPL) data. Take the simple case of when the SiC chip sits in an air surrounding implying $R_1 = R_2 = R$. In this case using Eq. 4.2.6, the extreme power readings can be written as:

$$P_{m_{max}} = K \frac{4R}{(1+R)^2}$$
$$P_{m_{min}} = 0 \qquad\qquad (4.2.11)$$

If the values of K and R (due to possible change in SiC front and back interface Fresnel reflection coefficient parameters) fluctuate over different instantaneous 3-reading power sets, the peak modulation swing $4KR/(1+R)^2$ of the PD_1 power cycle (see Eq. 4.2.11) may change but the *cos*(OPL) data due to the self-normalization process from the sensor system is still accurate and robust for further signal processing. This attribute of the proposed sensor is particularly attractive for fossil fuel applications where the proposed sensor front-end SiC chip will be exposed to extreme mechanical and chemical effects that can alter receive beam alignments and also change refractive index of the medium surrounding the SiC chip that will cause a change/decrease in the Fresnel power coefficients of the SiC chip. Because the proposed sensor signal processing and operations is robust to such changes, a powerful sensor can be realized for extreme environments. This attribute is all the more powerful when compared to standard Fabry-Perot-based sensors using broadband light and power spectrum measurements where the Fabry-Perot etalon must maintain its given spectral shape throughout sensor operations. Hence any changes in Fresnel coefficients will drastically affect the quality of the spectral filter function that will make detection of the shifts of the spectral maxima/minima all the more difficult. Recall that shaped Fabry-Perot filter functions require highly reflective etalon interfaces, a key limitation in extreme fossil fuel applications where these interface reflectivities can severely degrade with extreme and cycle temperature swings.

The proposed instrument can also be calibrated in a continuous mode as explained next. In this case, wavelength tuning is not required to generate the $P_{m_{max}}$ and $P_{m_{min}}$ values required for

normalization. Instead, the sensing parameter such as temperature is swept over the desired

sensing zone that causes the SiC refractive index n and chip thickness d to change that in-turn

causes the required max/min cos(OPL) change to produce naturally induced $P_{m_{max}}$ and $P_{m_{min}}$

values at PD_1. In this case, once all the P_m data is recorded over the whole sensor calibration

temperature range, $P_{m_{max}}$ and $P_{m_{min}}$ values within a given one cycle zone are used to normalize all

the P_m values within this given one cycle power data. In this special case, it must be shown that

$P_{m_{max}}$ and $P_{m_{min}}$ remain constant over any one power variation cycle for the proposed SiC chip.

Recall that the Fresnel power reflectivity R for the SiC chip in air can be written as:

$$R = \frac{(n - n_0)^2}{(n + n_0)^2}$$
(4.2.12)

Taking the derivative of Eq. 4.2.12 on both sides with respect to the refractive index n:

$$dR = \frac{2(n - n_0)}{(n + n_0)} \left\{ \frac{(n + n_0) - (n - n_0)}{(n + n_0)^2} \right\} dn$$

$$\Rightarrow \Delta R = \frac{4n_0(n - n_0)}{(n + n_0)^3} \Delta n$$
(4.2.13)

Now consider that the sensor chip OPL $\phi = \frac{4\pi n d}{\lambda}$ undergoes a π phase change to

introduce one optical power cycle variation detected by PD_1. This power variation can be due to

the combined effect of change in refractive index and thickness of SiC. However, as a worst case

scenario, it is assumed that the change in OPL is only due to the SiC refractive index change.

Note that this condition imposes an extreme restriction on the OPL change while in practical

situations; the actual restriction being less severe due to the accompanied change in thickness.

Nevertheless, the corresponding change in refractive index of SiC associated with one optical power cycle is given by $\Delta n = \dfrac{\lambda}{4d}$. Using this value of Δn in Eq. 4.2.13, the corresponding change in R, the coefficient of power reflectivity of the front-end sensor chip is given by:

$$\Delta R = \frac{n_0(n - n_0)}{(n + n_0)^3} \frac{\lambda}{d} .\qquad (4.2.14)$$

Again the worst case for R change will be for SiC in air or $n_0=1$. As an example, using a value of $n=2.6$ typical for single crystal 6H-SiC, a thickness of 0.5 mm, and $\lambda= 1550$ nm, a ΔR of 0.000106 or 0.0106% is obtained. This minute change in PD_1 detected optical power reflectivity is very small to influence the per power cycle data P_m normalization procedure. Hence the assumption of constant R_1 and R_2 for one power variation cycle proposed for the sensor continuous-mode calibration is valid.

4.2.3 Proposed Sensor Signal Processing for Unambiguous Temperature Sensing

Now consider the proposed sensor used for measuring some arbitrary temperature T that induces changes in both refractive index and thickness of the SiC chip. The variation of chip refractive index thickness product or $n \times d$ induces a change in the PD_1 detected optical power where:

$$\cos\{\phi(T)\} = \cos\left\{\frac{4\pi n(T)d(T)}{\lambda}\right\} = \left\{2\frac{P_m - 0.5 \times (P_{m\max} + P_{m\min})}{P_{m\max} - P_{m\min}}\right\},\qquad (4.2.15)$$

$$\phi(T) = \cos^{-1}\left\{2\frac{P_m - 0.5 \times (P_{m\max} + P_{m\min})}{P_{m\max} - P_{m\min}}\right\}.\qquad (4.2.16)$$

Here λ is the wavelength of operation. For a given instantaneous temperature T of the SiC chip remotely placed in the sensing environment of temperature T, PD$_1$ records the three optical power levels P_m, $P_{m_{max}}$, $P_{m_{min}}$ (as mentioned earlier), and hence the instantaneous phase $\phi(T)$ can be computed. To calibrate the sensor, this procedure is repeated for the desired temperature range of T_{min} to T_{max}. The sensor provided instantaneous $\phi(T)$ phase value change from the minimum temperature to the maximum temperature given by $\Delta\phi_1(T)$ can be expressed as:

$$\Delta\phi_1 = \left\{ \frac{4\pi n(T_{max})d(T_{max})}{\lambda_1} \right\} - \left\{ \frac{4\pi n(T_{min})d(T_{min})}{\lambda_1} \right\} = 2\pi m + \sigma_1. \qquad (4.2.17)$$

Here, because of the rather large (e.g., 300 μm) proposed thickness of the SiC chip, $\Delta\phi_1$, the unwrapped phase obtained from Eq. 4.2.16 by adding 2π after each cycle, is expected to have m number of 2π phase cycles plus a possible fixed phase value of σ_1. Because of the presence of multiple power cycles, a phase ambiguity arises in the sensor data obtained using P_m data at λ_1. This phase ambiguity can be removed by measuring the instantaneous sensor phase $\phi(T)$ at another carefully selected wavelength λ_2. This wavelength λ_2 is selected such that the total unwrapped phase shift change $\Delta\phi_2$ in going from T_{min} to T_{max} is increased by π and given by:

$$\Delta\phi_2 = \left\{ \frac{4\pi n(T_{max})d(T_{max})}{\lambda_2} \right\} - \left\{ \frac{4\pi n(T_{min})d(T_{min})}{\lambda_2} \right\} = 2\pi(m+0.5) + \sigma_1. \qquad (4.2.18)$$

Here, the unwrapped phase difference defined as $\phi_{12} = \Delta\phi_1 - \Delta\phi_2 = \pi$ as the temperature changes from T_{min} to T_{max}. Note that the refractive index is assumed to be the same for wavelengths λ_1 and λ_2. Based on earlier reported experimental data for 6H-SiC in the near infrared band, this approximation is indeed valid, particularly when the two wavelengths are

within 100 nm of each other as later shown in the experimental section of this paper.[15-16] Solving Eq. 4.2.17 and Eq. 4.2.18 gives:

$$\lambda_2 = \lambda_1 \frac{2\pi m + \sigma_1}{2\pi(m+0.5)+\sigma_1}. \qquad (4.2.19)$$

Equation 4.2.19 is used to select the second wavelength of operation for the proposed temperature sensor. Note that the additional phase shift σ_1 can be made zero by either selecting wavelength λ_1 such that the total phase shift is an integral multiple of 2π or by selecting the T_{min} and T_{max} such that σ_1 vanishes. In these cases with $\sigma_1 = 0$, Eq. 4.2.19 can be rewritten as:

$$\lambda_2 = \lambda_1 \frac{m}{m+0.5}. \qquad (4.2.20)$$

Note that the process of unwrapping the instantaneous phase $\phi(T)$ is for design purposes to verify proper unambiguous sensor processing conditions via dual wavelength selection. For a given temperature T, the proposed sensor must generate PD$_1$ provided P_m, $P_{m_{max}}$, $P_{m_{min}}$ optical power data set values at Eq. 4.2.20 based two pre-selected optical design wavelengths of λ_1 and λ_2. These power values are used to compute the instantaneous sensor phase values of $\phi_1(T)$ and $\phi_2(T)$ at the temperature T. This process is repeated for the entire temperature range of T_{min} to T_{max} and then the instantaneous sensor phase difference $\Delta\phi(T) = \phi_1(T) - \phi_2(T)$ is calculated. Using Figure 4.2.5 power data, a unique set of values of $\Delta\phi$ and $\phi_1(T)$ (or $\phi_2(T)$) exists for each temperature value eliminating the sensor power data ambiguity problem. Note that $\Delta\phi$ changes from $-\pi$ to π and completes many cycles as the temperature changes over the designated T_{min} and T_{max} range. During the sensor calibration process, the $\Delta\phi$, T, $\phi_1(T)$ (or $\phi_2(T)$) values are stored. During sensor real-time temperature sensing operations, $\Delta\phi$ and $\phi_1(T)$ (or

$\phi_2(T)$) are measured and matched to the unique T in the computer table that gives the same values for $\Delta\phi$ and $\phi_1(T)$ (or $\phi_2(T)$. Because today's commercial tunable lasers can be reset quickly (e.g., 1 ms) and accurately (e.g., within 0.01 nm), the proposed sensor can quickly provide the desired sensing parameter, i.e., temperature value where the SiC chip is remotely placed.

4.2.4 Proposed Sensor Demonstration from Room Conditions to 1000^0C

The Figure 4.2.2 proof-of-principle sensor system is set-up in the laboratory to demonstrate the feasibility of the Figure 4.2.1 design. A single SiC chip with no coatings present is placed and sealed in the experimental high temperature chamber based on induction heating. SiC used is 6H single crystal type with a refractive index of 2.57 provided by AppliCote Associates, Florida.[15-16] Using Eq. 4.2.8, the SiC chip front surface power reflection coefficient is calculated to be $R = 0.193$ implying that 19.3% of the input strike light on the chip take a first bounce off the chip to return to the photo-detector. On the other-hand, the light reflected first bounce back from the high temperature exposed rear surface of the SiC chip has a power reflection coefficient given by $R(1-R)^2 = 0.125$ or 12.5 % of the input laser light. Light returning to the photo-detector after a second bounce from the SiC chip high temperature interface is a much smaller $R^3(1-R)^2 = 0.0047$ or 0.47 % fraction of the original input laser light power. These first order calculations firstly imply that about 0.193+0.125=0.318 or approximately 32 % of the input light power will return from the SiC chip to strike the receive photo-detector. Second, the natural reflection properties for the SiC chip in air produces strong two beam interferometry that is expected to give a classic sinusoidal interference function.
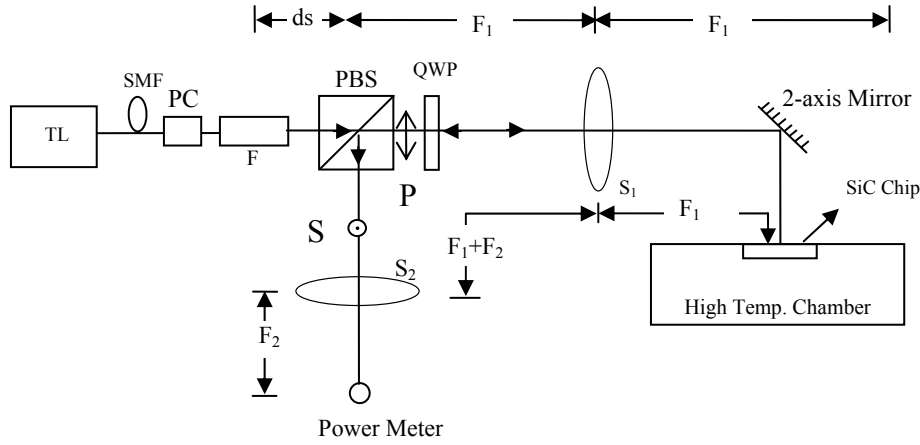
Figure 4.2.2: Experimental set-up of demonstrated SiC-based minimally invasive optical sensor for extreme temperature measurements. TL: Tunable laser, PBS: Polarization Beam Splitter, QWP: Quarter Wave Plate, SMF: Single Mode Fiber. F: Fiber Lens of self imaging type with half self imaging distance d_s where beam waist w_i is located ; S_1/S_2 Imaging Lenses of focal lengths FL_1/FL_2.

Given the proposed sensor system's high efficiency (> 30%), a typical lower power 1.5 mW tunable laser source is used to launch light into the freespace optics coupled to the SiC chip. Specifically, the tunable laser has a wide 1500-1600 nm tuning range with a 0.01 nm tuning step and 0.0005 nm laser line-width. As seen in Figure 4.2.2., the tunable IR laser is collimated by a fiber Graded Index Rod (GRIN) lens with a d_s =6 cm half self-imaging distance and a 0.44 mm $1/e^2$ beam waist diameter or approximately 0.88 mm null-to-null beam size. The half-self imaging distance for the GRIN lens is where the Gaussian beam has a minimum beam waist and hence perfect collimation.[17] A mechanical fiber-based polarization controller (PC) is used to produce the desired horizontal (or p) polarization light that exits the GRIN lens. This collimated light from the GRIN-lens passes through a PBS and only lets p- polarization light to pass through towards the SiC chip. Hence, the PBS works as a polarization noise filter to prevent any

unwanted s or vertical polarization input light from reaching the SiC chip. A lens S_1 is placed between the GRIN lens and SiC chip to prevent large beam expansion. The distance between the fiber lens and imaging lens S is 36 cm, where FL_1=30 cm is the focal length of S_1 and 6 cm is from the GRIN half self-imaging distance. The distance between S_1 and SiC chip is 30 cm. The PBS is placed 15 cm before S. A QWP plate oriented at 45^0 to the horizontal or p-axis is placed between the PBS and S. The QWP converts the input linear p-polarization to circular polarization. As the SiC chip is a birefringent material, using circularly polarized input light makes the sensing system polarization independent to the SiC chip rotational orientation. A FL_2=10 cm focal length sphere S_2 is placed 25 cm from the PBS deflected port, and a large area Newport photo-detector with a 3 mm diameter is placed 10 cm away from lens S_2. All optics are anti-reflection (AR) coated for the near IR 1550 nm band.

With the given optical design in Figure 4.2.2, the Gaussian beam waist is formed on the SiC chip and the photo-detector. The light beam waist on the SiC chip is 0.88 mm null-to-null beam size while on the detector it undergoes a factor of 3 reduction in size to 0.29 mm due to ratio of focal lengths FL_1/FL_2 = 30 cm/10 cm. This demagnification of the beam size makes the sensor received beam easily located within the 3 mm diameter active area of the Newport free-space coupled detector. Unlike Figure 4.2.1, no active alignment mirrors are used because of the large area of the photo-detector size and the static and controlled environment of the SiC chip placed in the high temperature test chamber. The chamber consists of a small (~7.9 mm diameter) hole in a stainless steel disk. The hole is covered with an induction heating coil powered by a 2.5 kW, 200 KHz, 240/380/480 V, 3-Phase alternating current power supply. The hole is sealed by placing the SiC chip on the opening with ceramic insulator rings that clamp the chip into position. The chip boundary is free to expand as it is not restricted in the sealing

ceramic package. A steel disk is used to clamp the entire assembly from the top. The chip sits mid-way between the coil positioning to provide a uniform temperature to both sides of the chip. A salient feature of the chamber design is the reduced size of the steel cavity and hence small SiC chip exposure area which reduces stress variations across the exposed chip surfaces. There are no measurable optical reflections from the background of the chip as the steel cavity is terminated with a non-optical quality plate. The chip acts like a sealed optical window in the induction heating-based high temperature chamber. The chamber assembly has coarse translation stages to adjust the position of the laser beam with-respect to the SiC chip designated targeting zone. An external fixed mirror M_1 with fine x-y tilt control is used to make sure that the laser beam strikes the SiC chip at normal incidence. The 6-H SiC single crystal chip used has a 300 μm thickness and a 0.5 cm x 0.25 cm rectangular size. Reference temperature T of the SiC chip is monitored by a K-type thermocouple that is in contact with the SiC chip zone that is external to the test chamber but close (within 1 mm) to the probe optical beam. The thermocouple wire is inserted from the top steel plate through the ceramic rings and placed directly in contact with the top side of the SiC chip so it measures the heated chip temperature.

The freespace laser beam only interacts with a small 0.88 mm diameter central targeted region on the SiC chip. Hence, high quality (e.g., $\lambda/50$) optical flatness requirements are only subjected to a very small region of the chip front and back surfaces. Note that for proper in-line interferometry, the front and back surfaces of the SiC chip over the active laser region must be parallel to enable high spatial coherence optical detection. In case, the surfaces are slightly non-parallel, a fringe pattern will appear on the detector surface. One can practically alleviate this issue by using a pin-hole placed in front of the photo-detector with the pinhole size much smaller that a single fringe cycle. In this way, high spatial coherence interferometric data can be taken as

needed for proper sensor operations. Single crystal SiC is known as an excellent optical quality material and hence it is optically suited for the proposed minimally invasive sensor design. In our case, the used SiC chip surfaces were the desired quality and no pinhole use was required where the large area Newport point photo-detector acted as a natural pin-hole.

To demonstrate proof-of-concept sensor operations, an experiment is performed where the optical power by the sensor photo-detector is continuously recorded using a temperature chamber and hence SiC chip heating from room temperature to 1000 ^{0}C. Here the chosen tunable laser wavelength λ_1 = 1547.0 nm, giving m = 37 optical power detection 2π cycles over the designed room temperature to 1000 ^{0}C sensor range (see Figure 4.2.3). Using the wavelength design Eq. 4.2.20 with m = 37 and λ_1 = 1547.0 nm, one gets λ_2 = 1526.4 nm that should provide 37.5 optical power detection 2π cycles. To stay within experimental margin of error, a slightly higher value of λ_2 = 1530 nm is used such that one does not exceed the unambiguous range of π phase shift. The sensor photo-detector optical power and temperature data are recorded using a computer where 750 data sets are recorded as the SiC temperature is increased from near room temperature to 1000 ^{0}C using current heating of the test chamber. A better sensor resolution can be achieved over the same near 1000 ^{0}C range using more data samples per optical power cycle. In effect, the proposed sensor can zoom into a specific temperature zone and take extensive power data using accurate optical power meters and fast sampling data analog-to-digital converters. Hence, accurate calibration of the sensor can be implemented using the proposed robust signal processing methods.
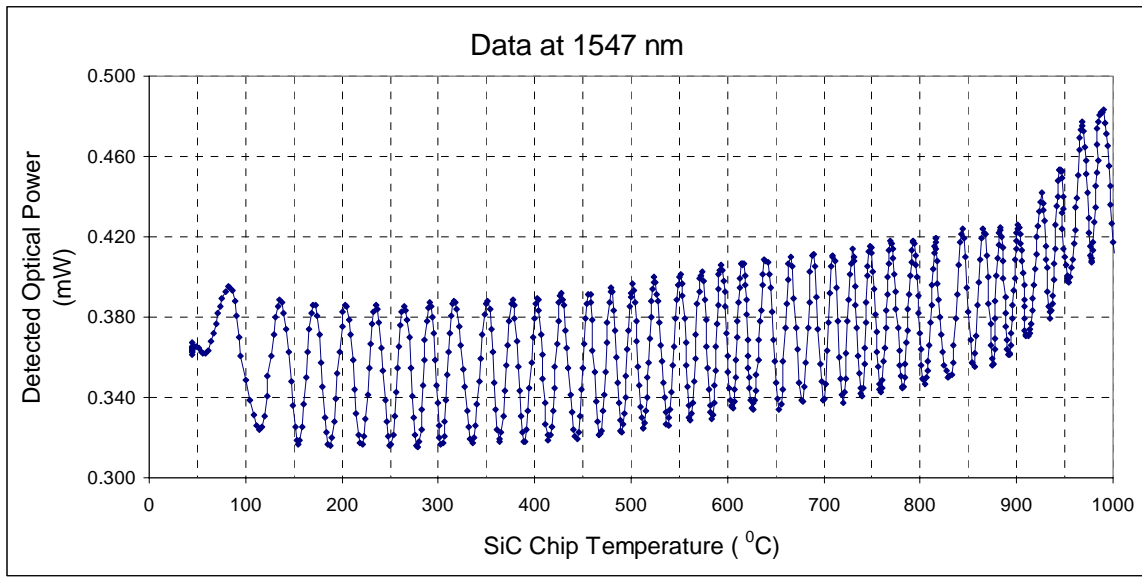
Figure 4.2.3: Sensor provided raw optical power measurements at 1547 nm as the SiC chip temperature is raised to 1000^0C.
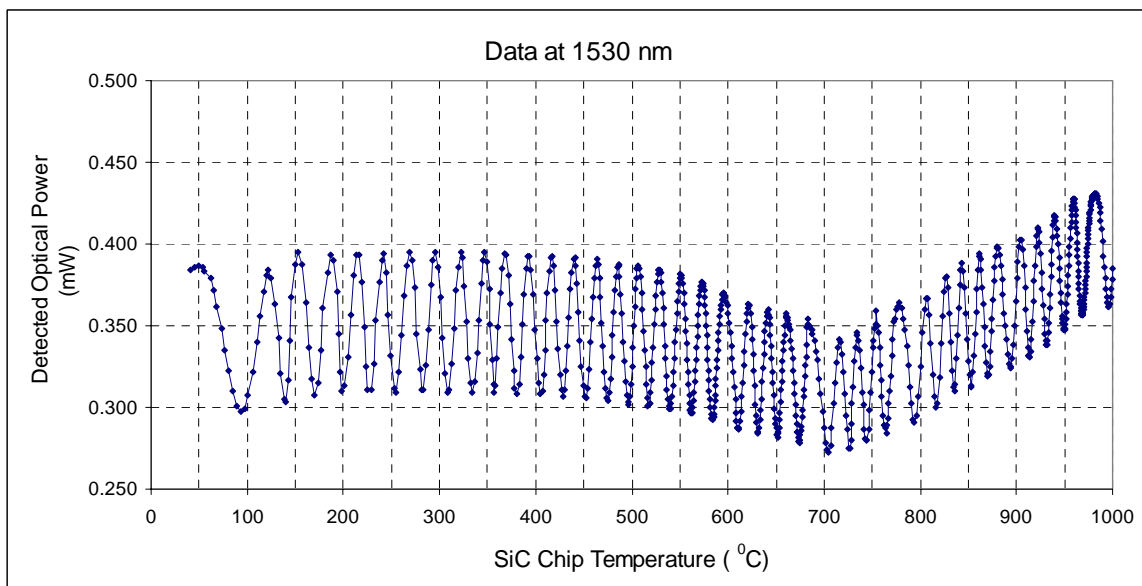
Figure 4.2.4: Sensor provided raw optical power measurements at 1530 nm as the SiC chip temperature is raised to 1000^0C.

Figure 4.2.3 and 4.2.4 show the raw sensor optical power data in mWs obtained for two different wavelengths using the computer automated power and temperature measurement set-

up. Note that over the 1000°C temperature measurement process, as expected, the power maximum and minimum values per cycle change depending on the time varying experimental conditions such as mechanical vibrations, thermal gradients, and air currents that affect the optical returning beam to the photo-detector. Because the present experiment is characterizing the proposed optical sensor, one can store the optical power data over the entire temperature band and then process optical power data per cycle to produce the required normalized plot of the cosine of the chip optical phase ϕ versus temperature. Figure 4.2.5 shows this normalized cos{$\phi(T)$} plot obtained for the two wavelengths of 1530 nm and 1547 nm.
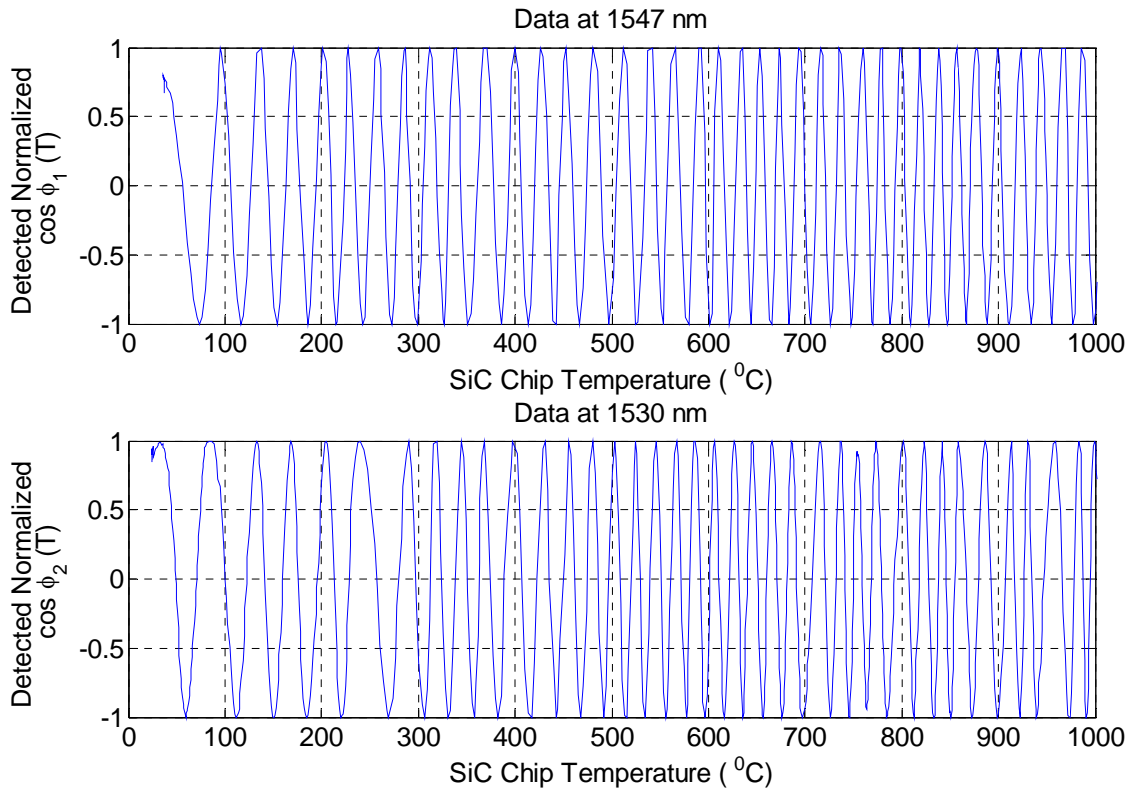
Figure 4.2.5: Sensor provided normalized cos{$\phi_1(T)$} and cos{$\phi_2(T)$} measurements at 1530 nm and 1547 nm as the SiC chip temperature is raised to 1000^0C.

153
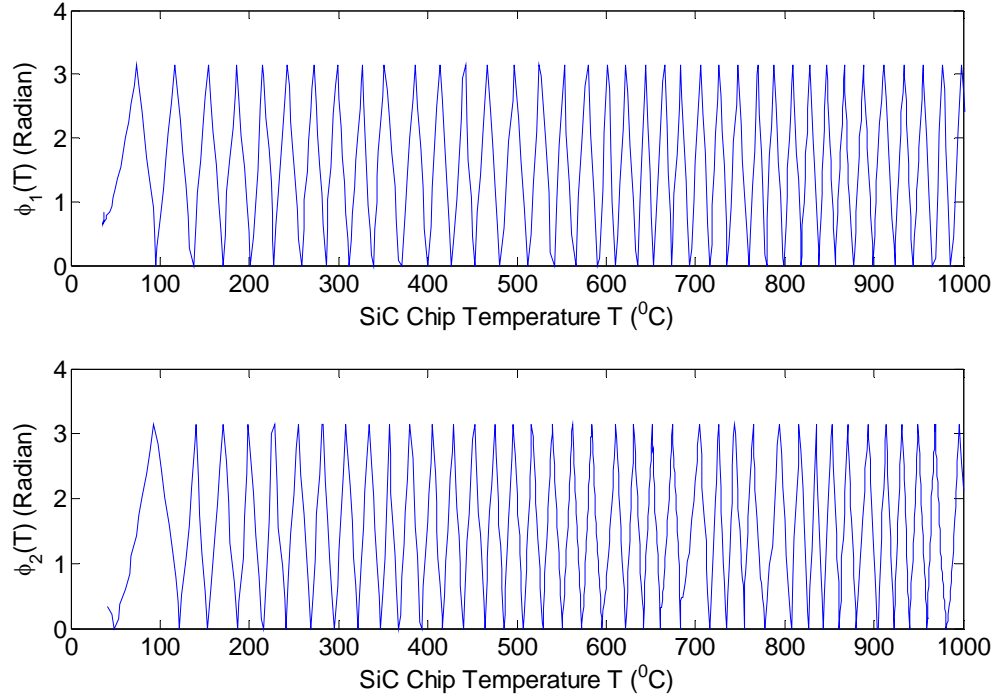
Figure 4.2.6: Instantaneous phase calculated by using data in Figure 4.2.5 at 1547 and 1530 nm.

Using data from Figure 2.4.5, the instantaneous phase at the two wavelengths is shown in Figure 4.2.6. Figure 4.2.3 and 4.2.4 show the sensor's data ambiguity issue as the same values of *cos{$\phi(T)$}* occur for many different values of temperature. To check the elimination of the data ambiguity in the gathered data set, one simply takes into consideration the number of cycles recorded and adds 2π after each cycle to get an unwrapped phase value. This mathematical operation can be done in software and these unwrapped $\phi(T)$ phase value results in radians for the Figure 4.2.3 experimental data are shown in Figure 4.2.7 and Figure 4.2.8. Note in Figure 4.2.5 for the room temperature to 1000 ^{0}C range, the optical power for 1547 nm sweeps 37 cycles while for 1530 nm sweeps the expected almost 37.5 cycles. Hence experiments conducted at wavelengths of λ_1= 1547 nm and λ_2= 1530 nm give the desired unwrapped phase values $\Delta\phi_1(T)$ and $\Delta\phi_2(T)$, respectively.

154
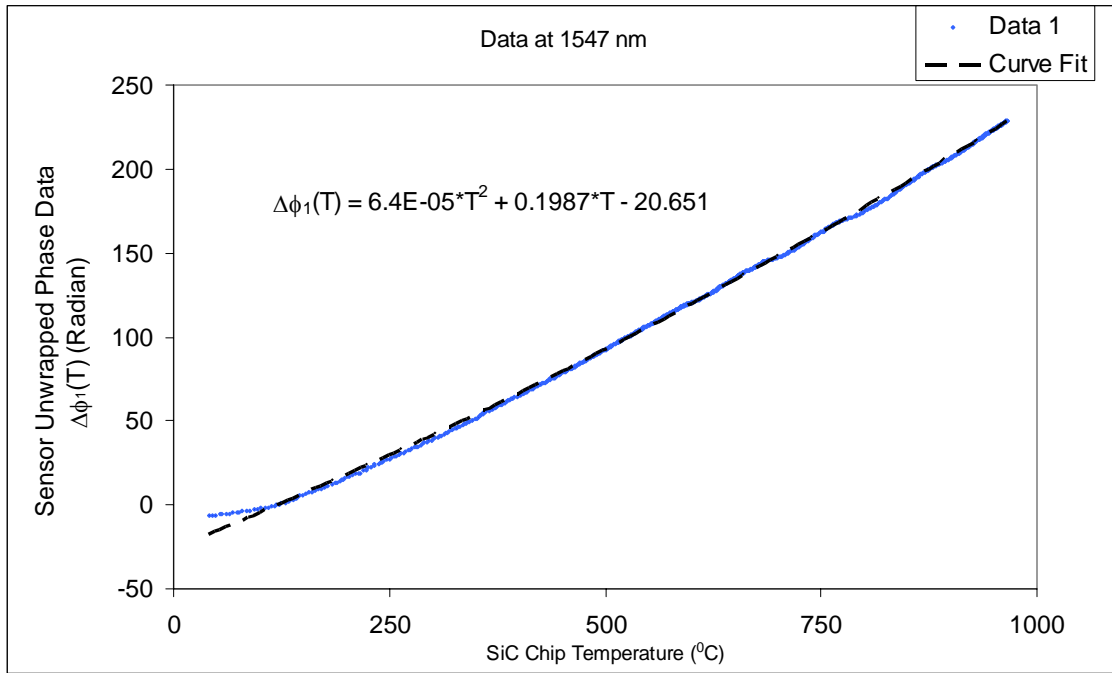
Figure 4.2.7: Sensor unwrapped phase shift data $\Delta\phi_1(T)$ in radian versus SiC Chip temperature (^{0}C) with data taken at 1530 nm. A weak quadratic curve fit is achieved for this data.
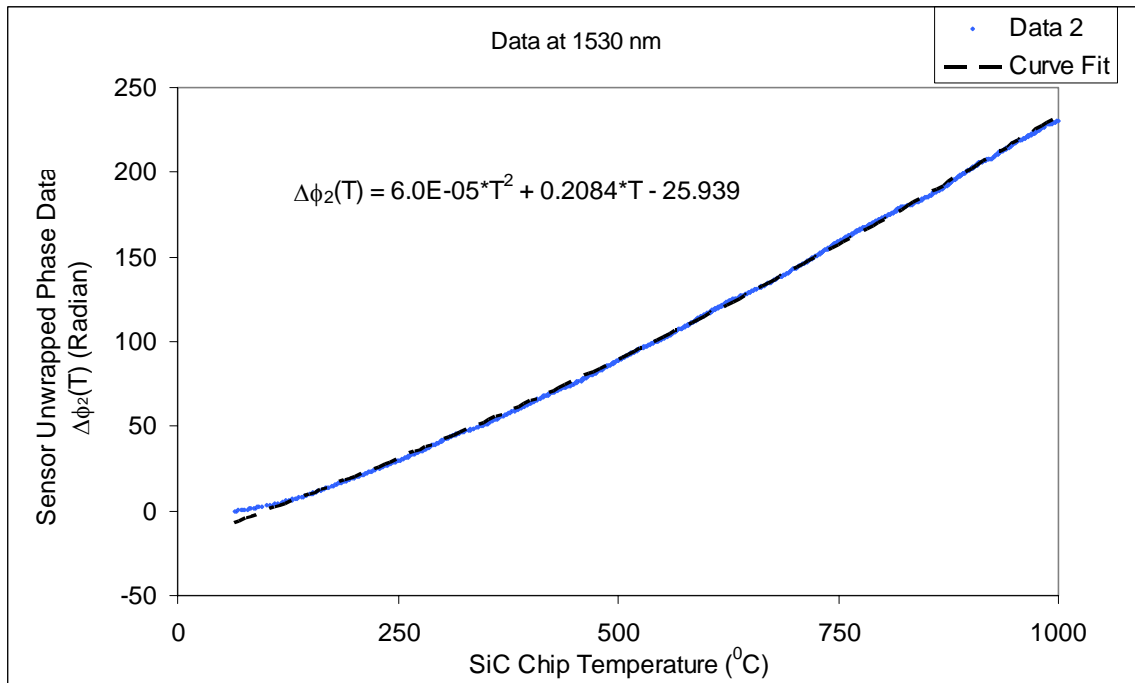
Figure 4.2.8: Sensor unwrapped phase shift data $\Delta\phi_2(T)$ in radian versus SiC Chip temperature (^{0}C) with data taken at 1547 nm. A weak quadratic curve fit is achieved for this data.

155

Next, the curve fits to the $\Delta\phi_1$ and $\Delta\phi_2$ data are used to calculate $\phi_{12} = \Delta\phi_1(T) - \Delta\phi_2(T)$ and ϕ_{12} is plotted in Figure 4.2.9. Note that this unwrapped phase difference $\phi_{12}(T)$ is slightly less than π radians for the temperature range from 35^0C to $1000\ ^0C$, as needed for the implemented sensor design. Thus the data in Figure 4.2.9 does show how the 37 ambiguous cycles of phase data versus temperature have been converted to almost a single unambiguous π cycle making the gathered sensor data appropriate for processing.
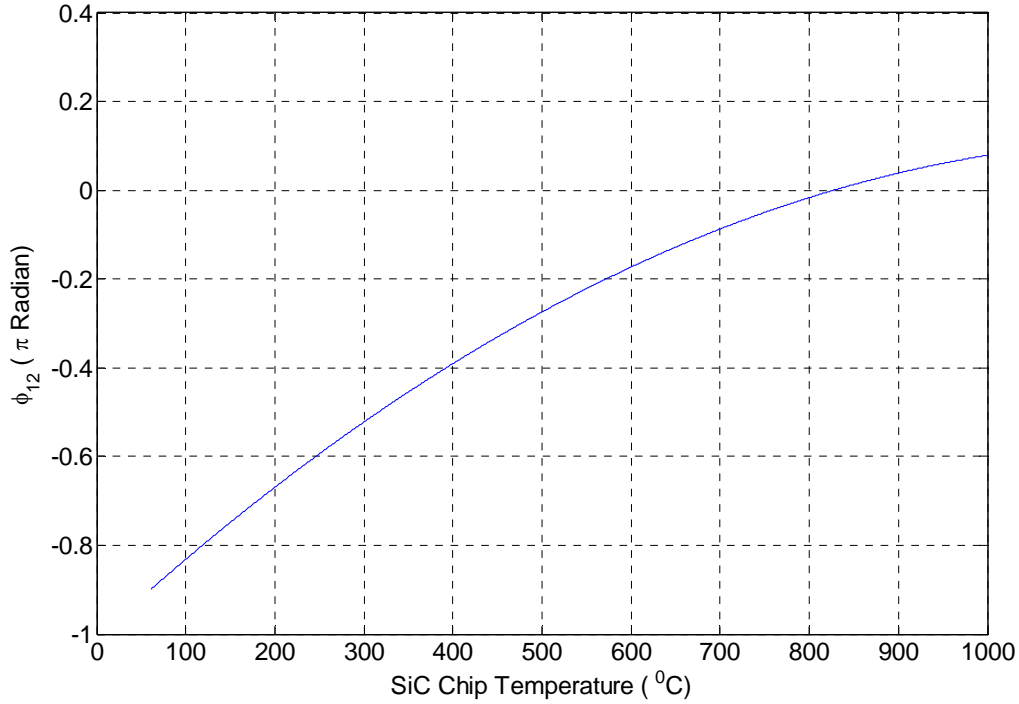
Figure 4.2.9: Unwrapped phase shift difference $\phi_{12} = \Delta\phi_1 - \Delta\phi_2$ data for the two wavelengths used for the sensor operations.

For real time temperature measurement via the sensor, the two wavelength calibration data is used, hence eliminating the need to unwrap the phase data from the sensor. The instantaneous phase difference unlike unwrapped phase difference takes values from $-\pi$ to π. However, this instantaneous phase difference $\Delta\phi(T)$ and the corresponding instantaneous

156

phase $\phi_1(T)$ (or $\phi_2(T)$) produces a unique pair and when compared to the stored calibration data set provides a unique unambiguous temperature value. The instantaneous phase difference $\Delta\phi(T)$ clalculated by using instantaneous phase data at two wavelengths shown in Figure 4.2.6 is presented in Figure 4.2.10. Note that there are still many instants at which the instantaneous phase difference $\Delta\phi(T)$ has same values, however these same values occur at a different value of $\phi_1(T)$ (or $\phi_2(T)$) thus providing a unique value of temperature T.
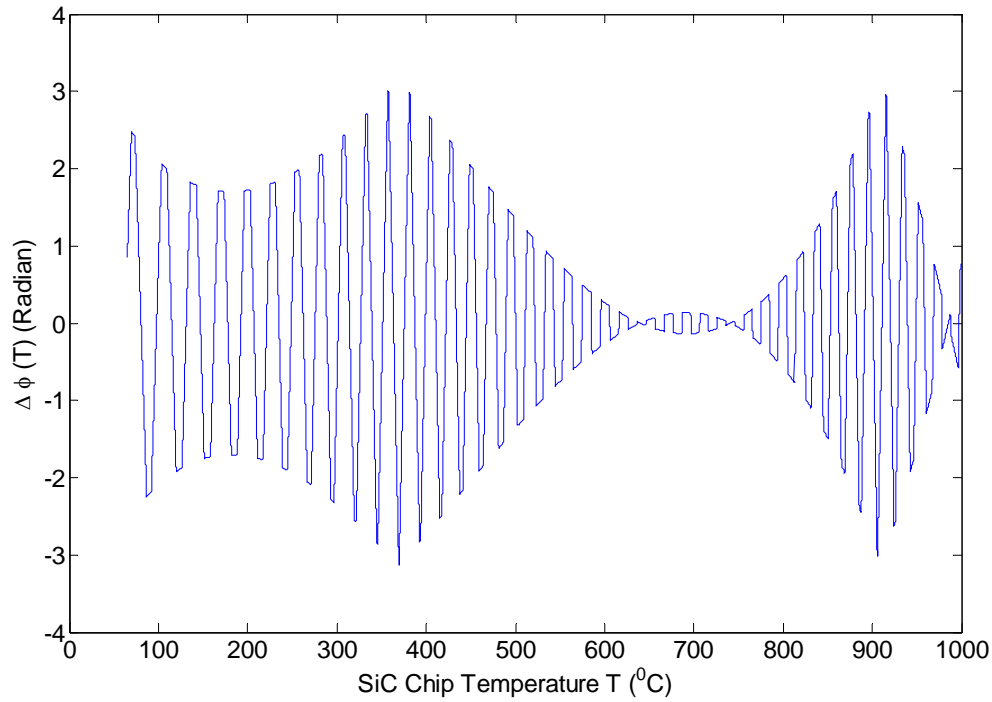
Figure 4.2.10: Instantaneous phase difference between data at 1547 nm and 1530 nm calculated using instantaneous phase data in Figure 4.2.6.

The temperature resolution depends upon the stored calibration data. As 750 data values are taken from room temperature to 1000^0C, hence, the average sensor resolution based on the given data sampling range is computed to be approximately 970 ^{0}C / 750 ~ 1.3 ^{0}C. Note that a 2π radian or 360^0 phase shift in the measured optical power is produced by a near 30^0C temperature

change in the lower temperature zone. Therefore a 1^0C temperature shift corresponds to $2\pi/30^0$C = 0.21 radians based on instantaneous phase change Also note that at higher temperature of 1000^0C, a 20^0C temperature shift corresponds to a phase change of $2\pi/20^0$C = 0.314 radian, an improvement of about 66% in the resolution as compared to 0.21 radian at room temperature. This shows that the sensor temperature resolution improves as the temperature increases. To visually illustrate this novel ability of the sensor signal processing, a three dimensional (3-D) plot with axes of $\Delta\phi(T)$, ϕ_1 , and T is generated using measurements for the two wavelengths at the room temperature to 100 ^{0}C temperature range. This curve shown in Figure 4.2.11 shows a helical spring like behavior where for every set of values of $\Delta\phi$ and ϕ_1, there is only one value of the temperature corresponding to that data set. Note that the extended sensor experimental calibration curve to 1000 ^{0}C is again a spiral curve (like Figure 4.2.11) with changing pitch according to the changing period of the chip OPL parameter variations. Here again there is no ambiguity in the temperature measurements provided by the proposed sensor.

For sensor signal processing, the optical phase shift is not being calculated directly. In fact, optical power readings are taken that are then used to calculate the phase values. It has been explained earlier that a typical equivalent phase resolution is 0.21 radians. Note that the raw power data in Figure 4.2.3 and 4.2.4 shows a 0.1 mW power change between the maxima and minima that corresponds to a π phase shift. Hence, a 0.21 radian change will correspond to a power change of 0.1 mW $\times$ 0.21/π = 6.6 μW. Commercially available power meters can easily measure optical power accurately to nano-Watts (nWs). Therefore, optical power measurement instrumentation will not cause computational errors in the sensor processing. Furthermore, the

laser power can be increased to any desired higher value so that the minimum power change per

degree temperature change is significantly higher than the detector noise.
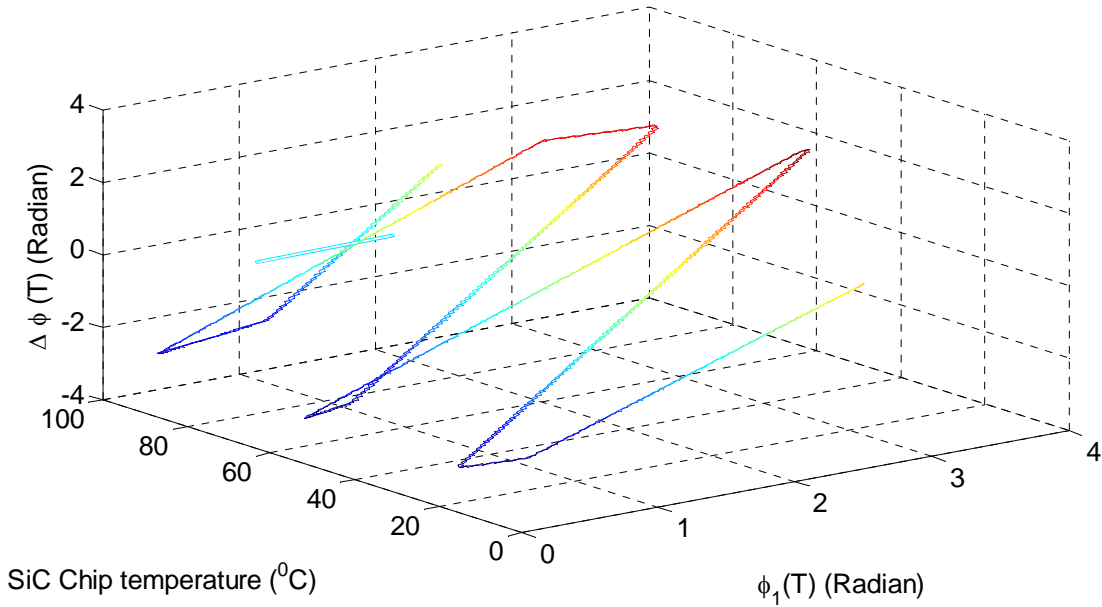
Figure 4.2.11: Three dimensional (3-D) representation of the sensor calibration chart for the unambiguous instantaneous temperature measurement via the demonstrated sensor from room conditions to 100^0C. This 3-D plot uses the instantaneous phase difference data $\Delta\phi(T)$, instantaneous phase shift $\phi_1(T)$, and given temperature T.

Thus, the proposed minimally invasive single crystal SiC chip-based optical sensor when

used with the proposed signal processing can provide true unambiguous temperature

measurements for extremely high temperatures that the single crystal SiC can naturally withstand

in environmentally unfriendly settings. Quantitatively, the effect of temperature on the proposed

single crystal SiC-based optical sensor has been investigated and results for the used 300 μm

thick SiC chip showed a 2π OPL change (or $\phi(T)$ phase shift change) for an average temperature

change range of 30 to 20 ^{0}C. More specifically around room temperature, a 30 ^{0}C change causes

a 2π optical power cycle. Later at the extreme 1000 ^{0}C temperature, the SiC refractive index and

159

thickness are at a higher value causing a 2π optical power cycle for a smaller 20^0C change in temperature. These results also point out that the proposed SiC sensor requires calibrated data for proper operations over a wide sensing parameter range. Another point to note is that the sensor performance can be considered coded in temperature period, i.e., a given temperature value is always within a specific sensor temperature period for a 2π optical power cycle. This particular effect can also be used to extend the unambiguous temperature detection range of the proposed sensor. Starting with the defined sensor OPL parameter expression at a λ_1 wavelength and temperature T :

$$\phi(T) = \left\{ \frac{4\pi n(T) d(T)}{\lambda} \right\}. \tag{4.2.21}$$

Taking the derivative of both sides of Eq. 4.2.21 gives:

$$\frac{d}{dT} \{\phi(T)\} = \frac{4\pi}{\lambda} \left[d(T) \frac{\partial}{\partial T} n(T) + n(T) \frac{\partial}{\partial T} d(T) \right]. \tag{4.2.22}$$

The rate of change of phase or $d\phi(T)/dT$ governs the variation of the temperature change causing a full power cycle. If this rate remains constant, there is no variation in temperature change value that produces a full optical power cycle. According to Eq. 4.2.22, the rate of change of phase is governed by two rates, i.e., $\frac{\partial}{\partial T} n(T)$, also known as the thermo-optic coefficient (TOC) and $\frac{\partial}{\partial T} d(T)$ called the coefficient of thermal expansion α. Both these factors increase with increasing temperature, in particular, the TOC as cited in Ref. [15-16]. In fact, the TOC doubles for a change of 300^0C from room temperature. The increase in TOC increases the refractive index and therefore the optical path length (or the optical phase shift) increases at a greater speed producing an increase in the rate of change of phase with temperature. Note that

Eq. 4.2.22 also contains refractive index and thickness in them and the absolute increase in these factors further enhances the value of rate of phase change at higher temperature. Hence, the temperature change that causes a full power cycle decreases with temperature increase because now the phase change of 2π is obtained for smaller change of temperature. This explains why the full optical power cycle temperature change decreases from a value of 30^0C at room temperature to a value of 20^0C at 1000^0C.

Finally, do note that the proposed sensor can also be operated in an alternate signal processing wideband wavelength swept mode that simulates a broadband input source in time. Because state-of-the-art commercial tunable lasers in the 1550 nm band can sweep wavelength at a fast millisecond regime, a wide (e.g., 100 nm) spectral source can be quickly synthesized for the proposed sensor. In this case, the proposed sensor can generate the Fabry-Perot wavelength response of the SiC etalon at the instantaneous temperature without requiring a spectral resolution limited optical spectrum analyzer instrument. Nevertheless, the peak or notch movement of the synthesized received optical spectrum will have to be monitored to access temperature change, thereby running into the temperature sensing resolution constraints limited with monitoring individual notch or peak positions when the etalon spectral shape can deteriorate with changing high hazard extreme sensing conditions. In effect, if the deep notch (or peak) shape changes to a spectrally broad notch (or peak), the sensor temperature resolution will degrade. Furthermore, this data processing is based on a non-robust approach where over the entire temperature range of the sensor, one looks for one given optical power minimum (or maximum) value (here we are assuming equal notch depths) and determines temperature value by measuring the wavelength shift for this minima (or maxima). In the proposed sensor signal processing, full cycle optical power readings and not just a minima (or maxima) power reading

gives the sensor measured temperature. Hence, the proposed sensor can use a more robust approach to processing that takes into account many optical power readings and not just a localized minima (or maxima) power reading. Of course, both signal processing methods can be engaged in the proposed sensor without any hardware changes, thus adding built-in redundancy and fault-tolerance to the temperature measurements via the proposed minimally invasive sensor.

Note that the proposed system does not require super-accurate positioning on a micron or $< 0.01^0$ scale as needed with near field SMF optics where coupling light from a freespace beam to a SMF requires extreme precision.[18] This is because the proposed sensor system is a hybrid fiber-freespace design system where the SMF is used to launch a high spatial quality small beam spot size (e.g., < 0.5 mm diameter) laser beam in the sensing target region and the large aperture freespace beam capture receive optics is used for the return beam power-based detection. Specifically, transverse alignment on both transmit and receive beams is done on a rather large sub-millimeter scale (e.g., 1 mm) implying that the transmit beam hits within for example a 1 mm diameter zone of the SiC chip where the chip is also optically flat over the target zone. Similarly, the receive beam hits within a 1 mm diameter zone of the receive optics that can be a large 3 mm diameter freespace optical detector such as used for the demonstrated experiment or a large diameter multi-mode fiber. Note that the Figure 2.2.1 shown alignment and beam control mirror optics using today's state-of-the-art mirrors [19] can scan at fast kilo-Hertz (KHz) rates keeping beams on the chip and receive detector targets despite environmental effects such as vibrations. In addition, these mirrors are excellent for sub-degree high resolution beam pointing allowing the freespace transmit beam to be quickly and accurately angularly adjusted for near normal incidence targeting of the thick SiC chip.

4.2.5 Single Crystal SiC Refractive index Measurements:

Another important aspect of the SiC-based optical sensor system is its ability to predict the material characteristics of the frontend SiC chip. Specifically, the thickness and the refractive index change of SiC is of special interest for the practical implementation of the high temperature sensing and measurement system. For these measurements of refractive index and thickness, Eq. 4.2.17 can be modified as:

$$\Delta\phi(\Delta P) = \phi(P_f) - \phi(P_i) = \left\{\frac{4\pi n(P_f)d(P_f)}{\lambda_1}\right\} - \left\{\frac{4\pi n(P_i)d(P_i)}{\lambda_1}\right\} \quad . \quad (4.2.24)$$

Here P is some parameter that influences the refractive index and the thickness of the optical sensor chip as it changes from state i to state f. The corresponding change in the optical phase is given by $\Delta\phi(\Delta P)$ and can be calculated by repeated application of Eq. 4.2.16. It can be seen from Eq. 4.2.24 that the refractive index and the thickness of the SiC chip are coupled together and can be expressed as:

$$d(P_f) = \frac{\Delta\phi(\Delta P)\lambda_1}{4\pi n(P_f)} + \frac{n(P_i)d(P_i)}{n(P_f)}, \qquad (4.2.25)$$

$$n(P_f) = \frac{\Delta\phi(\Delta P)\lambda_1}{4\pi d(P_f)} + \frac{n(P_i)d(P_i)}{d(P_f)}. \qquad (4.2.26)$$

Equation 4.2.25 shows that the thickness of the SiC material can be calculated if the initial state, i.e., the initial thickness and the refractive index and the final refractive index are known. Similarly Eq. 4.2.26 can be used to calculate the refractive index of the SiC chip given the initial refractive index and thickness along with the final thickness value. In the case of temperature experiments, the external parameter P is the temperature of the SiC chip. In this case, the initial thickness of the chip used for experiments is measured to be 300 μm and the refractive index in

the 1550 nm IR region is given in prior art as 2.57 at room temperature. The thickness change of

the chip can be expressed as:

$$d(T_f) = [1 + \alpha \Delta T] d(T_i) = [1 + 4.7 \times 10^{-6} \times (T_f - T_i)] 300 \times 10^{-6} \qquad (4.2.27)$$

Here $\alpha = 4.7 \times 10^{-6} / {}^0C$ is the coefficient of thermal expansion for SiC.[32]
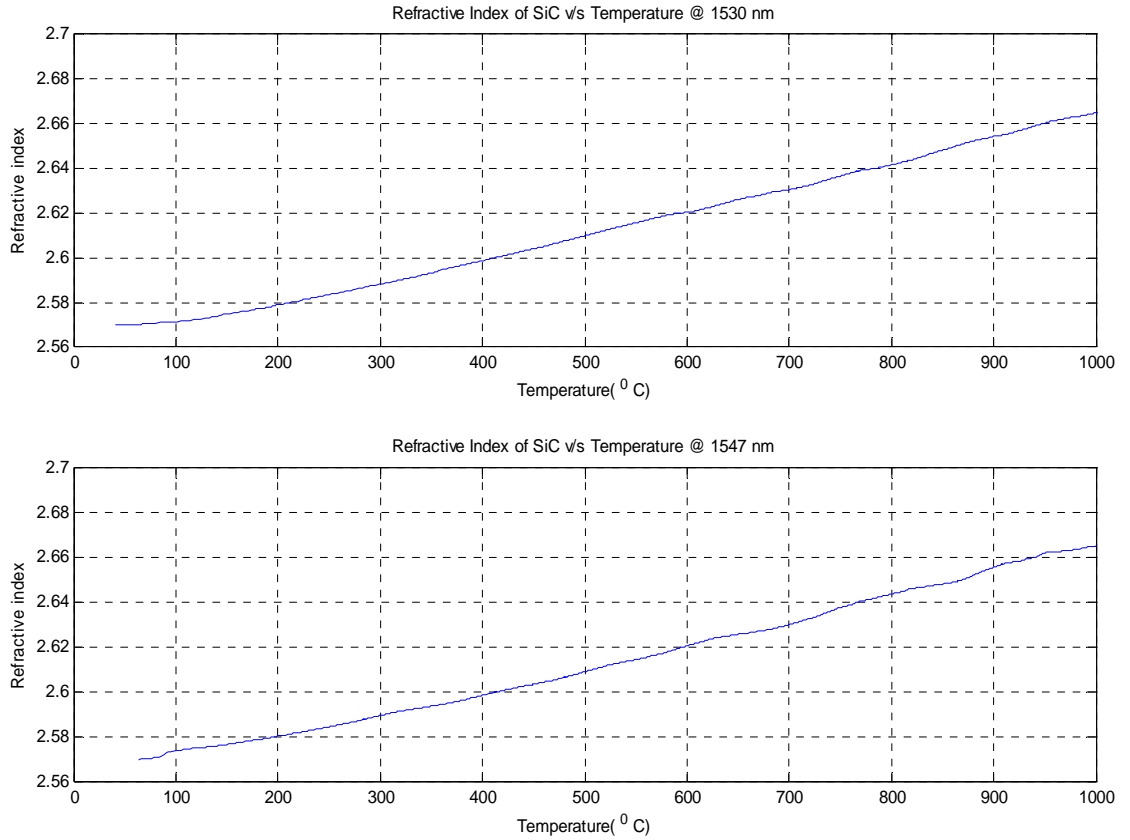
Figure 4.2.12: Plot of refractive index of the used single crystal SiC in the sensor with index variation shown from room temperature to 1000^0C at two different wavelengths of 1530 nm and 1547 nm.

Using Equations 4.2.26 and 4.2.17 and the $\Delta\phi(T)$ data from earlier experiments (Figure 4.2.7

and 4.2.8 are used to calculate $\Delta\phi(T)$) in addition to the initial refractive index value of 2.57 for

164

SiC, the refractive index is calculated (see Figure 4.2.12) for SiC from room temperature to 1000^0C at the two different wavelengths of 1530 nm and 1547 nm. The calculated refractive index at 1530 nm at 1000^0C is found to be 2.6655 while that at a wavelength of 1547 nm is found to be 2.6656, indicating a change of 0.0001 in the refractive index value at the two different wavelengths. This in-turn confirms the assumption that the refractive variations of SiC with respect to the wavelength in the IR region are very minimal.

4.2.6 High Temperature and Pressure Chamber

A special test chamber for temperature and pressure measurements is fabricated with an automated data acquisition system using thermocouples, programmable logic controller (PLC), and LabView software. The system is shown in Fig. 4.2.13. A single crystal 6H-SiC is used as the sensing element as shown in Fig. 4.2.14. The SiC is polished on both sides without any coating on the surfaces.
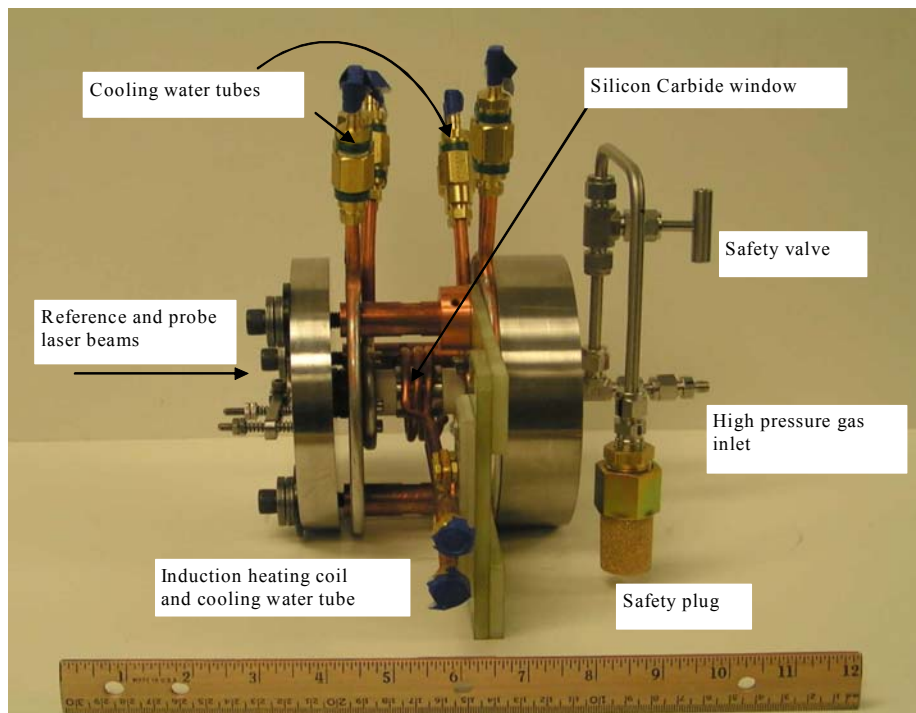
Figure 4.2.13: Fabricated novel high temperature and high pressure test chamber
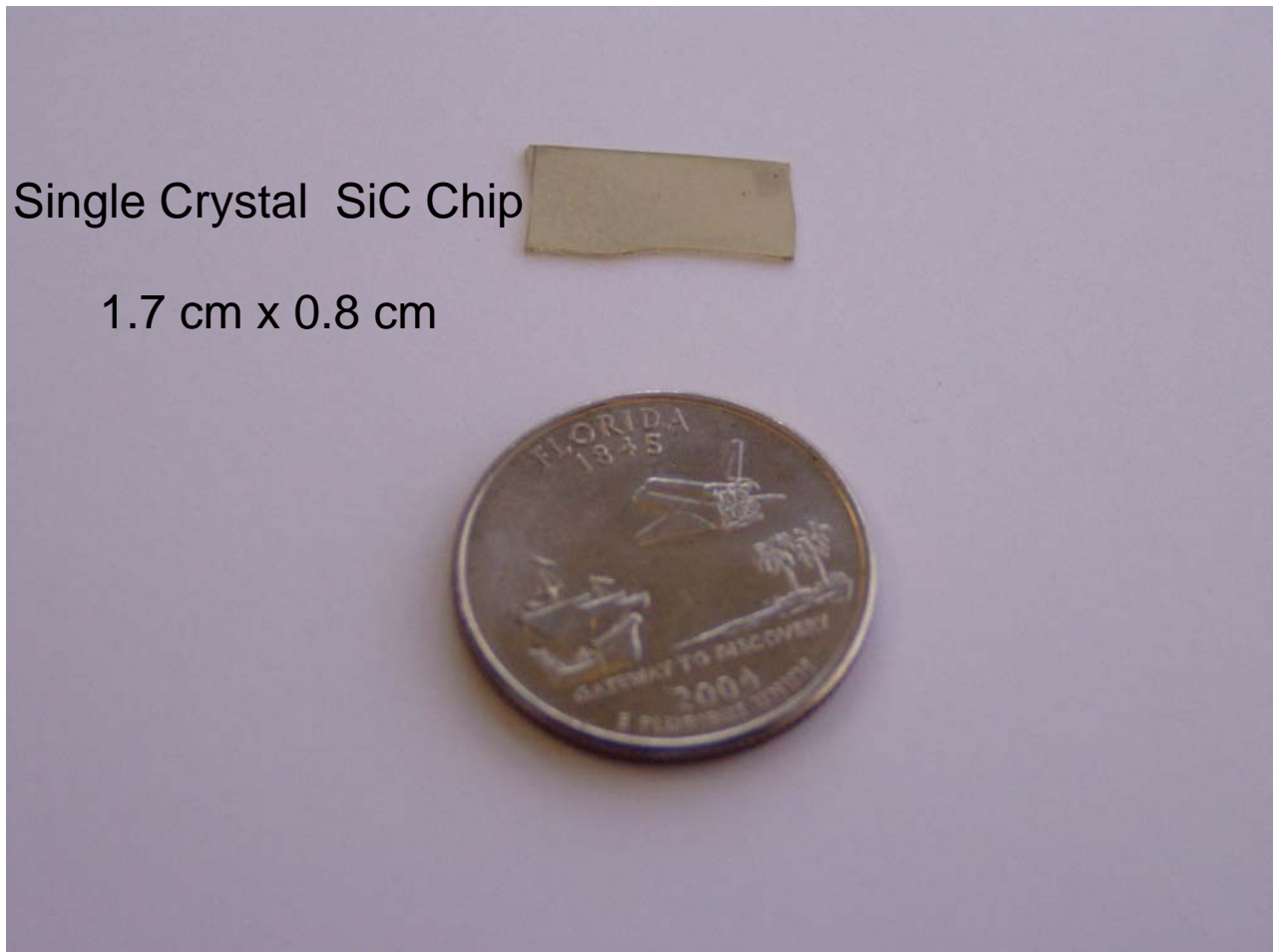
Figure 4.2.14: Sample single crystal SiC chip used in high temperature high pressure experiments.

4.3 Applications of Interferometric Sensor in Optical Metrology

The proper design and performance of all-optical and optoelectronic devices requires knowledge of optical properties of materials. Some of these important optical properties include refractive index, reflectivity, and absorption. For proper device and system design, the measurement of refractive index is of prime importance. The refractive index of any material

depends upon a large number of factors that include temperature, pressure, wavelength, and other environmental conditions like atmospheric gas concentrations and humidity. For key optical materials such as crystalline and amorphous silicon, the temperature dependence of refractive index n usually dominates the other mentioned factors.[20] The temperature T dependence of the refractive index is characterized by the thermo-optic coefficient (*TOC)* given by $\frac{\partial n}{\partial T}$. In particular, the *TOC* can change significantly as temperature is increased over a wide (e.g., 1000 K) range. Hence indirect measurement of the *TOC* using interpolation of lower temperature range data is not an accurate *TOC* measurement technique and direct *TOC* should be measured for higher temperatures.[21,22] A number of approaches have been used to measure the *TOC* of optical materials (e.g., GaAs, Si, and InP) using optics including direct techniques and indirect measurements.[23-26] Optical interferometry is an important tool in fast, reliable and accurate measurement of refractive indices.[27,28] In particular, the Fabry-Perot interferometric behavior of a test sample has been used to measure the refractive index and *TOC*. Here, by measuring the detuning of the detected multiple beam interference signal produced by a Fabry-Perot etalon test sample from its resonance position, the *TOC* is determined.[29] It is important to note that the spectral resolution of the Fabry-Perot interferometer formed by the sample under test determines the *TOC* measurement resolution. In order to get clear resonance peaks (or dips) in the etalon spectrum, the optical reflectivities of the two sides of the etalon must be sufficient (e.g., > 20 %). Hence care must be taken in preparing the etalon sample under test to enable the moderately high reflectivity for the two interfaces of the etalon.

Silicon Carbide (SiC) is an excellent optical material due to its superior thermal, mechanical, electrical, and chemical inertness properties. Single crystal 6H-SiC is in particular

an optical quality (i.e., flat on an optical wavelength scale) large band gap planar material that can be fabricated in large sizes (e.g., > 2 cm diameter wafers) and can withstand high temperatures (e.g., 2500 K) and pressures (50 atmospheres). Recently, a single crystal 6H-SiC based temperature sensor using optics has been designed and demonstrated for a room temperature to 1273 K temperature range.[30,31] Therefore, it is important to measure optical properties of 6H SiC for a wide range of temperature conditions. To date, to the best of the author's knowledge, the *TOC* of 6H-SiC has been measured up-to 600 K with no extreme temperature data available as needed for high temperature sensing applications.[32] In addition, it is well known that 6H-SiC shows birefringence behavior.[33] Previously reported 6H-SiC measurements did not taken into account the effect of material birefringence in their measurements. In addition, the 6H-SiC samples used had poor etalon reflectivities that led to poor spectral resolution for the etalon and hence low quality 6H-SiC *TOC* data plots.

In this section, for the first time is experimentally reported the *TOC* for 6H-SiC from near room temperature to extreme 1273 K conditions. In particular, the *TOC* measurement system takes into account the birefringent nature of the 6H-SiC sample and provides high resolution *TOC* data plots using the natural high quality etalon behavior of the single crystal 6H-SiC bulk sample. In addition, the freespace-fiber hybrid *TOC* measurement system operates at the attractive eye safe telecommunications band around 1550 nm.

4.3.1 Theory of Measurement of Thermo-optic Coefficient

The experimental set-up is same as explained in section 4.2 as shown in Figure 4.2.2. Consider that in Figure 4.2.2 the optical light power P_{FP_m} measured by the power meter is given

by $P_{FP_m} = K R_{FP_m}$, where K is a constant that depends upon the experimental specifications like input power, power meter response, losses due to other optics and the noise present in the system. As the noise in the system varies with time this constant K keeps changing. R_{FP_m} is the SiC etalon reflectance given by:

$$R_{FP} = \frac{R_1 + R_2 + 2\sqrt{R_1 R_2}\cos\phi}{1 + R_1 R_2 + 2\sqrt{R_1 R_2}\cos\phi} \quad, \quad (4.3.1)$$

where R_1 and R_2 are the Fabry-Perot etalon front and back mirror reflectances, respectively. ϕ is the round-trip propagation phase accumulated by an optical beam while passing through the SiC etalon of thickness t and refractive index n at a wavelength of λ, and is given by $\phi = \dfrac{4\pi n t}{\lambda}$ at normal incidence. For the SiC sample in air, $R_1 = R_2 = R = r^2$, where $r = (n-1)/(n+1)$ is the Fresnel amplitude reflection coefficient of an air-SiC interface. Eq. 4.3.1 indicates that the maximum reading of the power meter is taken when $cos(\phi) = 1$ or $\phi = 2\pi m$, where $m = 0,1,2,3,\ldots$, while the minimum reading of the power meter is taken when $cos(\phi) = -1$ or $\phi = (2m-1)\pi$. As the temperature T of the SiC sample changes by an amount dT, the optical path length in the chip changes, causing ϕ to change by $d\phi = 2\pi$ cycles, leading to consecutive optical peak (or null) measurements. By measuring the dT values that give the consecutive $d\phi = 2\pi$ cycles over a large temperature range, and since ϕ is related to the SiC sample refractive index n, the change of refractive index ∂n with temperature change ∂T can be calculated giving the desired SiC TOC. Starting with:

$$\phi = \frac{4\pi n t}{\lambda}, \quad (4.3.2)$$

and taking the derivative on both sides of Eq. 4.3.2 with respect to the temperature gives:

$$\frac{d}{dT}\{\phi(T)\} = \frac{4\pi}{\lambda}\left[t(T)\frac{\partial}{\partial T}n(T) + n(T)\frac{\partial}{\partial T}t(T)\right]. \qquad (4.3.3)$$

Here $\frac{\partial}{\partial T}n(T)$ is the *TOC* that has to be measured. Therefore Eq. 4.3.3 can be rearranged as:

$$TOC = \frac{\lambda}{4\pi t(T)}\frac{d}{dT}\{\phi(T)\} - \frac{n(T)}{t(T)}\frac{\partial}{\partial T}t(T). \qquad (4.3.4)$$

Fundamentally, the thickness t of the SiC chip also changes with temperature. Specifically, the temperature dependence $t(T)$ of the thickness is characterized by the SiC thermal coefficient of linear expansion $\alpha = 4.56\times10^{-6}$ K^{-1},[12,13] and is given by:

$$t(T) = \left[1 + \alpha\Delta T\right]t(T_i) , \qquad (4.3.5)$$

where T_i is the initial (e.g., room) temperature and $\Delta T = T - T_i$ is the temperature difference. Differentiating Eq. 4.3.5 with respect to temperature (T) gives:

$$\frac{\partial}{\partial T}t(T) = \alpha\, t(T_i) . \qquad (4.3.6)$$

Substituting Eq. 4.3.5 into Eq. 4.3.6 gives the desired *TOC* to be:

$$TOC = \frac{1}{t(T)}\left\{\frac{\lambda}{4\pi}\frac{d}{dT}(\phi(T)) - n(T)\alpha\, t(T_i)\right\}. \qquad (4.3.7)$$

Here $d\phi(T)/dT$ is determined by measuring dT that gives the desired 2π phase shift corresponding to the adjacent detected optical power peaks (or nulls), while α is a known material constant. However based on Eq. 4.3.7, $n(T)$ and $t(T)$ are required to get a value for *TOC*.

For the measurement of refractive index, one can write:

$$\Delta\phi(\Delta T) = \phi(T) - \phi(T_i) = \left\{\frac{4\pi\, n(T)t(T)}{\lambda}\right\} - \left\{\frac{4\pi\, n(T_i)t(T_i)}{\lambda}\right\} \qquad (4.3.8)$$

170

Rearranging the terms in Eq.8:

$$n(T) = \frac{\Delta\phi(\Delta T)\lambda}{4\pi\, t(T)} + \frac{n(T_i)t(T_i)}{t(T)}. \qquad\qquad (4.3.9)$$

Equation 4.3.9 shows that that the refractive index of the etalon material $n(T)$, in this case, 6H-SiC can be calculated at higher temperatures (e.g., T) if the initial state, i.e., the initial thickness $t(T_i)$ and the refractive index at room temperature $n(T_i)$ are known in addition to the elevated temperature thickness $t(T)$, the wavelength λ and the optical phase shift $\Delta\phi(\Delta T)$ change. The first term in Eq. 4.3.7 contains the term $d\phi(T)/dT$ that for a 300 μm 6H-SiC chip changes relatively faster compared to the second term containing the SiC instantaneous refractive index $n(T)$ that varies by a small relative amount with the same temperature change. Based on Ref. [30,31] data, a 300 μm 6H-SiC chip starting at room temperature produces a phase change of 2π for a 35 ^{0}C temperature change. The equivalent refractive index at a temperature of room+35^{0}C calculated by $n(T) = n(T_i) + TOC \times \Delta T$ gives a value of $2.57 + 3.0 \times 10^{-5} \times 35 = 2.5711$ where $n(T_i) = 2.57$ is given in Ref. [32]. Note that here $TOC = 3.0 \times 10^{-5}$ at room temperature has been used as cited in Ref. [32]. Using a 1550 nm wavelength, the Eq. 7 first term $\frac{\lambda}{4\pi}\frac{d}{dT}(\phi(T))$ is calculated to be

2.58×10^{-8} m/K while the Eq. 4.3.7 second term $n(T)\alpha\, t(T_i)$ provides a contribution of 3.5185×10^{-9} m/K. Hence, the contribution from the second term is smaller by a factor of 7.33 as compared to the first term for the temperature change of 35^{0}C from room temperature to ~ 335 K. A similar calculation done at 600 K where a smaller 25^{0}C change provides a 2π change gives a value of 3.10×10^{-8} m/K for the first factor in Eq. 4.3.7 while the contribution from the second factor is 3.5175×10^{-9} m/K. This calculation shows that a near 300^{0}C temperature change produces a 20% change in the first factor in Eq. 4.3.7 while the second term is changed by only 0.01%.

171

Hence, it can be inferred that the second term in Eq. 4.3.7 provides approximately an order of magnitude smaller and constant contribution to *TOC* calculations. Therefore the measured 6H-SiC *TOC* can be approximated as:

$$TOC \approx \frac{\lambda}{4\pi t(T)} \frac{d}{dT} \{\phi(T)\}. \qquad (4.3.10)$$

However, for a general material and for higher precision measurements, Eq. 4.3.7 should be used that requires prior knowledge of the refractive index at room temperature at the operating wavelength.

Data from the Figure 4.2.2 system provides the temperature locations over an entire test range that correspond to optical power peaks (or nulls) where $d\phi(T)$ has changed by 2π due to temperature change dT. Using this measured temperature data set corresponding to optical power peaks (or nulls) that can provide a numerical function representing $d\phi(T)/dT$ and using Eq. 4.3.10, the *TOC* of the test sample is numerically calculated. Next an experiment is performed using Figure 4.2.2 to measure the *TOC* of 6H-SiC at the telecom 1550 nm wavelength and extreme temperature range from near room temperature to 1273 K.

4.3.2 Experiment

Figure 4.2.2 system is setup in the laboratory using a single crystal 6H:SiC with a thickness $t(T_i)$ of 300μm (at room temperature) and a laser source at 1550 nm wavelength. The temperature of SiC is raised from room temperature to 1273 K (1000^0C) by using an electronically controlled induction heater that heats a steel cylinder on which the SiC is placed. The temperature is recorded by a k-type thermo-couple put on the SiC chip. The Figure 4.2.2

optical design is a high optical throughput set-up with polarizing multiplexing used to separate the transmit and receive light channels and no light lost in the processing optics. Given all Anti-Reflection (AR) coated components, the main light lost in the system comes only from the Fresnel loss of the 6H-SiC etalon with about 30% light returned by the etalon to the detector.
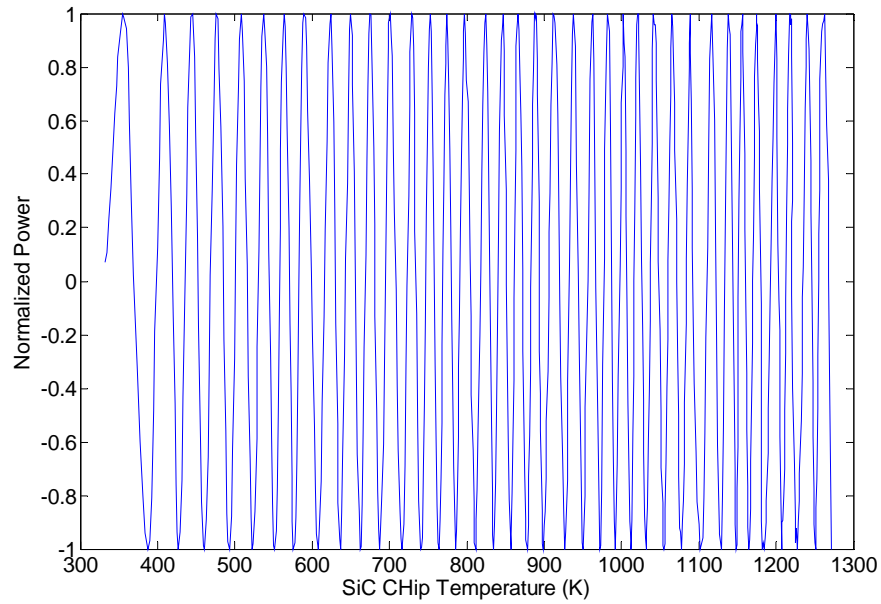

Figure 4.3.1: Normalized Power measured by the power meter in Figure 4.2.2 as the SiC chip temperature is increased from near room temperature to 1273 K.
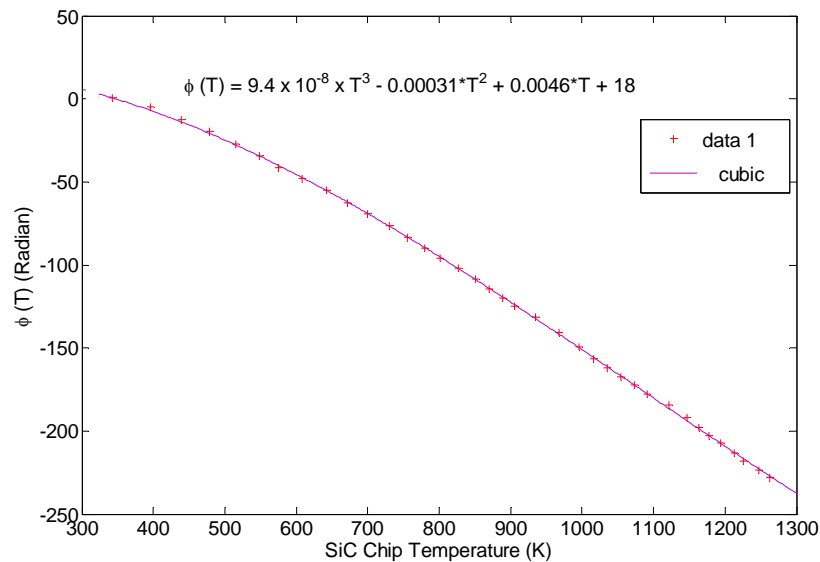

$$\phi(T) = 9.4 \times 10^{-8} \times T^3 - 0.00031*T^2 + 0.0046*T + 18$$

Figure 4.3.2: Plot of measured modulo-2π values of phase $\phi(T)$ versus SiC chip temperature. The dots are the 37 data points while the solid line is the cubic fit to the data.

As the temperature of the SiC is changed, the optical path length in the etalon changes causing the detected optical power to cycle between maxima and minima as seen by Figure 4.3.1 where the power is shown after normalization using localized maximum and minimum values. From this normalized data, the locations of consecutive dT values can be determined that produce the consecutive d$\phi(T) = 2\pi$ phase shifts leading to generation of a plot of unwrapped phase shift $\phi(T)$ versus temperature T shown in Figure 4.3.2 given by

$\phi(T) = 9.4 \times 10^{-8} T^3 - 0.00031 T^2 + 0.0046 T + 18$. Note that a numerical cubic fit on the Figure 4.3.2 data is used to calculate $\dfrac{d}{dT}\{\phi(T)\}$ for the chosen 6H-SiC sample. In Figure 4.3.2, note that the variation between the data points and the cubic curve fit is very minimal. Another aspect of the demonstrated experiment is the availability of a large number of data points from near room temperature to 1273 K (1000^0C). Specifically, there are 36 full peak-to-peak power cycles leading to densely filled improved curve fitting. Based upon the $\dfrac{d}{dT}\{\phi(T)\}$ curve fit data in Figure 4.3.2, the 6H-SiC *TOC* is calculated by using Eq. 4.3.10 and Eq. 4.3.5 and the result is shown in Figure 4.3.3. This *TOC* measurement can be expressed as:

$$TOC = -1.2 \times 10^{-10} T^2 + 3.2 \times 10^{-7} T - 9.7 \times 10^{-5} \text{ K}^{-1} \qquad (4.3.11)$$
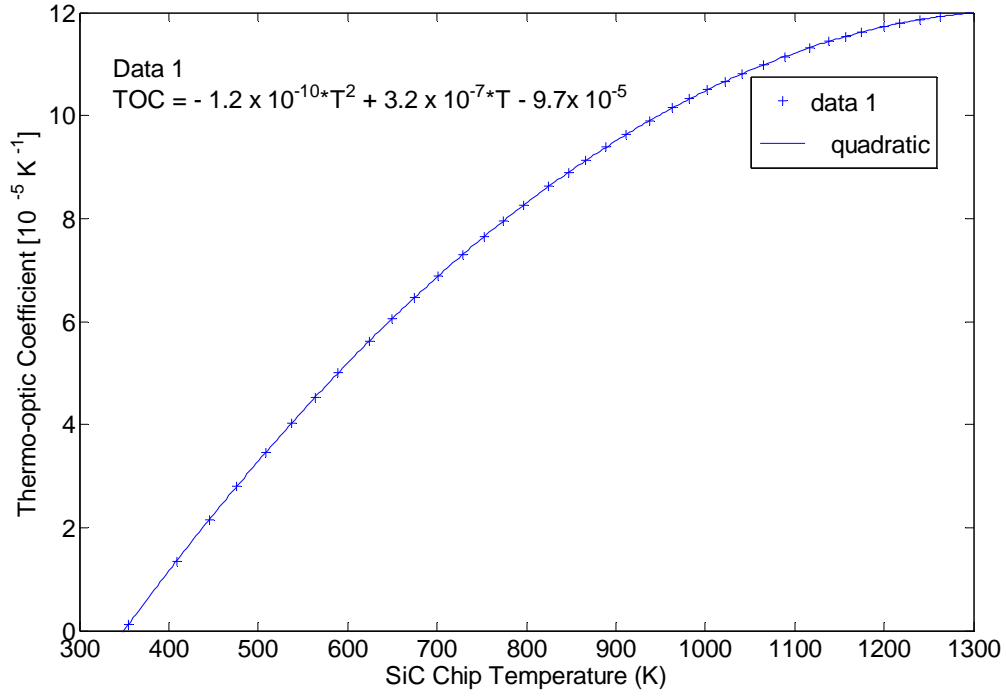
Figure 4.3.3: Calculated 6H-SiC Thermo-optic Coefficient (*TOC*) versus SiC temperature at 1550 nm using the Figure 4.3.2 measured cubic fit data for the phase $\phi(T)$ change with temperature. The *TOC* expression shows a quadratic dependence on the temperature.

To check the validity of the conducted experiment represented by Eq. 4.3.10, the refractive index of SiC is calculated using Eq. 4.3.9 and Eq. 4.3.5 and by using the prior art room temperature SiC refractive index value $n(T_i)$ of 2.57 along with a SiC thermal expansion coefficient of α of 4.56×10^{-6} K^{-1}.[12,13] Note that $\Delta\phi(\Delta T)$ needed for evaluating Eq. 4.3.9 is calculated via Eq. 4.3.8, i.e., by using room temperature phase as the reference phase and subtracting this phase value from the subsequent unwrapped phase values obtained from the Figure 4.3.2 measured expression of $\phi(T) = 9.4 \times 10^{-8} T^3 - 0.00031 T^2 + 0.0046 T + 18$ at the elevated temperature *T*. Hence, the resultant refractive index $n(T)$ is calculated using Eq. 4.3.9 and used in

Eq. 4.3.7 to calculate the *TOC* as shown by the data 2 curve in Figure 4.3.4. This *TOC* quadratic

curve fit expression is given by:

$$TOC = -1.2 \times 10^{-10} T^2 + 3.2 \times 10^{-7} T - 11 \times 10^{-5} \text{ K}^{-1} \qquad (4.3.12)$$
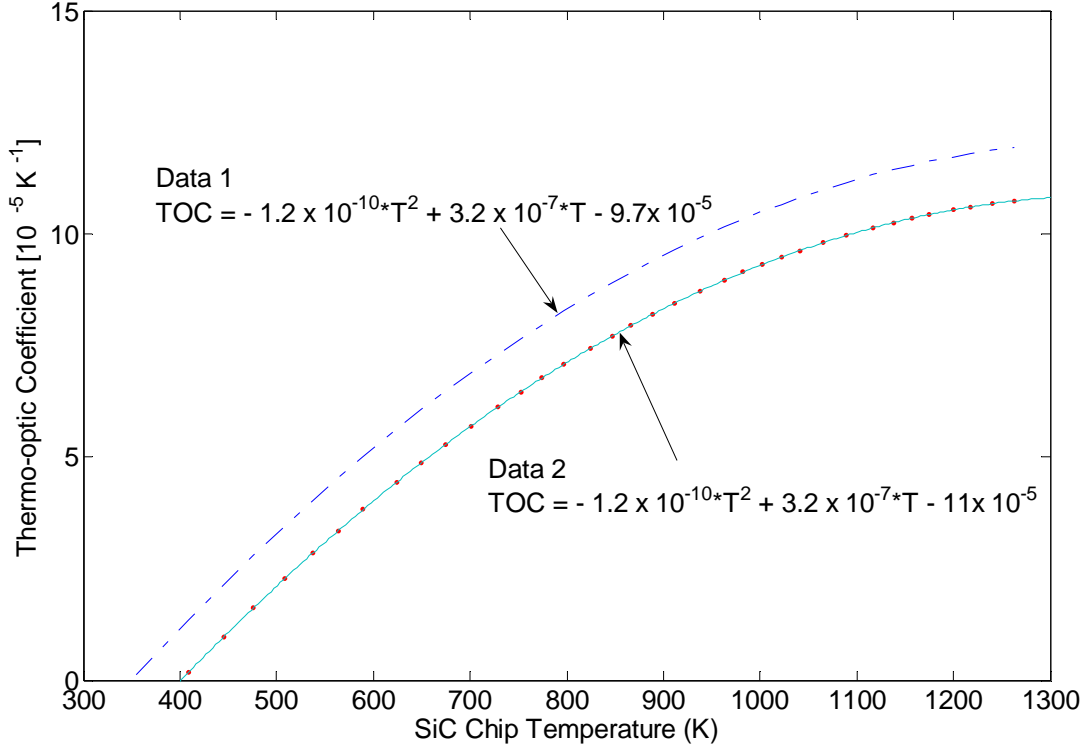
Figure 4.3.4: Calculated 6H-SiC Thermo-optic Coefficient (*TOC*) versus SiC temperature at 1550 nm. Data 1 curve is from Figure 4.3.3 using the approximate expression of Eq. 4.3.10 for *TOC*. Data 2 curve is using the exact expression of Eq. 4.3.7 for the *TOC*.

Note that Eq. 4.3.11 and 4.3.12 are in good agreement with a slight difference only in the

constant term (i.e., 11 instead of 9.7) indicating that the approximation in Eq. 4.3.10 is justified

for a 300 μm thick 6H-SiC chip. Note that the difference between the expressions in Eq. 4.3.7

and Eq. 4.3.10 is given by $\beta = \dfrac{n(T)\alpha\, t(T_i)}{t(T)}$ that is plotted in Figure 4.3.5 for the experiment

conducted in this paper. Results show that ignoring β introduces a relatively small error

(1.182×10^{-5} to 1.188×10^{-5} m/K over a 1000 K temperature change) in calculating the *TOC* of the

used 6H-SiC chip using Eq. 4.3.10. A key advantage of using the Eq. 4.3.10 approximation to

calculate the SiC chip *TOC* is that it eliminates the need for any the prior knowledge of the SiC
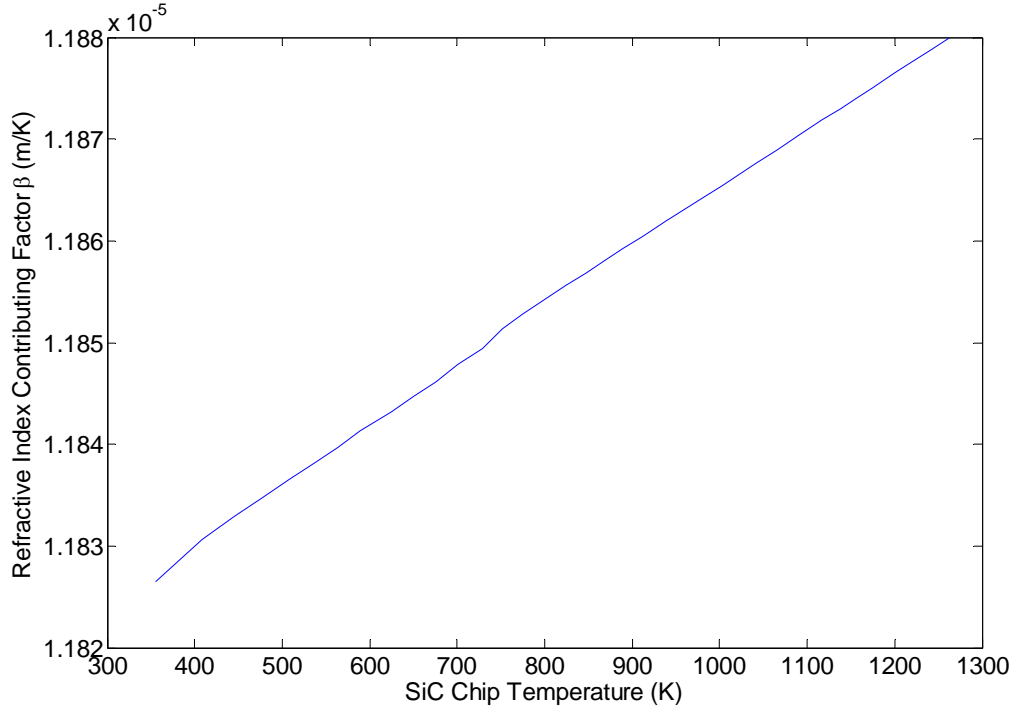
refractive index *n*(*T*).

Figure 4.3.5: Plot of the factor $\beta = \dfrac{n(T)\alpha\, t(T_i)}{t(T)}$ in Eq. 4.3.7, i.e., the difference between Data 1 and
Data 2 in Figure 4.3.4 showing the small error introduced if TOC of 6H-SiC chip is calculated
without prior knowledge of 6H-SiC refractive index.

Conclusions

Fabry-Perot interferometry is revisited in this chapter. A novel approach for single wavelength interferometry in Fabry-Perot interferometry is presented along with complete theoretical basis. Based on this, proposed and demonstrated to 1000^0C is a novel extreme temperature optical sensor using tunable light, free-space beam targeted single crystal SiC chip front-ends, strong two-beam single wavelength interferometry, and robust multi-wavelength signal processing concepts to simultaneously provide both high resolution and wide unambiguous range sensing for dynamic scenarios. The sensor has an operating potential temperature near 2500^0C, the melting point for single crystal SiC. Because single crystal SiC is a highly robust material from a mechanical and chemical point of view, the proposed sensor can also be adapted for extreme environment pressure and chemical species sensing.

The proposed sensor can also be used to characterize materials under extreme conditions. The optical power max/min data provided by the proposed sensor occur for condition cos (ϕ)= ± 1. From these data points collected over a given sensing parameter (e.g., temperature) range, sensor OPL=ϕ can be calculated that contains material refractive index, thickness, and wavelength dependency data. If the two-beam interferometry condition valid for the SiC chip is invoked, all P_m data points can be used to compute material parameters such as the change of index with temperature called thermo-optic coefficient. Thermo-optic coefficient of SiC is measured as a proof-of-concept experiment. Applications for the proposed sensor include use in fossil fuel-based power systems, aerospace/aircraft systems, satellite systems, deep space exploration systems, and drilling and oil mining industries.

References

1. J. H. Ausubel, " Big Green Energy Machines," The Industrial Physicist, AIP, pp.20-24, Oct./Nov., 2004.
2. R. E. Bentley, "Thermocouple materials and their properties," Chap. 2 in *Theory and Practice of Thermoelectric Thermometry: Handbook of Temperature Measurement*, Vol. **3**, pp. 25-81, Springer-Verlag Singapore, 1998.
3. H. Ernst, L. Rauscher, G. Bähr, E. Müller, and W. A. Kaysser, "Long-term stability and thermal cycling of thermocouple contacts to Si up to 350°C," The Third European Conference on High Temperature Electronics (HITEN), pp. 87 – 90, 4-7 July 1999.
4. B. Lee, " Review of the present status of optical fiber sensors," *Optical Fiber Technology*, Vol. **9**, pp.57-79, (2003).
5. M. Winz, K. Stump, T.K. Plant, "High temperature stable fiber Bragg gratings, " Optical Fiber Sensors (OFS) Conf. Digest, pp. 195-198, 2002.
6. D. Grobnic, C. W. Smelser, S. J. Mihailov, R. B. Walker," Isothermal behavior of fiber Bragg gratings made with ultrafast radiation at tempertaures above 1000 C," European Conf. Optical Communications (ECOC), Proc. Vol. **2**, pp.130-131, Stockholm, Sept. 7, 2004.
7. H. Xiao, W. Zhao, R. Lockhart, J. Wang, A. Wang, " Absolute Sapphire optical fiber sensor for high temperature applications," SPIE Proc. Vol. **3201**, pp.36-42, (1998).
8. D. Grobnic, S. J. Mihailov, C. W. Smelser, H. Ding, " Ultra high temperature FBG sensor made in Sapphire fiber using Isothermal using femtosecond laser radiation," European Conf. Optical Communications (ECOC), Proc. Vol. **2**, pp.128-129, Stockholm, Sept.7, 2004.
9. Y. Zhang, G. R. Pickrell, B. Qi, A. S.-Jazi, A. Wang, "Single-crystal sapphire-based optical high temperature sensor for harsh environments," *Opt. Eng.*, Vol. **43**, pp. 157-164, (2004).
10. A. Arbab, A. Spetz and I. Lundstrom, "Gas sensors for high temperature operation based on metal oxide silicon carbide (MOSiC) devices," *Sensors and Actuators B*, Vol. **15-16**, pp. 19-23, (1993).
11. G. Beheim, " Fibre-optic thermometer using semiconductor-etalon sensor," *Elec. Lett.*, Vol. **22**, pp. 238, 239, (1986).
12. L. Cheng, A. J. Steckl, J. Scofield, "SiC thin film Fabry-Perot interferometer for fiber-optic temperature sensor," *IEEE Tran. Electron Devices*, Vol. **50**, pp. 2159-2164, (2003).
13. L. Cheng, A. J. Steckl, J. Scofield, " Effect of trimethylsilane flow rate on the growth of SiC thin-films for fiber-optic temperature sensors," *Journal of Microelectromechanical Systems*, Vol. **12** , pp. 797 – 803, (2003).
14. Eric Udd, *Fiber Optic Sensor,* Wiley Series in Pure and Applied optics, (John Wiley & Sons, Inc. New York, 1991).
15. http://www.ioffe.rssi.ru/SVA/NSM/Semicond/SiC/optic.html
16. Goldberg Yu., Levinshtein M.E., Rumyantsev S.L. in *Properties of Advanced SemiconductorMaterials GaN, AlN, SiC, BN, SiC, SiGe* . Eds. Levinshtein M.E., Rumyantsev S.L., Shur M.S., John Wiley & Sons, Inc., 93-148, New York, 2001.
17. Martin van Buren and N. A. Riza, " Foundations for low loss fiber gradient-index lens pair coupling with the self-imaging mechanism," *Appl. Opt.*, Vol. **42**, pp. 550-565, (2003).

18. Shifu Yuan and N. A. Riza, "General formula for coupling loss characterization of single mode fiber collimators using gradient-index rod lenses," *Appl. Opt.* Vol. **38**, pp.3214-3222, (1999). Erratum, Applied Optics, Vol. **38**, pp. 6292, (1999).
19. Cambridge Technology Scanning Mirrors Catalog, Cambridge, MA, 2005.
20. G. Ghosh, "Temperature dispersion of refractive indices in crystalline and amorphous silicon," *Appl. Phys. Lett.*, Vol. **66**, pp. 3570-3572, (1995).
21. Z. Li and R. C. Bradt, Thermal Expansion and Elastic Anisotropies of SiC as Related to Polytype Structure, Silicon Carbide Symposium (1987).
22. *Properties of Gallium Arsenide, 2nd ed.*, edited by N. Parkman et al., EMIS data reviews Series No. 2 (The Institution of Electrical Engineers and Peter Peregrines LTD., Piscataway, NJ, 1990).
23. M. Bertolotti, V. Bogdanov, A. Ferrari, A. Jascow, N. Nazorova, A. Pikhtin, and L. Schirone, "Temperature dependence of the refractive index in semiconductors," *J. Opt. Soc. Am. B* Vol. **7**, pp. 918-922, (1990).
24. P. Martin, E-Mostafa Skouri, L. Chusseau, and C. Alibert, "Accurate refractive index measurements of doped and undoped InP by a grating coupling technique," *Appl. Phys. Lett.*, Vol. **67**, pp. 881-883, (1995).
25. E. Gini and H. Melchior, "Thermal dependence of the refractive index of InP measured with integrated optical demultiplexer," *J. of Appl. Phys.*, Vol. **79**, pp. 4335-4337, (1996).
26. G. Cocorullo, F. G. D. Corte, and I. Rendina, "Temperature dependence of the thermo-optic coefficient in crystalline silicon between room temperature and 550 K at the wavelength of 1523 nm," *Appl. Phys. Lett.*, Vol. **74**, pp. 3338-3340, (1999).
27. T. Fukano and I. Yamaguchi, "Separation of measurement of the refractive index and the geometrical thickness by use of a wavelength-scanning interferometer with a confocal microscope," App. *Opt.*, Vol. **38**, pp. 4065-4073 (1999).
28. N. A. Riza and M. A. Arain, "Angstrom-Range Optical Path-Length Measurement with a High-Speed Scanning Heterodyne Optical Interferometer", *Appl. Opt.*, Vol. **42**, pp. 2341-2345, (2003).
29. F. G. D. Corte, M. Esposito, L. Moretti, A. Rubino, "Study of the thermo-optic effect in hydrogenated amorphous silicon and hydrogenated amorphous silicon carbide between 300 and 500 K at 1.55 μm," *Appl. Phys. Lett.*, Vol. **79**, pp. 168-170, (2001).
30. N. A. Riza, M. A. Arain, F. Perez, "Harsh Environments Minimally Invasive Optical Sensing Technique for Extreme Temperatures: 1000 °C and Approaching 2500 °C," Optical Fiber Sensors (OFS) 17th Conference, Bruges, Belgium May 23-27, 2005.
31. N. A. Riza, M. A. Arain, F. Perez, "Harsh Environments Minimally Invasive Optical Sensor using Free-Space Targeted Single Crystal Silicon Carbide," submitted to *IEEE Sensors Journal*.
32. F. G. D. Corte, G. Cocorullo, M. Iodice, and I. Rendina, "Temperature dependence of the thermo-optic coefficient of InP, GaAs, and SiC from room temperature to 600 K at the wavelength of 1.5 μm, " *Appl. Phys. Lett.*, Vol. **77**, pp. 1614-1616, (2000).
33. Y. Goldberg, M. Levinshtein, and S. Rumyantsev, *Properties of Advanced Semiconductor Materials*, ed. M.E. Levinshtein et. al., (John Wiley & Sons Inc., UK, 2001).

CONCLUSIONS

The field of optical interferometry has seen rapid technical and scientific progress over the past few decades. A number of instruments capable of precise measurements have been built, and put in commercial use. However, there is still a lot of potential for research and development. This dissertation has shown a number of innovative applications of optical interferometry in optical communication and information processing. A number of useful systems have been designed and demonstrated using several types of interferometers.

Specifically, interference in the form of holography has been used to demonstrate a novel scanner called C-MOS for free space optical communication. C-MOS provides almost 2π coverage for scanning with flexibility of design, simplicity of operation, high speed, and provision of multiple image generation. Applications of C-MOS include laser radars, target designation, optical communication, and 3-D displays. A number of heterodyne interferometer designs have been validated for optical path length measurements. A resolution of 1.4 Angstrom is available with repeatability and stability. A first ever, IR heterodyne interferometer has been proposed and demonstrated for optical metrological applications. The concept has been extended to hybrid optical interferometer with far reaching applications. In the electronic domain, interference between electronic signal has been used to develop reconfigurable RF transversal filter for signal processing, image processing, and aerospace applications. Both positive and negative coefficient filter designs have been demonstrated with a large number of taps. Finally, Fabry-Perot interferometer is used for instantaneous single wavelength interferometry that uses low cost detectors instead of costly optical spectrum analyzer with a higher resolution. Complete theoretical analysis for this is carried out with the proposed signal processing for unambiguous

optical path length measurements. Use of such interferometers built via SiC etalons have been demonstrated for temperature measurements from room temperature to 1000^0C. The same interferometer can be used for applications like pressure measurements, gas detection, and material characterization.

In short, various interferometric systems have been proposed and demonstrated for optical communication and information processing. We believe that through this dissertation, we have been able to contribute significantly in the rich science of interferometry.